

1992

# Tomographic reconstruction algorithms using optoelectronic devices

Tongxin Lu  
*Iowa State University*

Follow this and additional works at: <https://lib.dr.iastate.edu/rtd>

 Part of the [Electrical and Electronics Commons](#), [Signal Processing Commons](#), and the [Systems and Communications Commons](#)

## Recommended Citation

Lu, Tongxin, "Tomographic reconstruction algorithms using optoelectronic devices " (1992). *Retrospective Theses and Dissertations*. 10330.  
<https://lib.dr.iastate.edu/rtd/10330>

This Dissertation is brought to you for free and open access by the Iowa State University Capstones, Theses and Dissertations at Iowa State University Digital Repository. It has been accepted for inclusion in Retrospective Theses and Dissertations by an authorized administrator of Iowa State University Digital Repository. For more information, please contact [digirep@iastate.edu](mailto:digirep@iastate.edu).

## INFORMATION TO USERS

This manuscript has been reproduced from the microfilm master. UMI films the text directly from the original or copy submitted. Thus, some thesis and dissertation copies are in typewriter face, while others may be from any type of computer printer.

**The quality of this reproduction is dependent upon the quality of the copy submitted.** Broken or indistinct print, colored or poor quality illustrations and photographs, print bleedthrough, substandard margins, and improper alignment can adversely affect reproduction.

In the unlikely event that the author did not send UMI a complete manuscript and there are missing pages, these will be noted. Also, if unauthorized copyright material had to be removed, a note will indicate the deletion.

Oversize materials (e.g., maps, drawings, charts) are reproduced by sectioning the original, beginning at the upper left-hand corner and continuing from left to right in equal sections with small overlaps. Each original is also photographed in one exposure and is included in reduced form at the back of the book.

Photographs included in the original manuscript have been reproduced xerographically in this copy. Higher quality 6" x 9" black and white photographic prints are available for any photographs or illustrations appearing in this copy for an additional charge. Contact UMI directly to order.

# U·M·I

University Microfilms International  
A Bell & Howell Information Company  
300 North Zeeb Road, Ann Arbor, MI 48106-1346 USA  
313/761-4700 800/521-0600



**Order Number 9234833**

**Image reconstruction algorithms using optoelectronic devices**

**Lu, Tongxin, Ph.D.**

**Iowa State University, 1992**

**Copyright ©1992 by Lu, Tongxin. All rights reserved.**

**U·M·I**  
300 N. Zeeb Rd.  
Ann Arbor, MI 48106



**Tomographic reconstruction algorithms using optoelectronic devices**

by

**Tongxin Lu**

A Dissertation Submitted to the  
Graduate Faculty in Partial Fulfillment of the  
Requirement for the Degree of  
**DOCTOR OF PHILOSOPHY**

**Department: Electrical Engineering and Computer Engineering**  
**Major: Electrical Engineering (Signal Processing and Communications)**

**Approved:**

Signature was redacted for privacy.

**In Charge of Major Work**

Signature was redacted for privacy.

**For the Major Department**

Signature was redacted for privacy.

**For the Graduate College**

**Members of the Committee:**

Signature was redacted for privacy.

**Iowa State University**  
**Ames, Iowa**

1992

Copyright © Tongxin Lu, 1992. All rights reserved.

## TABLE OF CONTENTS

ACKNOWLEDGEMENTS .....	iv
CHAPTER 1. INTRODUCTION .....	1
CHAPTER 2. LITERATURE REVIEW .....	6
2.1 Tomographic Image Reconstruction Algorithms .....	6
2.2 Optical Implementation of Tomography .....	12
2.3 Spatial Light Modulator Array .....	14
2.4 Charge Coupled Device Detecting Array .....	18
2.5 Summary .....	20
CHAPTER 3. SIMULTANEOUS ITERATIVE RECONSTRUCTION TECHNIQUE AND ITS OPTOELECTRONIC IMPLEMENTATION .....	21
3.1 Cross-Sectional Image and Projection .....	22
3.2 Simultaneous Iterative Reconstruction Technique (SIRT) .....	24
3.3 Optoelectronic Implementation .....	31
3.4 Issues Relating to Optoelectronic Implementation .....	37
3.5 Simulation Results .....	43
3.6 Summary .....	54
CHAPTER 4. PROJECTION ITERATIVE RECONSTRUCTION TECHNIQUE AND ITS OPTOELECTRONIC IMPLEMENTATION .....	56
4.1 Projection Iterative Reconstruction Technique .....	57

4.2 Properties of PIRT .....	64
4.3 Conjugate Gradient Method for PIRT .....	74
4.4 Optoelectronic Implementation .....	82
4.5 Simulation of PIRT .....	85
4.6 Summary .....	92
<b>CHAPTER 5. ITERATIVE FILTERED BACK PROJECTION AND ITS OPTOELECTRONIC IMPLEMENTATION .....</b>	<b>93</b>
5.1 Filtered Back Projection Method and Iterative Implementation .....	94
5.2 Optical Implementation of The Radius Filter .....	102
5.3 Optoelectronic Implementation .....	110
5.4 Simulation Studies .....	112
5.5 Summary .....	115
<b>CHAPTER 6. PIRT WITH PARTIAL CONVOLUTION AND CONSIDERATIONS OF A PROTOTYPE .....</b>	<b>116</b>
6.1 Convolution Back Projection Method .....	118
6.2 Projection Iterative Reconstruction Technique Employing Partial Convolution (PIRT - PC) .....	122
6.3 Residual Iterative Reconstruction Techniques .....	124
6.4 A Hybrid Prototype for Implementing Iterative Reconstruction Algorithms	126
6.5 Implementation of High Speed Analog SLM using Binary SLM .....	132
6.6 Methods for Eliminating The Effects of Limited Dynamic Range .....	136
6.7 Simulation Results .....	137
6.8 Summary .....	144

<b>CHAPTER 7. CONCLUSIONS</b> .....	147
7.1 Comparison of PIRT and SIRT .....	147
7.2 Summary of Proposed Algorithms .....	149
7.3 Summary of Proposed Optoelectronic Structures .....	150
7.4 Further Plans for Algorithm Development .....	151
7.5 Further Plans for Development of Structures .....	151
7.6 Prototype Construction .....	152
7.7 Summary .....	152
<b>BIBLIOGRAPHY</b> .....	153

## ACKNOWLEDGEMENTS

I wish to acknowledge indebtedness to my advisor, Dr Satish Udpa, for providing me the opportunity to pursue the Ph.D degree. His valuable support and encouragement are sincerely appreciated. His professional insight, which has guided this research, is most appreciated.

My sincere appreciation is also due to Dr. Lalita Udpa, whose valuable ideas, criticisms and assistance throughout the research were very useful.

I would like to express my gratitude to Dr. William Lord, Dr. John Doherty and Dr. Suraj Kothari for their professional suggestions and willfully taking time to serve on my committee.

I also wish to thank Dr. Roger Alexander for his valuable suggestions concerning the mathematical aspects of the proposed algorithms.

I would also like to thank all my friends and fellow graduate students who have provided me so much help.

This dissertation is dedicated to my parents for their contributions which are beyond my ability to express.

## CHAPTER 1. INTRODUCTION

The main contribution outlined in this dissertation is the development of a new family of iterative tomographic reconstruction algorithms and a novel concept involving implementation of such algorithms using optoelectronic devices.

The Greek word "tomos" means slice or section. The technique of tomography involves reconstruction of a two-dimensional cross-sectional image of a three-dimensional body from measured projections. The set of projections is taken in the plane of the cross-section around the body at a number of angles. A projection involves a set of measurements taken across the plane with the same orientation. The measurement can be taken using x-rays, acoustic waves, or techniques employing magnetic nuclear resonance. For example, when x-rays penetrate a human body, part of the energy is absorbed. The attenuation in intensity of the x-ray is a function of the absorption coefficients of the cells along the path. A conventional x-ray image is a two-dimensional image perpendicular to the direction of the travelling rays. The tomographic image is an image reproduced in the plane where the rays travel through.

In 1972, Hounsfield invented the x-ray computed tomographic scanner [1, 2] and shared the Nobel Prize with Cormack [3] in 1979. Cormack was credited for his pioneering work in the development of tomographic algorithms. Computerized tomography

has revolutionized several fields including diagnostic medicine, imaging of underground resources and nondestructive testing.

Commonly used tomographic algorithms can be broadly classified as direct and iterative methods, based on the method of computation. This dissertation is mainly interested in iterative algorithms. When a system is underdetermined, commonly used iterative algorithms, such as the Simultaneous Iterative Reconstruction Technique (SIRT) [4], do not guarantee a unique solution. The Projection Iterative Reconstruction Technique (PIRT) proposed in this dissertation [5-6] is a basic iterative image reconstruction algorithm which can be considered as a counterpart of the conventional algorithm - SIRT. The PIRT attempt to obtain the minimum-norm solution of an underdetermined system, whereas, conventional methods are usually based on an attempt to estimate the least squares solution of an overdetermined system. Therefore, when the PIRT algorithm is applied to an underdetermined system, a unique solution is intrinsically guaranteed. The proposed algorithms include a family of accelerated algorithms, such as PIRT-CG (PIRT - Conjugate Gradient), and PIRT-PC (PIRT - Partial Convolution).

In the early 70s, computed tomography (CT) brought its revolutionary impact to diagnostic medicine. Soon, researchers felt that optical processing might be able to compete successfully with electronic computers for transaxial tomography [7]. As a result, various optoelectronic structures were proposed over the last two decades. However, due to noise associated with optical processing techniques and the limited dynamic range of most optoelectronic devices, it was quickly determined that it would be difficult for optoelectronic

structures to compete with electronic computers unless major breakthroughs in the areas of either algorithm development or optoelectronic devices and materials were made. All of the previously reported optical implementations were exclusively focused on implementing direct algorithms. The concept proposed in this dissertation [8] suggests the implementation of iterative algorithms instead of direct algorithms. In contrast to conventional optoelectronic implementations, common problems, such as finite dynamic range of devices and distortions introduced through optical transforms, are overcome by using a closed-loop system. In comparison with implementations of iterative reconstruction algorithms using conventional electronic digital computers, the speed of reconstruction can be improved significantly, since expensive computations associated with back and forward projections are implemented in parallel using optical projections. Furthermore, the structures proposed in this dissertation can be built using inexpensive off-the-shelf video imaging devices.

Chapter 2 represents a literature review and a description of some of the devices used in this dissertation. The Chapter describes a few tomographic algorithms, discusses optoelectronic implementations of tomography, and describes optoelectronic devices such as Spatial Light Modulators (SLM's) and Charge Coupled Devices (CCD's).

The conventional SIRT algorithm and the corresponding iterative optoelectronic structure are reviewed and introduced in Chapter 3. Some basic notations including a matrix formulation of tomographic systems are presented. The least squares solution of an overdetermined system and optoelectronic schemes for implementing forward and back projections using SLM and CCD arrays are also included. The SIRT is analyzed from the

point of view of solving an overdetermined system to obtain the least squares solution. It also shows that, when a system is underdetermined, the SIRT does not guarantee convergence to a unique solution.

Chapter 4 introduces the PIRT algorithm and the corresponding optoelectronic implementation. The significance of the PIRT algorithm is that it guarantees a unique solution when a tomographic system is underdetermined, unlike the SIRT which does not guarantee convergence to a unique solution. The chapter discusses the minimum-norm solution of an underdetermined system and highlights the distinctions between PIRT and SIRT. Several fundamental properties of the new algorithm are discussed in this Chapter. The PIRT-CG (Conjugate Gradient) algorithm designed to accelerate the convergence process, when the system is underdetermined, is also included in this Chapter.

In Chapter 5, an optoelectronic implementation of Iterative Filtered Back Projection (IFBP) method [9] is proposed. Distortion associated with the optical spatial frequency filters is minimized in the structure by using a feedback scheme. In addition, convergence is accelerated by employing a low accuracy optical filter. The most commonly used direct algorithm, Filtered Back Projection (FBP) method, the central slice theorem, optical Fourier Transform and the optical radius filter are also briefly reviewed.

In Chapter 6, an acceleration technique associated with the PIRT type algorithm is introduced and some design considerations for building a prototype are discussed. The PIRT-PC (Partial Convolution) uses a low order FIR filter in the basic PIRT algorithm to accelerate the convergence of high frequency components. Since the low order FIR filter

can be considered as a reduced order convolution, the commonly used direct method, Convolution Back Projection (CBP) method, is also discussed in this Chapter. A hybrid structure using video imaging devices and microprocessors is presented. This prototype can be used to further study the performance of algorithms. The iteration period is 1/30 second and the reconstruction time is less than one second if the PIRT-PC algorithm is used.

In addition to providing a few concluding remarks, Chapter 7 summarizes the algorithms and implementation schemes discussed in this dissertation.

## CHAPTER 2. LITERATURE REVIEW

This Chapter summarizes some of the work done to date in developing tomographic reconstruction algorithms and methods for implementing them using optoelectronic devices. The Chapter also presents a brief review of a few optoelectronic devices such as Spatial Light Modulators (SLM) and Charge Coupled Device (CCD) image detectors.

### 2.1 Tomographic Image Reconstruction Algorithms

#### 2.1.1 Cross-Sectional Image and Projection

A 2-D cross-sectional image of a 3-D object is shown in Fig. 2.1. Parallel x-ray projections are taken around the object in several orientations. The objective of the tomographic image reconstruction algorithm is to reconstruct the 2-D cross-sectional image on the basis of information contained in the ray-sums of projections measured from several orientations across the image plane around the object.

In the continuous case, a ray sum is expressed by the Radon transform which is obtained by performing a line integration along each ray [10-12]. As shown in Fig. 2.2, a line integral  $P_{\theta}(t)$  can be defined as

$$P_{\theta}(t) = \int_{(\theta, t) \text{ line}} f(x, y) dx \quad (2.1)$$

Using the sifting property of the delta function, eq. 2.1 can be rewritten as

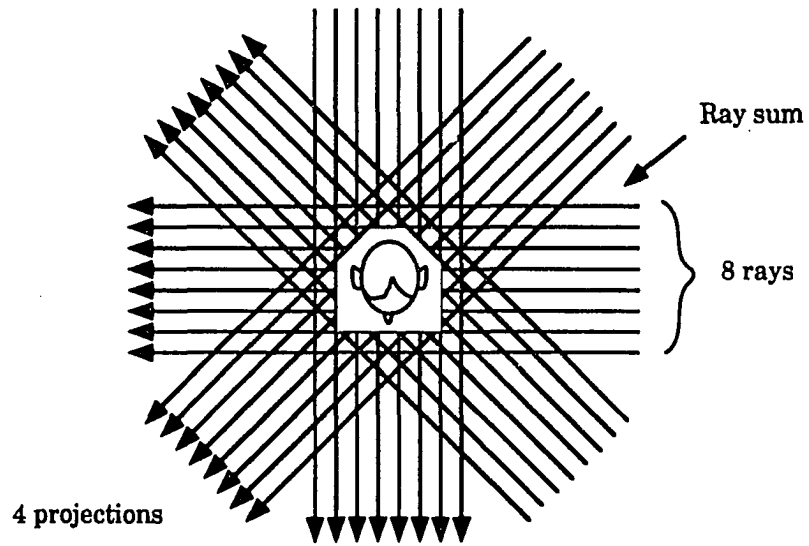


Fig. 2.1. In order to obtain the cross-sectional image, x-rays are taken around the object.

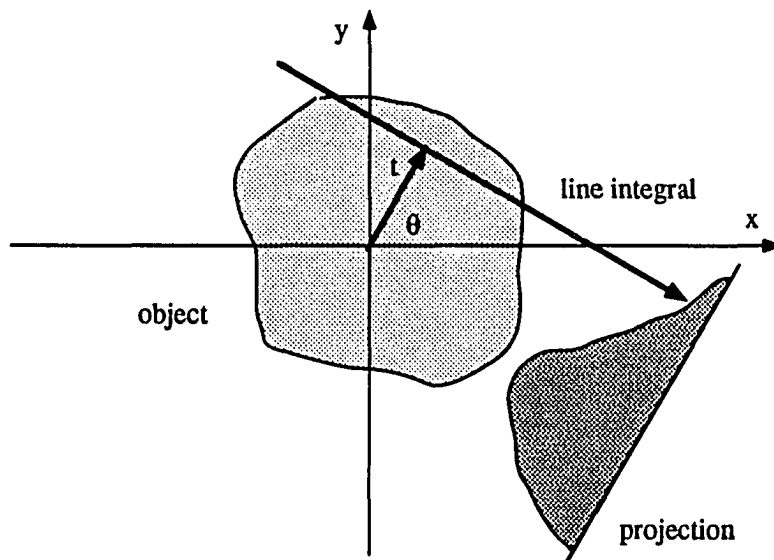


Fig. 2.2. A 2-D cross-sectional image and corresponding projection.

$$P_{\theta}(t) = \int_{-\infty}^{\infty} \int_{-\infty}^{\infty} f(x, y) \delta(x \cos \theta + y \sin \theta - t) dx dy \quad (2.2)$$

The function  $P_{\theta}(t)$  is known as the Radon transform of the function  $f(x, y)$ .

In the discrete case, eq. 2.2 can be rewritten in the form of a summation and projection operations can be modeled using a linear system representation

$$\mathbf{A} \mathbf{x} = \mathbf{b} \quad (2.3)$$

where  $\mathbf{x}$  represents all pixels on the two dimensional image,  $\mathbf{b}$  represents data measured at all projection orientations, and the matrix  $\mathbf{A}$  maps data from the image space to the projection space. Image reconstruction involves estimation of the 2-D image  $\mathbf{x}$  from known projections  $\mathbf{b}$ .

Tomographic image reconstruction involves operations of mapping the data from the projection space back to the image plane. The operation is called back projection. The back projection was one of the earliest methods used to obtain the a cross-section of an object in an x-ray film before computed tomography was invented [11-12]. Since the method simply smears the projection data back to the image space instead of solving for the true inverse, information in the reconstructed image severely lacks in detail.

### 2.1.2 Reconstruction Algorithms

Tomographic image reconstruction involves estimation of  $f(x, y)$  from given  $P_{\theta}(t)$  using the inverse Radon transform. The task is summarized in eq. 2.2 for the continuous

case. In the discrete case, the objective is to determine  $\mathbf{x}$  from known  $\mathbf{b}$  as expressed in eq. 2.3. In computed tomography, the enormous amount of data contained in the projections collected in several directions has to be appropriately manipulated to obtain the spatial distribution of the parameters. The algorithms for tomographic imaging solves the inverse problem by estimating the cross-sectional images from the given projections. The commonly used algorithms can be broadly classified as direct methods or iterative methods based on the method of computation.

### **Direct Methods**

The direct methods whose mathematical foundation was laid by Radon in 1917 [13], constitutes the basis of most commonly used algorithms. The tomographic image reconstruction process can be considered as finding the inverse of the Radon transform. However the singularities associated with the inverse transform prohibit its direct use. In practice, the commonly used algorithms include Fourier transform methods, Filtered Back Projection methods (FPB) and Convolution Back Projection methods (CBP). These algorithms can be derived either from the Inverse Radon transform or using Fourier transform and the Central Slice Theorem [10-12].

### **Iterative Methods**

The iterative methods consider tomographic systems as large and sparse linear time-invariant systems and then solve for the system iteratively without calculating the inverse.

The most commonly used iterative methods include the Algebraic Reconstruction Technique (ART), Simultaneous Iterative Reconstruction Technique (SIRT), and schemes employing such methods as Maximum Likelihood, Maximum Entropy approaches and so on.

The Algebraic Reconstruction Technique (ART) was first introduced in open literature by Gordon, Bender, and Herman in 1970 [14]. Coincidentally, the same algorithm had already been proposed by Hounsfield in his patent application filed in 1968 for the first CT [1]. The mathematical foundation of the ART can be traced back to the "method of projections" proposed by Kaczmarz in 1937 [15] for solving systems of linear equations iteratively.

The Simultaneous Iterative Reconstruction Technique (SIRT) is discussed in greater detail in Chapter 3. The SIRT was introduced for tomographic image reconstruction by Gilbert in 1972 [7]. An essentially similar iteration method was proposed for solving integral equations by Landweber in 1951 [16]. Many acceleration techniques for the SIRT have also been proposed, including the conjugate gradient method [17] for tomographic reconstruction by Artzy and Herman [18]. The iterative method has also been used for positron emission tomography [19-20]. The SIRT can be derived directly by applying the basic iterative method to obtain the least squares solution of the normal equation method for overdetermined systems. Theoretically, for an underdetermined system, the SIRT converges to the minimum-norm solution when the initial value is properly chosen. However, a minimum-norm solution is not guaranteed if numerical error is present or acceleration methods, such as the Conjugate Gradient (CG) method, are applied.

The Multiplicative Algebraic Reconstruction Technique (MART) was proposed by Gordon, Bender, and Herman in 1970 [14]. It has been shown that the result obtained using this algorithm is identical to those obtained using Maximum Entropy methods. In the case of X-ray tomography, the Maximum Entropy algorithms (MENT) have also been extended further by Minerbo [21] as well as Dusaussor and Abdou [22]. For emission tomography (ET), the Maximum Likelihood reconstruction algorithms are similar to multiplicative recursive algorithms and have drawn attention in medical applications [23-25].

In the case of most iterative reconstruction methods, the error corrections are fed back in the image space except for a few exceptions, such as the Projection Space Iterative Reconstruction-Reprojection (PIRR) [26-27] and Projection Space MAP (PSMAP) methods [28-30]. The PIRR projects the reconstructed image to the projection space recursively in order to recover the missing projection data whereas the PSMAP optimizes data in the projection space iteratively and then reconstructs the image using convolution back projection (CBP). The approaches and objectives of the projection space iterative algorithms differ from the PIRT proposed in this dissertation.

Because of the extreme computational demands, iterative methods usually are not able to compete with direct algorithms in commercial CT systems. However, the iterative algorithms still offer advantages in certain applications. They are particularly suitable for reconstructing images from incomplete data, reconstruction with *a priori* statistical knowledge as well as single photon emission computerized tomography (SPECT) and positron emission tomography (PET) [17-38].

## 2.2 Optical Implementation of Tomography

As mentioned before, conventional x-ray tomography techniques were used to estimate cross-sectional images of objects even before the invention of computed tomography. In this method, a photographic film and the object are rotated synchronously. X-rays pass through a narrow slit, penetrate the object and are recorded on another film. The signal is then smeared on the film plane. Although, the technique may be considered as the earliest optical implementation of tomography, the method is mathematically equivalent to the back projection method [11-12]. However, the quality of results obtained are poor compared with those obtained using modern computed tomography techniques.

The computed tomography methods differ from the conventional tomography schemes in that they attempt to solve the inverse problem using the measured projection instead of simply smearing the projections back into the image space.

The earliest reported optical computed tomographic reconstruction processor was built by Peter [7] in 1973. An image was first recorded on a film using back projections. The output image was obtained by filtering the blurred image using a coherent optical spatial filter. The resulting image was much sharper than those obtained using back projections only.

In order to avoid the problems associated with coherent processing such as speckle and other coherent noise, several incoherent optical tomographic reconstruction systems were built.

The Oldelft transaxial tomography system, built in 1978 [40], implements the

convolution back projection method. The Oldef system is a hybrid system and optics is used only for one dimensional and two channel convolutions. The two channels are used for positive and negative valued convolution respectively.

The Edholm's system, built in 1977 [41-42], is an optical system using films. The original projections and the filtered negative projections are prepared on two separate films. The reconstructed image is then recorded on a rotating output film.

Since 1977, several structures have been proposed by Gmitro et al. [43-46], where pupil plane masks have been used for spatial radius filtering operations. This approach, known as optical transfer function (OTF) synthesis, is a technique for performing spatial filtering operations in an incoherent system. The loop processor records all projections on a continuous film loop and the drum processor records projections on the surface of a drum. The CCD processor collects the back projected output image using a CCD camera.

Several coherent computed tomography systems have been proposed by Hansen et al., and Nishimura and Casasent. These approaches have been summarized by Gmitro et al. [44]. All of these algorithms involve the use of direct algorithms. Due to the finite dynamic range of materials and devices, and distortions of optical transforms, these approaches could not compete with electronic computers in respect of the quality of reconstructed images.

Advances in technology related to video imaging devices have led to improvements in the quality and speed of optical implementations [46-48]. Recently, a videographic tomographic structure for medical imaging, built by Gmitro et al. [48], was able to achieve

1% contrast resolution. The structure was able to achieve real time reconstruction. Three filter structures were evaluated including a digital FIR filter, an Acoustic-optic (AO) convolver and a Surface Acoustic Wave (SAW) convolver. The best results were obtained using the digital FIR filter. However, the digital FIR filter was not only expensive but also introduced distortions in the low frequency range since the order of the filter used was not long enough to cover the entire frequency range. In addition, optical distortions were not eliminated. Nevertheless, the development is very encouraging since it demonstrated the feasibility of high quality and high speed optoelectronic tomography.

### **2.3. Spatial Light Modulator Array**

The optoelectronic systems used to implement many of the reconstruction algorithms described in this dissertation employ devices such as the spatial light modulator and Charge Coupled Devices. The following sections provide a brief introduction to the devices.

Spatial Light Modulators (SLM's) are devices which can be employed to modulate the intensity, magnitude, polarization or phase of light. Applications of SLM range from commercial television displays [48], real-time image processing to parallel optical computing [49-57]. Fig. 2.3 shows an example of a linear SLM array with four cells. The optical transmissivity of each cell can be controlled by the applied modulating signal. The intensity of the output light beam from each cell is, therefore, a function of the intensity of the incident beam and the transmissivity of the cell. SLM's can be classified on the basis of their addressing modes. If the modulating signal is controlled by an electrical signal, it

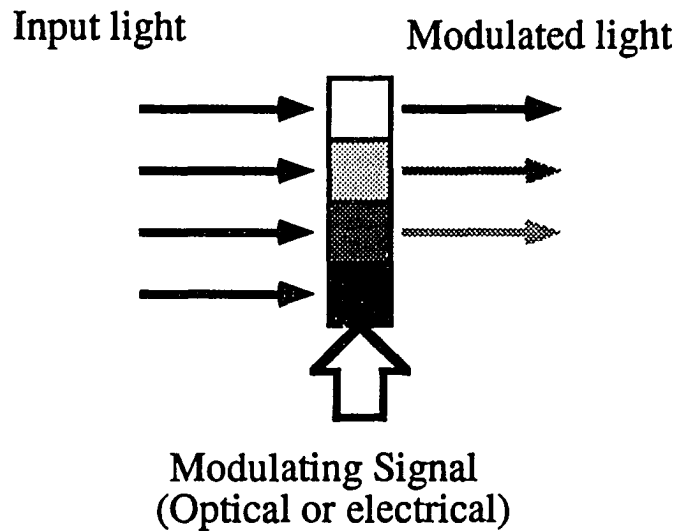


Fig. 2.3. A linear SLM array with four cells.

is referred to as an electrically addressed SLM (E-SLM). If the modulating signal is a second beam of light, it is classified as an optically addressed SLM (O-SLM).

SLM's have been built using several technologies. This had led to the development of the optoelectronic SLM, opto-acoustic SLM, and opto-magnetic SLM. Commercially available SLM's, such as Liquid Crystal (LC) SLM [48], and Ferroelectric Liquid Crystal (FLC) SLM [54] will be briefly described in this section. For the sake of completeness, Multiple Quantum Well (MQW) SLMs [55-57] are also discussed.

Liquid crystal are organic materials that possess an intermediate phase between the solid and liquid phase. The molecular orientations of liquid crystal materials can be changed by applying electrical fields. Therefore, the polarization of the light through such materials can also be twisted. Amplitude and intensity modulation is obtained by placing a polarizer and an analyzer in front of and behind the liquid crystal layer respectively. The technology relating to Liquid Crystal SLM has been used in commercial video image projectors and miniature television sets. Since commercial LCTV's offer many of the same attractive features as other modulators, but at only a fraction of the cost, they have also been used in many optical signal processing and computing systems [58].

Ferroelectric liquid crystals are characterized by a spontaneous molecular polarization caused by an anisotropy in the molecule. The molecular polarization allows the orientation of FLC's to be easily switched with a small electric field. The FLC SLM has the advantage of high speed and high contrast ratio. Commercial available FLC SLM only offer binary light modulation since tilting of FLC molecules is confined to two orientational positions.

Multiple quantum well (MQW) structures consist of thin layers of low bandgap semiconductor (wells) sandwiched between layers of larger bandgap semiconductor (barriers). When the thickness of the well layers is on the order of a carrier de Broglie wavelength, the electron and the hole are forced to orbit close to each other and the binding energy increase correspondingly. The electrical and optical properties of the structure are then dominated by quantum size effects (QSE). The QSE results in the features of step-like absorption edges in the optical absorption spectrum and room temperature exciton

resonances. The change in the energy levels of the excitons resulting from applied electric field, called the quantum-confined Stark-effect (QCSE), allows shifting of the abrupt, highly absorbing edge. By shifting the absorption edges, the MQW structures produce larger absorption changes (in a narrow spectrum range around the absorption edges) than those in bulk semiconductors with the same applied field.

The LCTV's are able to provide better grey level images. However most of them can only operate at television frame rates (30 to 60 frames per second). The FLC SLM's support binary processing only but can operate at relatively higher speed (up to 100 KHz). The MQW SLM's are expected to operate at GHz rates. However, the spectrum of modulated light has to be within a narrow range. Comparisons of some commercially available SLM's are given in Tables 2.1 [58] and 2.2 [54].

**Table 2.1. Characteristics of Several Common SLMs [58]**

<i>SLM</i>	<i>Visibility</i>	<i>Resolution</i>	<i>Size</i>	<i>Speed</i>	<i>Cost</i>
MSLM	0.5	4 lp/mm	25 mm dia	2 sec	\$25K
MOD	0.91	6.4 lp/mm	1×1 cm	200 Hz	\$18K
DMD	0.5	10 lp/mm	0.64 cm	60 Hz	?
FELC	0.9	40 lp/mm	12.5 mm dia	60 Hz	\$17.5K
HC LCLV	0.86	60 lp/mm	50×50 mm	60 Hz	\$25K
Epson LCTV	0.96	6.3 lp/mm	2.54×1.9 cm	60 Hz	\$800

**Table 2.2. Specifications of Several Electrically Addressed SLMs [59]**

<i>device</i>	<i>material</i>	<i>pixels</i>	<i>frame rate Hz</i>	<i>pixel size <math>\mu m</math></i>	<i>fill factor</i>	<i>contrast ratio</i>
STC Ltd.	FLC	128×128	165	165×165	0.83	200:1
Displaytech	FLC	10×10	2000	1 <sup>3</sup> ×10 <sup>3</sup>	0.77	100:1
Disp.tech CMOS	FLC	64×64	4500	45×45	0.56	12:1
Semetex SMD	Iron Garnet	128×128	100	56×56	0.54	10 <sup>4</sup> :1
Litton MOSLM	Iron Garnet	128×128	2000	56×56	0.54	-
TI DMD	Def.mirror	128×128	1200	25×25	0.9	2:1

#### 2.4 Charge Coupled Device Detecting Array

Charge Coupled Devices (CCD) are also called Charge Transfer Devices (CTD). These devices were introduced by Boyle and Smith in 1970 [59]. The applications of CCD's include optoelectronic computing [48-51, 60-62], charge domain signal processing [63-65], focal plane image processing [66-69], high speed analog-to-digital and digital-to-analog conversion, time-axis conversion [70], and image detection [71].

A CCD array functions like shift registers in which sampled values of an analog signal are stored in the form of charges in a series of neighboring cells. Clock pulses allow the transfer of charge from one cell to the next without significant loss in accuracy. The charge, which is called a charge packet, is a small amount of charge stored in potential wells created by the gate voltage. By periodically varying the electrode or gate voltage, the

potential wells are shifted along the semiconductor. The charge packet, located under the voltage gate, moves along with the potential wells.

CCDs can be classified as surface-channel CCD (SCCD) and bulk-channel CCD (BCCD) depending on the device structures. A device is called SCCD if the charge resides at the semiconductor surface. In the BCCD, the charge location is moved away from the surface into the n-channel. There is no interaction between and the charge the interface states. In the case of peristaltic CCD, the n-channel is thicker and the charge is farther away from the surface. In spite of the increased process complexity, almost all of today's devices are BCCD's, due to their superior performance.

High performance Silicon CCDs can offer charge transfer efficiencies as high as 0.999999. Some of the fastest Silicon CCDs have been operated at several hundred MHz. Silicon peristaltic CCDs have been operated with clock frequencies up to 200 MHz. High mobility GaAs is a good material for building very high frequency CCD's. Devices with operating frequency in the range of GHz have been fabricated. However, typical operational frequencies of commercially available Silicon CCD's are usually below 20 MHz.

CCD detecting arrays are commonly used as solid state image detectors. Fig. 2.4 shows a linear CCD detector array with four cells. Each cell generates an electrical charge proportional to the number of photons incident on it. Alternatively, the charge developed is proportional to the intensity of the light integrated over the period of exposure. Charges in a CCD array can be shifted from cell-to-cell without significant loss in magnitude. The output is a sequence of voltage values proportional to the charge in each cell. Typical

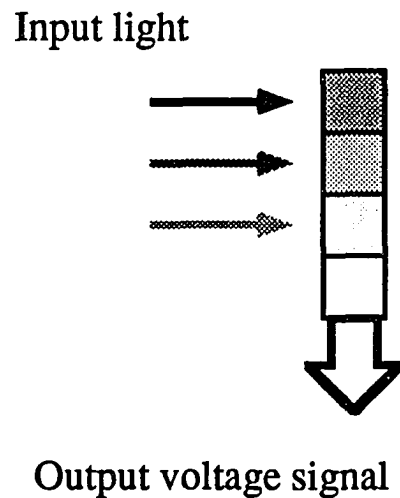


Fig. 2.4. A linear CCD detecting array with four cells.

contrast resolution of commercial image detectors can be in excess of 4096 distinguishable gray levels.

## 2.5 Summary

In this Chapter, some of the work done to date in developing tomographic reconstruction algorithms and methods for implementing them using optoelectronic devices have been described. The Chapter also presents a brief review of optoelectronic devices such as Spatial Light Modulators (SLM's) and Charge Coupled Devices (CCD).

### CHAPTER 3. SIMULTANEOUS ITERATIVE RECONSTRUCTION TECHNIQUE AND ITS OPTOELECTRONIC IMPLEMENTATION

The Simultaneous Iterative Reconstruction Technique (SIRT) uses an iterative method to solve linear equations for tomographic image reconstruction. The SIRT was first proposed by Gilbert in 1971 [4]. The basic SIRT uses Richardson's method [73] to solve a system  $Ax = b$ . The solution  $x = [A^T A]^{-1} A^T b$  represents the least squares solution [74] of the normal equations. It can also be treated as a method of quadratic optimization [11, 18]. Acceleration techniques, such as the Conjugate Gradient method, have been used in conjunction with SIRT to expedite convergence [18, 31-32].

Even though, iterative tomographic algorithms have been discussed extensively during the last two decades, most applications employ direct reconstruction methods, such as the Filtered Back Projection (FBP) method and the Convolution Back Projection (CBP) method. The computation cost of iterative algorithms is formidable if they are implemented using today's electronic computers. An optoelectronic structure implementing SIRT is presented in this Chapter. The proposed structure performs back and forward projection operations by simply projecting data optically. Time consuming matrix operations are, therefore, eliminated and the processing speed is improved significantly. Since, there is no need for computing Fourier Transforms or performing convolution operations explicitly, the cost of such a system is significantly lower.

Section 3.1 introduces the notation used in casting the tomographic reconstruction issue as a problem of solving a linear system. The SIRT is reviewed as an iterative method for solving overdetermined systems in section 3.2. This is followed by a discussion on the issues of convergence. In section 3.3, the optoelectronic implementation of SIRT is introduced after explaining the basic building blocks employed for back and forward projections briefly. Issues relating to the impact of device limitations on the performance of the proposed optoelectronic implementation are discussed in the section 3.4. Simulation results are given in section 3.5.

### 3.1 Cross-Sectional Image and Projection

A 2-D cross-sectional image of a 3-D object is shown in Fig. 3.1. The objective of the tomographic image reconstruction algorithm is to reconstruct the 2-D cross-sectional image on the basis of information contained in the ray-sums of projections measured from several orientations across the image plane around the object. A ray-sum is an integration or a summation of pixel grey levels across the image plane along that ray. A projection is a set of ray-sums in parallel with the same orientation.

Consider a 2-D discrete model for the  $n \times n$  cross-sectional image where the pixels and ray-sums are numbered from 1 to  $N$  and 1 to  $M$  respectively. Let  $x_j$ ,  $j = 1, 2, \dots, N$ , denote the grey level of the  $j^{\text{th}}$  pixel, and  $b_i$ ,  $i = 1, 2, \dots, M$ , represent the  $i^{\text{th}}$  ray-sum. Then, the ray-sum  $b_i$  can be expressed as

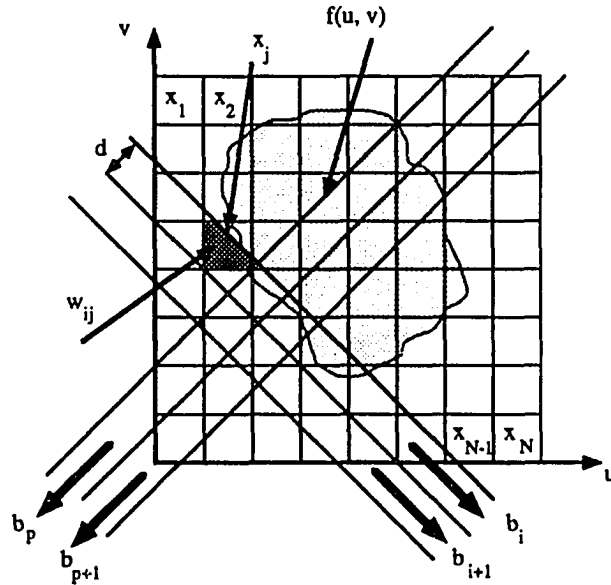


Fig. 3.1. A 2-D cross-sectional image and the corresponding projections.

$$\mathbf{b}_i = \sum_{j=1}^N w_{ij} x_j, \quad \text{for } i=1, \dots, M \quad (3.1)$$

where  $w_{ij}$  is the weight factor representing the fractional area intercepted by the  $i^{\text{th}}$  ray-sum and the  $j^{\text{th}}$  pixel. The projection operations of eq. 3.1 can be rewritten in a matrix form as

$$\mathbf{A}_{M \times N} \mathbf{x}_{N \times 1} = \mathbf{b}_{M \times 1} \quad (3.2)$$

where

$$\mathbf{x} = [x_1 \ x_2 \ \dots \ x_N]^T$$

$$\mathbf{b} = [b_1 \ b_2 \ \dots \ b_M]^T$$

In this expression, all the  $n \times n$  pixels in the 2-D cross-sectional image are stacked into the

$N \times 1$  vector  $\mathbf{x}$  and all the ray-sums from all projection orientations are denoted by the  $M \times 1$  vector  $\mathbf{b}$ . The matrix  $\mathbf{A}$  is an  $M \times N$  projection operator matrix mapping  $\mathbf{x}$  into  $\mathbf{b}$  and  $w_{ij}$  is its  $(i,j)^{\text{th}}$  element. Image reconstruction involves estimation of  $\mathbf{x}$  from known  $\mathbf{b}$ .

The operation of mapping the data from the projection space back to the image plane is called back projection. The back projection operation can also be expressed in the form of summation or matrix vector multiplication as

$$\beta \sum_{i=1}^M w_{ij} b_i \quad \text{for } j=1, \dots, N \quad (3.3)$$

or

$$\beta \mathbf{A}^T \mathbf{b} \quad (3.4)$$

where  $\beta$  is a constant used to normalize back projections. Usually,  $\beta$  is chosen as

$$\beta = \frac{1}{\|\mathbf{A}\|_1 \|\mathbf{A}\|_\infty} \quad (3.5)$$

where  $\|\cdot\|_1$  and  $\|\cdot\|_\infty$  denote matrix one-norm and infinite-norm.

### 3.2 Simultaneous Iterative Reconstruction Technique (SIRT)

In what follows, the least squares solution of the normal equations representing overdetermined systems is reviewed briefly. The Simultaneous Iterative Reconstruction Technique (SIRT) for computing the least squares solution of overdetermined systems is then discussed.

### 3.2.1 Least Squares Solution

When  $M > N$  and all  $N$  columns of the  $M \times N$  matrix  $A$  are linearly independent, the system is overdetermined. This implies, that there is no direct solution, since the number of equations exceeds the number of unknowns. However, there exists a unique least squares solution. Using the normal equation method, the least squares solution for the overdetermined system is

$$\mathbf{x} = [\mathbf{A}^T \mathbf{A}]^{-1} \mathbf{A}^T \mathbf{b} \quad (3.6)$$

The result can be derived by minimizing  $\|\mathbf{Ax} - \mathbf{b}\|_2$  where  $\|\cdot\|_2$  is the Euclidean norm and  $\mathbf{A}^T \mathbf{A}$  is symmetric and positive definite,

$$\begin{aligned} \frac{d}{d\mathbf{x}} \|\mathbf{Ax} - \mathbf{b}\|_2^2 &= \frac{d}{d\mathbf{x}} (\mathbf{Ax} - \mathbf{b})^T (\mathbf{Ax} - \mathbf{b}) \\ &= \mathbf{A}^T \mathbf{A} \mathbf{x} - \mathbf{A}^T \mathbf{b} \\ &= \mathbf{0} \end{aligned} \quad (3.7)$$

$$\mathbf{A}^T \mathbf{A} \mathbf{x} = \mathbf{A}^T \mathbf{b}$$

$$\mathbf{x} = [\mathbf{A}^T \mathbf{A}]^{-1} \mathbf{A}^T \mathbf{b}$$

if  $[\mathbf{A}^T \mathbf{A}]$  is nonsingular.

Fig. 3.2 shows the least squares solution for a overdetermined system where  $M=3$ ,  $N=2$ .

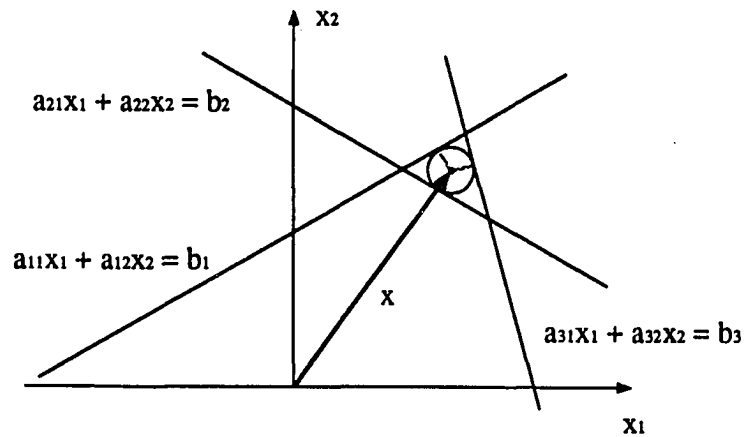


Fig. 3.2. The least squares solution for an overdetermined system where  $M=3$ ,  $N=2$  [74].

### 3.2.2 Iterative Methods for Image Reconstruction

In many applications such as the image reconstruction, the dimensions of the matrix  $A$  are large. In this case, least squares solution of the normal equations cannot be solved for directly using matrix inversion. Since the matrix  $A$  is extremely large and sparse in such cases, the matrix  $A$  cannot be formed in practice due to memory limitations and consequently only the non-zero entries of the matrix  $A$  are calculated on-line on an "as needed" basis and disposed off shortly thereafter. Since the matrix is not available in its entirety, techniques, such as Singular Value Decomposition (SVD), cannot be applied. However, these systems can be solved for using iterative methods where the matrix  $A$  is not required in full.

In eq. 3.6, the least squares solution  $x$  of the overdetermined linear system can be obtained by solving for  $x$  in a linear system  $Dx = c$ , where  $D = A^T A$  is an  $N \times N$  symmetric

positive definite matrix and  $\mathbf{c} = \mathbf{A}^T \mathbf{b}$  is an  $N \times 1$  vector. The least squares solution of the overdetermined system can be obtained using iterative methods, such as the basic RF (Richardson's) method

$$\mathbf{x}(k) = (\mathbf{I} - \alpha \mathbf{D})\mathbf{x}(k-1) + \alpha \mathbf{c} \quad (3.8)$$

or

$$\mathbf{x}(k) = \mathbf{x}(k-1) + \alpha (\mathbf{c} - \mathbf{A}^T \mathbf{A} \mathbf{x}(k-1)) \quad (3.9)$$

or

$$\mathbf{x}(k) = \mathbf{x}(k-1) + \alpha \mathbf{A}^T [\mathbf{b} - \mathbf{A} \mathbf{x}(k-1)] \quad (3.10)$$

where  $k$  is the iteration index and  $\alpha$  is the relaxation coefficient chosen such that all the eigenvalues of  $[\mathbf{I} - \alpha \mathbf{A}^T \mathbf{A}]$  lie within the unit circle. Eq. 3.10. can be rewritten as

$$\begin{aligned} \mathbf{x}\{z\} &= [\mathbf{I} - [\mathbf{I} - \alpha \mathbf{A}^T \mathbf{A}] z^{-1}]^{-1} \alpha \mathbf{A}^T \mathbf{b}\{z\} \\ &= [\mathbf{I} - [\mathbf{I} - \alpha \mathbf{A}^T \mathbf{A}] z^{-1}]^{-1} \alpha \mathbf{A} \mathbf{b} \frac{1}{1 - z^{-1}} \end{aligned} \quad (3.11)$$

where  $z^{-1}$  is the unit delay in terms of  $k$  and  $\mathbf{b}\{z\}$  is a constant vector. Invoking the final value theorem, the final value of  $\mathbf{x}$  is

$$\begin{aligned} \lim_{k \rightarrow \infty} \mathbf{x}(k) &= \lim_{z \rightarrow 1} [(1 - z^{-1}) \mathbf{x}\{z\}] \\ &= [\mathbf{A}^T \mathbf{A}]^{-1} \mathbf{A}^T \mathbf{b} \end{aligned} \quad (3.12)$$

The result converges to the least squares solution of the normal equations as given in eq. 3.6.

In tomographic image reconstruction, the matrix  $A$  is typically very large and sparse and consequently solving for  $x$  directly is unrealistic. The SIRT is a well-known method and uses a scheme identical to eq. 3.11. for solving an overdetermined system,

$$x(k) = x(k-1) + \alpha \beta A^T [b - A x(k-1)] \quad (3.13)$$

where  $\beta$  is used to normalize the back projection defined in eq. 3.4 and eq. 3.5. When the system is overdetermined, the solution converges to the least squares solution.

The SIRT can be considered as a time-invariant linear feedback system as shown in the block diagram given in Fig. 3.3. The matrix-vector multiplication associated with the matrix  $A$  performs the forward projection. The forward projection maps the reconstructed image into the projection space. This is equivalent to determining the measured projections taken from the test object as described by eq. 3.2 and Fig. 3.1. The matrix-vector multiplication  $\beta A^T$  represents the back projection. The back projection maps the data from the projection space back to the image space. This operation is in the reverse direction of the forward projection and simply smears the data in the projection space back to the image space along each ray. The sparse matrix  $A$  is too large to be stored. The matrix-vector-multiplications associated with the back and forward projections are performed using eqs. 3.1 and 3.3 and weight factors, which are calculated on line ( $w_{ij}$ 's). Expressing SIRT using eq. 3.13, the residuals are obtained in the projection space as shown in the system block diagram in Fig. 3.3. From eq. 3.9, an alternative version of the original SIRT can be obtained by comparing the errors in the image space.

$$\mathbf{c} = \beta \mathbf{A}^T \quad (3.14)$$

$$\mathbf{x}(\mathbf{k}) = \mathbf{x}(\mathbf{k}-1) + \alpha [\mathbf{c} - \beta \mathbf{A}^T \mathbf{A} \mathbf{x}(\mathbf{k}-1)]$$

The convergence properties of reconstruction algorithms expressed by eq. 3.13 and eq. 3.14 are the same. Both approach the least squares error in the projection space. However, when the system is overdetermined ( $M > N$ ), the dimension of the back projected vector  $\mathbf{c}$  is less than the dimension of the originally measured vector  $\mathbf{b}$ .

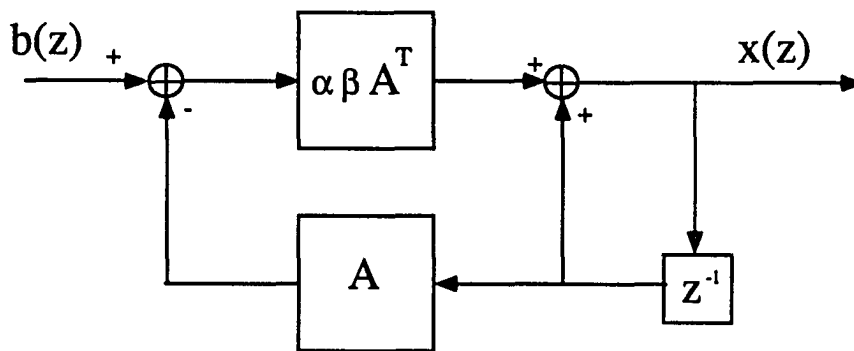


Fig. 3.3. A block diagram of the SIRT.

### 3.2.3 Convergence of SIRT

If numerical noise is not present, the SIRT expressed by eq. 3.13 guarantees convergence to a solution irrespective of whether the system is overdetermined, underdetermined or undetermined. However, the solution may not be unique.

It is evident from eq. 3.13 that, if the error corrections,

$$\mathbf{A}^T[\mathbf{b} - \mathbf{A} \mathbf{x}(\hat{\mathbf{k}})] = \mathbf{0} \quad (3.15)$$

then, the solution converges after the  $\hat{\mathbf{k}}^{\text{th}}$  iteration.

When a system is overdetermined, or undetermined, i.e., the rank of  $\mathbf{A}$  is less than  $M$ . The null space of  $\mathbf{A}^T$  is then not empty, and

there exists  $\mathbf{e} \perp$  range of  $\mathbf{A}$ ,

where  $\mathbf{b} - \mathbf{A} \mathbf{x}(\hat{\mathbf{k}}) = \mathbf{e} \neq \mathbf{0}$ ,

such that (3.16)

$$\mathbf{A}^T \cdot \mathbf{e} = \mathbf{0},$$

and  $\mathbf{A}^T[\mathbf{b} - \mathbf{A} \mathbf{x}(\hat{\mathbf{k}})] = \mathbf{0}$ .

In this case, the rank of  $\mathbf{A}$  is less than  $M$  and the residuals in the projection space may not converge to zero. However, the errors in the image space converge to the null space of the matrix  $\mathbf{A}^T$ . To emphasize the point further, the error corrections in the image space converge to zero even though the residuals in the projection space may not converge to zero.

When  $M = N$  or  $M < N$ , the system is said to be exactly determined or underdetermined respectively. In these cases, there exists at least one  $\hat{\mathbf{k}}$  satisfying

$$\mathbf{b} - \mathbf{A} \mathbf{x}(\hat{\mathbf{k}}) = \mathbf{0} \quad (3.17)$$

When the rank of  $\mathbf{A}$  is equal to  $M$ , there exist solutions for  $[\mathbf{b} - \mathbf{A} \mathbf{x}]$  and the residuals in the projection space converge to zeros. Hence, the condition for convergence expressed in eq. 3.15 is still satisfied. However, when the system is underdetermined, i.e.,  $M < N$ , the

solution obtained using SIRT is not guaranteed to be unique since there are infinitely many values of  $\mathbf{x}(\mathbf{R})$ 's satisfying eq. 3.17. An uncertain component in the null space of  $\mathbf{A}$  consequently exists in the image space. The corresponding component in the solution vector,  $\mathbf{x}$ , can be caused by computational errors accumulated during the iterative process.

### **3.3 Optoelectronic Implementation**

In this section, an optoelectronic implementation of SIRT using SLM and CCD arrays as basic building blocks is introduced. The exact types of the SLM and CCD arrays are not specified in the proposed schemes. For example, the SLM arrays can be liquid crystal television displays and the CCD arrays can be solid state image detectors used in television cameras. In section 3.3.1 and section 3.3.2, methods for performing parallel forward and back projections using coupled SLM and CCD array pairs are explained. The overall structure is presented in section 3.3.3.

#### **3.3.1 Optoelectronic Forward Projection Processor**

As shown in Fig. 3.1, ray-sums of a projection are obtained from strip integrations of pixel gray levels along areas intercepted by grids of pixels on the image plane and paths of rays in the projection. A forward projection from the reconstructed image is a duplication of the operation performed on the original image except that it is taken from the reconstructed image rather than the object under test. In Fig. 3.4, a 2-D SLM array is placed in front of a 1-D CCD array at an angle. The integrations are performed

simultaneously by projecting the 2-D image pattern from the 2-D SLM array into the 1-D strip detector array. The 2-D SLM array represents the reconstructed cross-sectional image and the 1-D CCD array collects the projected pattern of the image according to the geometrically intercepted fractional areas along each strip at the given angle. The operation on the SLM/CCD array pair merely duplicates the original projection operation shown in Fig. 3.1 except that it is taken on the reconstructed image. The optoelectronic structure allows the matrix-vector-multiplication associated with the forward projection matrix at the  $q^{\text{th}}$  angle,  $A_q$ , to be performed by a single optical projection between the SLM/CCD pair.

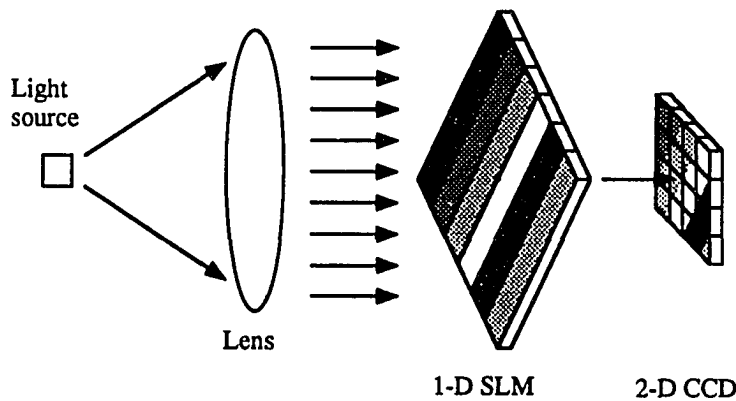


Fig. 3.4. An optoelectronic forward projection processor using a 2-D SLM array and a 1-D CCD.

### 3.3.2 Back Projection

A back projection, which is just an inverse of the forward projection operation, smears the data from the 1-D projection space back to the 2-D image space with the same intercepted fractional areas between projection strips and image pixels. In Fig. 3.5, a 1-D SLM array is placed in front of a 2-D CCD array, at an angle. The 1-D strip SLM array represents data in the projection space at the given angle and the 2-D CCD array represents the reconstructed image. After the light source is pulsed, the 1-D projected data is superimposed on the previously reconstructed image in proportion to the intercepted areas. The structure allows the matrix-vector-multiplication associated with the back projection matrix at the  $q^{\text{th}}$  angle,  $A_q^T$ , to be implemented using a single optical projection between the SLM/CCD pair.

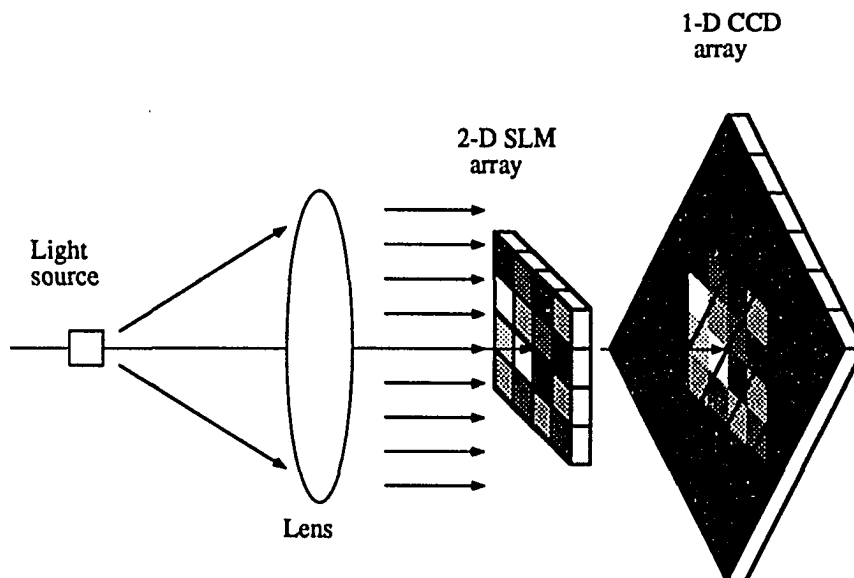


Fig. 3.5. An optoelectronic back projection processor using a 1-D SLM array and a 2-D CCD array.

### 3.3.3 Implementation of SIRT

The SIRT algorithm of eq. 3.13 can also be expressed in terms of projections taken at different angles:

**repeat**

$$x_{old} \leftarrow x_{new}$$

**for**  $q = 1$  **to**  $np$  **do**

$$x_{new} \leftarrow x_{new} + \alpha A_q^T [\hat{b}_q - A_q x_{old}]$$

(3.16)

**end of for**

**until done**

where  $A_q^T$ ,  $\hat{b}_q$  and  $A_q$  are submatrices or subvector of  $A^T$ ,  $b$  and  $A$  corresponding to the  $q^{\text{th}}$  angle respectively and  $np$  is the total number of projections from all the measured angles.

The structure is shown in Fig. 3.6. Forward projections are performed by the pair of arrays SLM2 and CCD2. Back projections are performed by the pair of arrays SLM1 and CCD1.

The iterative procedure using the structure shown in Fig. 3.6 can be described as follows:

**procedure** process for an iteration

**constant**

$b_q$ :  $q = 1$  to  $np$ , measured projection at the  $q^{\text{th}}$  angle;

**variable**

$x_{new}$ : in CCD1, reconstructed image;

$x_{old}$ : in SLM2, reconstructed image from the last iteration;

1. Postprocess the image obtained from the last iteration (contents of CCD1) and then load it into SLM2 and CCD1 as  $x_{old}$  and the initial value of  $x_{new}$  respectively.
2. **for**  $q=1$  to  $np$  **do**
3.       Rotate SLM1 and CCD2 to the  $q^{th}$  projection angle;
4.       Forward project  $x_{old}$ , the reconstructed image from the 2-D array SLM2 into the 1-D array CCD2, thereby generating  $[A_q x_{old}]$ .
5.       Determine errors in projection space,  $[b_q - A_q x_{old}]$ , by subtracting the reconstructed projection from the measured projection.
6.       Load the errors into SLM1 after scaling their magnitudes up to the maximum dynamic range of the device.
7.       Scale the back projection exposure period down by the same ratio as the scaling up factor used in step 6 and back project error corrections from the 1-D SLM1 into the reconstructed image in the 2-D CCD1. The result in CCD1 is

$$x_{new} = x_{old} + \alpha \sum_{i=1}^q A_i^T [\hat{b}_i - A_i x_{old}] \quad (3.17)$$

8.       **end of for**
9.       **end of the iteration.**

A scaling factor is used in steps 6 and 7 to eliminate the effects of finite dynamic range. The factor will be described in the following section.

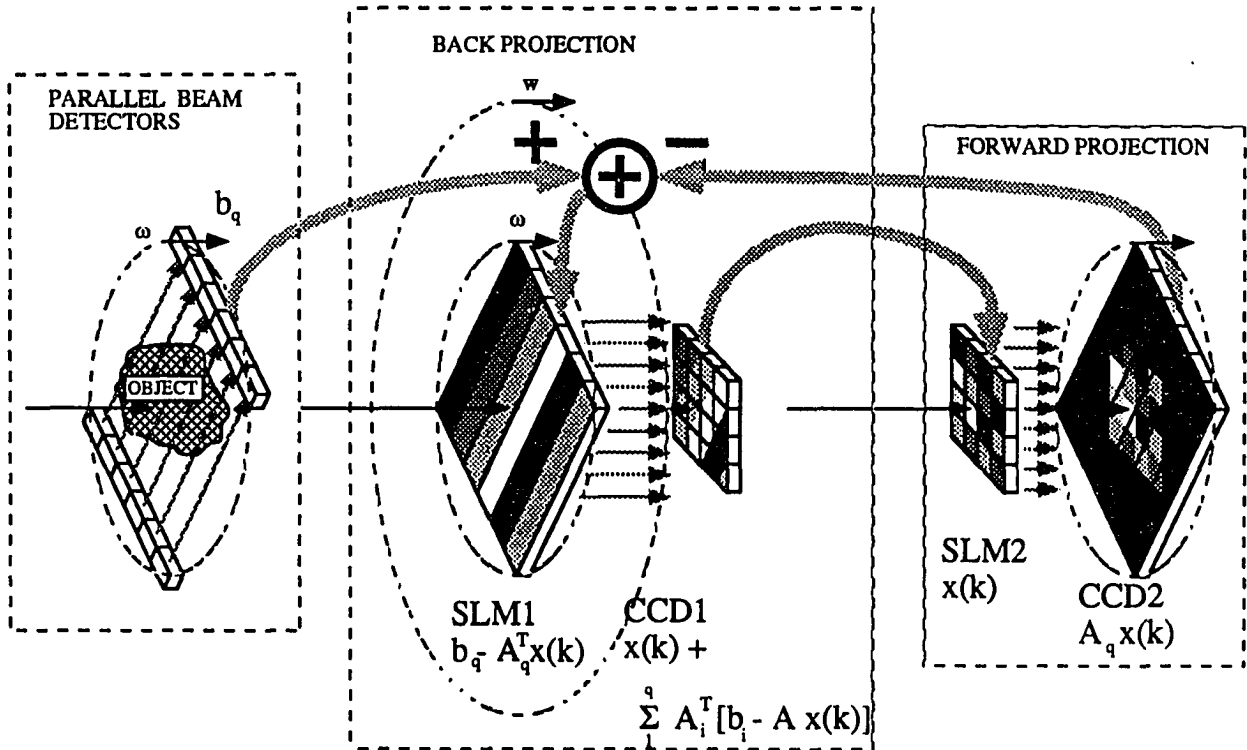


Fig. 3.6. An iterative optoelectronic structure implementing SIRT.

### **3.4 Issues relating to Optoelectronic Implementation**

Since the proposed structure is essentially analog in nature, degradation in the performance caused by limitations of the optoelectronic devices have to be taken into account. Several sources of degradation are discussed in the section. The first source of degradation is caused by the finite dynamic range of the devices. The finite dynamic range arises due to the fact that there are only finite number of distinguishable gray levels which the optoelectronic device can generate. The second source of degradation is related to the nonlinear nature of the devices. The degradation in performance can also be caused by non-uniform distribution of light intensity incident on a plane from a point source. The effect of random generated noise, which may be caused by the dark current of the CCD array, is also discussed.

#### **3.4.1 Finite Dynamic Range**

The number of distinguishable gray levels associated with CCD's is usually considered to be higher than those of SLM's. Hence, only the effects from SLM arrays are discussed here. For a typical liquid crystal television display, about two hundred distinguishable gray levels can be obtained.

The effect of the finite dynamic range of the back projection SLM can be minimized by scaling the magnitudes of the error terms up and then scaling the exposure period down correspondingly in steps 6 and 7 of the algorithm in section 3.3.3. In the feedback configuration, the magnitudes of the error correction terms decrease as the number of

iterations increase. Therefore, the distortions caused by finite dynamic ranges of the device can be minimized by scaling the magnitudes of the errors up to the full range of the back projection SLM and then obtaining the proper error corrections by controlling the time interval of exposure accordingly. The factors of scaling can be estimated in advance for each iteration. The back projection SLM and CCD operate at their maximum dynamic ranges, although magnitudes of error corrections keep decreasing as the number of iterations increase. Consequently, the number of distinguishable gray levels of a reconstructed image does not depend on the back projections any longer and instead depends on the number of distinguishable gray levels of the forward projection operations only. Therefore, the performance of the proposed structures will rely on the 2-D SLM array used for forward projections. The image in the forward projection SLM is updated only once during each iteration and consequently the response time of the forward projection SLM array is not as critical from the perspective of overall system processing speed. The less stringent response time requirement results in more choices for selecting the device.

### 3.4.2 Effects of Nonlinear Elements

SLM's and CCD's are not perfectly linear devices. In general, the degree of nonlinearity of SLM's is usually worse than those of CCD's. Fig. 3.7 shows the relationship between the input voltage and the transmitted intensity for GaAs/AlGaAs-based CCD/MQW SLM's [55-56]. In the block diagram of Fig. 3.8, block  $N(\mathbf{k})_B$  and  $N(\mathbf{k})_F$  can

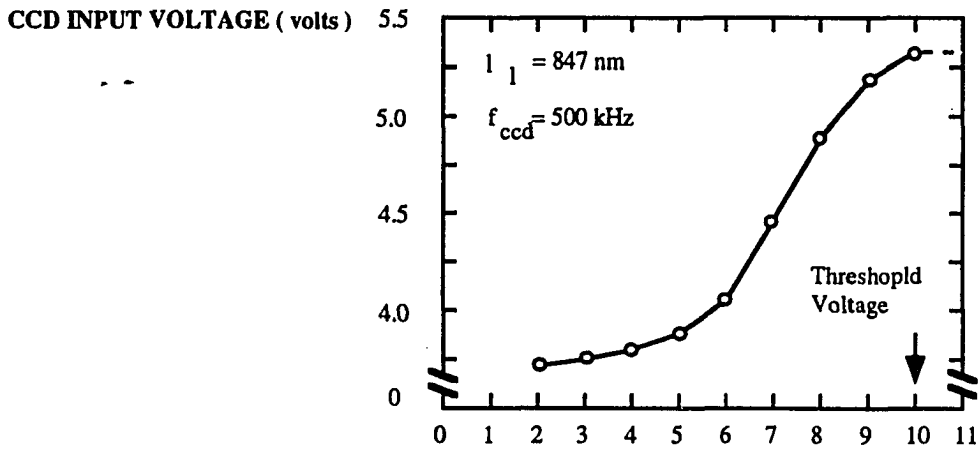


Fig. 3.7. A nonlinear response curve of GaAs/AlGaAs Multiple Quantum Well SLM [55-56].

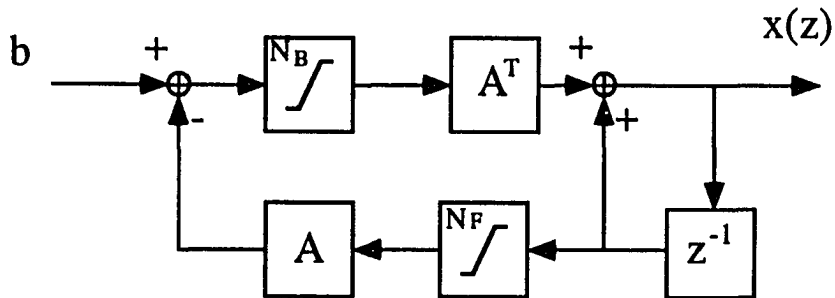


Fig. 3.8. A block diagram for the optoelectronic implementation of SIRT with nonlinear functions of forward projection and back projection SLM arrays.

be treated as nonlinear functions of the back projection and forward projection data corresponding to SLM1 and SLM2 respectively.

The system can be described as

$$\begin{aligned} \mathbf{x}(k) &= \mathbf{x}(k-1) + \mathbf{A}^T \mathbf{N}(k)_B [\mathbf{b} - \mathbf{A} \mathbf{N}(k)_F \mathbf{x}(k-1)] \\ &= [\mathbf{I} - \mathbf{A}^T \mathbf{N}(k)_B \mathbf{A} \mathbf{N}(k)_F] \mathbf{x}(k-1) + \mathbf{A}^T \mathbf{N}(k)_B \mathbf{b} \end{aligned} \quad (3.18)$$

where  $\mathbf{N}(k)_B$  and  $\mathbf{N}(k)_F$  are diagonal matrices reflecting the nonlinear functions.

If the system is stable, then, the final value of the reconstructed image is given by

$$\begin{aligned} \lim_{k \rightarrow \infty} \mathbf{x}(k) &= [\mathbf{A}^T \mathbf{N}_B \mathbf{A} \mathbf{N}_F]^{-1} \mathbf{A}^T \mathbf{N}_B \mathbf{b} \\ &= \mathbf{N}_F^{-1} [\mathbf{A}^T \mathbf{N}_B \mathbf{A}]^{-1} \mathbf{A}^T \mathbf{N}_B \mathbf{b} \\ &\approx \mathbf{N}_F^{-1} [\mathbf{A}^T \mathbf{A}]^{-1} \mathbf{A}^T \mathbf{b} \end{aligned} \quad (3.19)$$

where  $\mathbf{N}_B$  and  $\mathbf{N}_F$  correspond to the final value of  $\mathbf{N}(k)_B$  and  $\mathbf{N}(k)_F$ .

In eq. 3.19,  $\mathbf{N}_B$  is neglected since its effect on the solution is secondary. Instead, we consider the effect of the nonlinearity on the back projection first. The term  $[\mathbf{A}^T \mathbf{N}_B \mathbf{A}]^{-1} \mathbf{A}^T \mathbf{N}_B \mathbf{b}$  is equivalent to a least squares solution of a system

$$\mathbf{N}_B^{-\frac{1}{2}} \mathbf{A} \mathbf{x} = \mathbf{N}_B^{-\frac{1}{2}} \mathbf{b}$$

which minimizes (3.20)

$$\| \mathbf{N}_B^{-\frac{1}{2}} [\mathbf{A} \mathbf{x} - \mathbf{b}] \|_2 .$$

The effect of nonlinearity on the back projection affects the distribution of the residuals. Therefore, the distortion associated with back projections can be neglected since the magnitude of the residuals are much smaller than the magnitude of the solution.

The effect of the nonlinear nature of the forward projection SLM cannot be neglected since it lies in the signal path. However, the effect is only to stretch the gray levels of reconstructed images. When a gray level of a pixel lies in the region of saturation of the SLM, the magnitude of the pixel is clamped at a constant value. Hence, the nonlinear character of the SLM functions acts as a constraint on the values of the solution. Similarly as discussed in Section 4.2.2, the constraints on the values of the solution tends to make the system relatively more overdetermined. The net effect of this constraint is to ensure that the least squares solution is obtained in a reduced space.

### 3.4.3 Effects of Nonuniform Distribution of Light Intensity

Another source of distortion is caused by the nonuniform distribution of the incident light intensity over SLM arrays. This can be caused by the Gaussian beam dispersion character of lasers. Let  $D_B$  and  $D_F$  be  $N \times N$  diagonal matrices representing the light intensity distributions of the back and forward projections respectively and let  $C(k)$  be an  $N \times 1$  vector with identical elements representing the value of zero bias added during the back projection operation at the  $k^{\text{th}}$  iteration. The block diagram is shown in Fig. 3.8 and the system can be described as

$$\mathbf{x}(k) = \mathbf{x}(k-1) + D_B \mathbf{A}^T [\mathbf{b} + C(k) - \mathbf{A} D_F \mathbf{x}(k-1)] - \mathbf{A}^T C(k) \quad (3.21)$$

where the zero bias  $C(k)$  is added to the data to be projected before back projecting and subtracted from the image after each iteration. The final image is given by

$$\begin{aligned}
 \lim_{k \rightarrow \infty} x(k) &= [D_B A^T A D_F]^{-1} [D_B A^T b + [D_B - I] A^T C] \\
 &= D_F^{-1} [A^T A]^{-1} A^T b + D_F^{-1} [A^T A]^{-1} D_B^{-1} [D_B - I] A^T C \\
 &\approx D_F^{-1} [A^T A]^{-1} A^T b
 \end{aligned} \tag{3.22}$$

where  $C = \lim_{k \rightarrow \infty} C(k)$ .

The term in eq. 3.22 associated with  $C$  is caused by zero bias and its effect can be reduced. As the magnitudes of zero bias is adjusted down as the reconstructed image converges to the final solution, the magnitude of  $C$  can also be reduced. If positive and negative valued error corrections are projected separately as mentioned in section 6.7, the zero bias term tends to cancel out. The  $D_F^{-1}$  corrects the distortion caused by  $D_F$  at the forward projection and the distortion is canceled out if an output image is taken from the image used for forward projections. If the light intensity decreases as we move from the center to the edge of an image, the term associated with  $D_F^{-1}$  causes the brightness of the reconstructed image to increase from the center to the edge of the reconstructed image directly obtained from the back projection CCD array.

### 3.4.4 Random Noise and Stability

A dark voltage is generated in CCD cells as a result of build up caused by dark current. The effect of the dark voltage can be minimized by subtracting the average value

from the CCD output after each iteration. Then, the residuals can be treated as random noise.

If the system is overdetermined or exactly determined, then the effect of this random noise can be minimized by the feedback scheme of the SIRT algorithm. When a system is underdetermined, i.e. the number of ray sums,  $M$ , is less than the number of pixels,  $N$ , the matrix  $[A^T A]$  becomes singular. Components of the noise perpendicular to the null space of the matrix  $A$  will remain and accumulate in the image space. Consequently, convergence of the SIRT algorithm is not guaranteed. The problem of poor convergence is addressed in the next chapter where a new algorithm which guarantees convergence to a unique solution when the system is underdetermined is presented.

### 3.5 Simulation Results

In order to assure the validity of the scheme, the system was simulated. The effects of limited dynamic range, nonlinearity, and random additive noise associated with optoelectronic devices have been included in the simulation model. Results of the simulation are presented in this section. The Shepp and Logan phantom is used as a test cross-sectional image throughout the simulation exercise. The phantom is described in section 3.5.1. In order to model the intercepted fractional areas of optical projections in the free space, the weight factors,  $w_{ij}$ 's in eq. 3.1, are calculated exactly in the simulations. The mapping errors, introduced as a result of the fact that the original measured projections are taken from continuous cross-sectional plane and the images are reconstructed on a discrete

plane, are included. Projections are usually taken from an image with higher spatial resolution. The image is, however, reconstructed with lower spatial resolution.

### 3.5.1 Shepp and Logan Phantom

The Shepp and Logan phantom [75, 10] is a commonly used test cross-sectional image in tomographic image reconstruction. The phantom is specified in Fig. 3.9 and Table 3.1. Projections can be calculated directly from the given parameters of the ten ellipses or obtained by taking discrete Radon integrations from the image constructed using the given data.

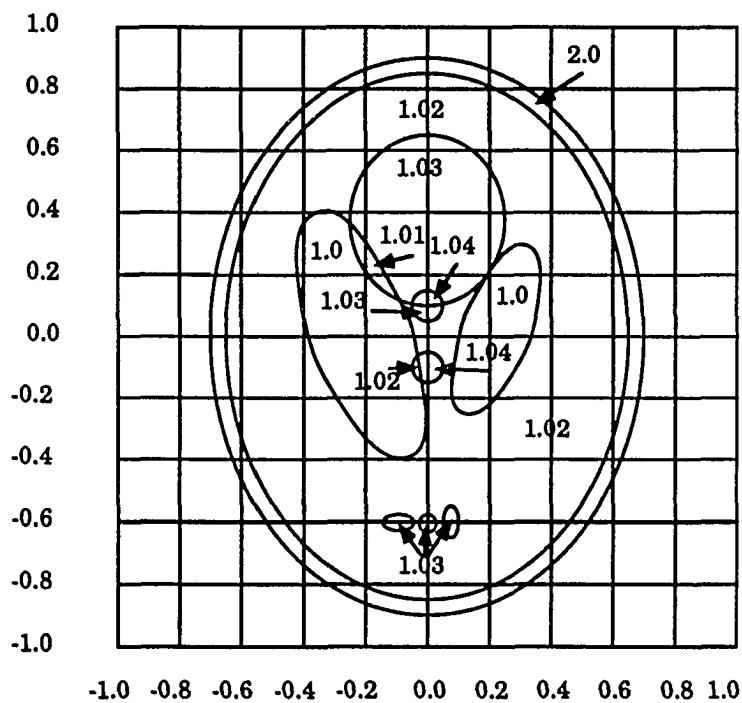


Fig. 3.9. A Shepp and Logan Phantom consisting of ten ellipses [10, 75].

**Table 3.1. Parameters of the Shepp and Logan Phantom [10, 75].**

<i>Center Coordinate</i>	<i>Major Axis</i>	<i>Minor Axis</i>	<i>Rotation Angle</i>	<i>Refractive Index</i>
(0, 0)	0.92	0.69	90	2.0
(0, -0.0184)	0.874	0.6624	90	-0.98
(0.22, 0)	0.31	0.11	72	-0.02
(-0.22, 0)	0.41	0.16	108	-0.02
(0, 0.35)	0.25	0.21	90	0.01
(0, 0.1)	0.046	0.046	0	0.01
(0, -0.1)	0.046	0.046	0	0.01
(-0.08, -0.605)	0.046	0.023	0	0.01
(0, -0.605)	0.023	0.023	0	0.01
(0.06, -0.605)	0.046	0.023	90	0.01

In our simulations, an image is built first and then projections are taken from the image using eq. 3.1. The number of gray levels in the image is 200 as specified originally and a plot of a cross-section is shown in Fig. 3.10. However, the details of this phantom can not be observed if the gray levels are not stretched. The number of grey levels in the original phantom is 200, and the reconstructed image consists of real-valued gray levels in the range of 0-255. In order to enhance the contrast of the displayed image, gray levels in the range of 126-134 were stretched after reconstruction to cover the full range of the display by multiplying by a factor of 32. Fig. 3.11 shows a plot of the cross-section after contrast stretching.

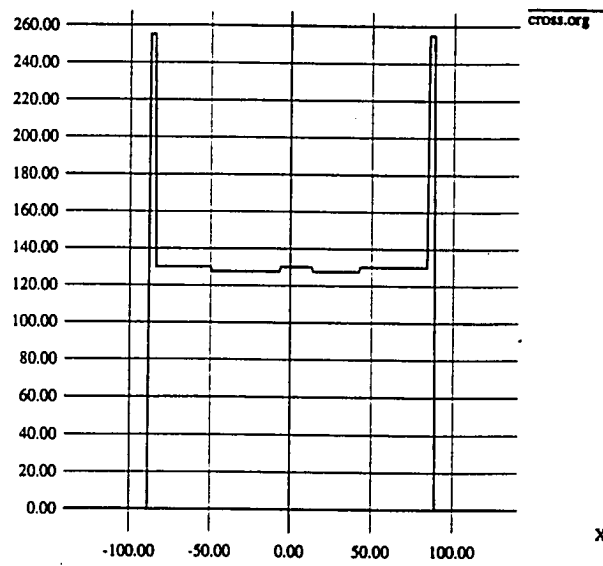


Fig. 3.10. A cross-section of the original phantom and actually reconstructed images.

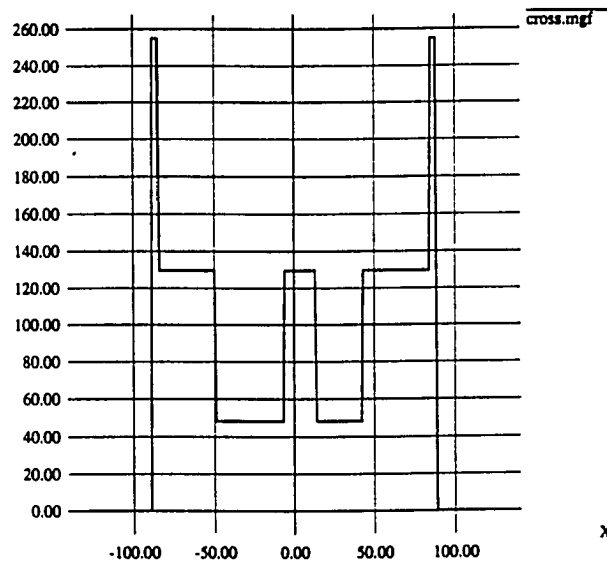


Fig. 3.11. A cross-section of displayed images after contrast stretching.

### 3.5.2 SIRT Simulation

Fig. 3.12 shows reconstructed images as a function of the number of iterations. These images are reconstructed using the basic SIRT algorithm. Projections are obtained by strip integrating the 512×512 original cross-sectional image. The dimensions of reconstructed images are 128×128. The system is overdetermined ( $M > N$ ) with the number of projections set at 180. The width of ray-sums is the same as those of the pixels. Each projection covers the whole image plane.

### 3.5.3 Simulation The Effects of Limited Dynamic Range

Fig. 3.13 and Fig. 3.14 show the results obtained by simulating SLM arrays with 1024 and 256 distinguishable grey levels respectively. The finite number of gray levels is simulated by scaling the maximum pixel value to the maximum dynamic range and then quantizing properly. Fig. 3.14 shows that, when the number of distinguishable gray levels of the forward projection SLM array is reduced to 256, the reconstructed images show severe distortion. The results show that, for implementing the SIRT, the critical device parameter effecting the quality of reconstructed images is the number of distinguishable grey levels of the 2-D forward projection SLM array. This is consistent with the analysis given in section 3.4.1.

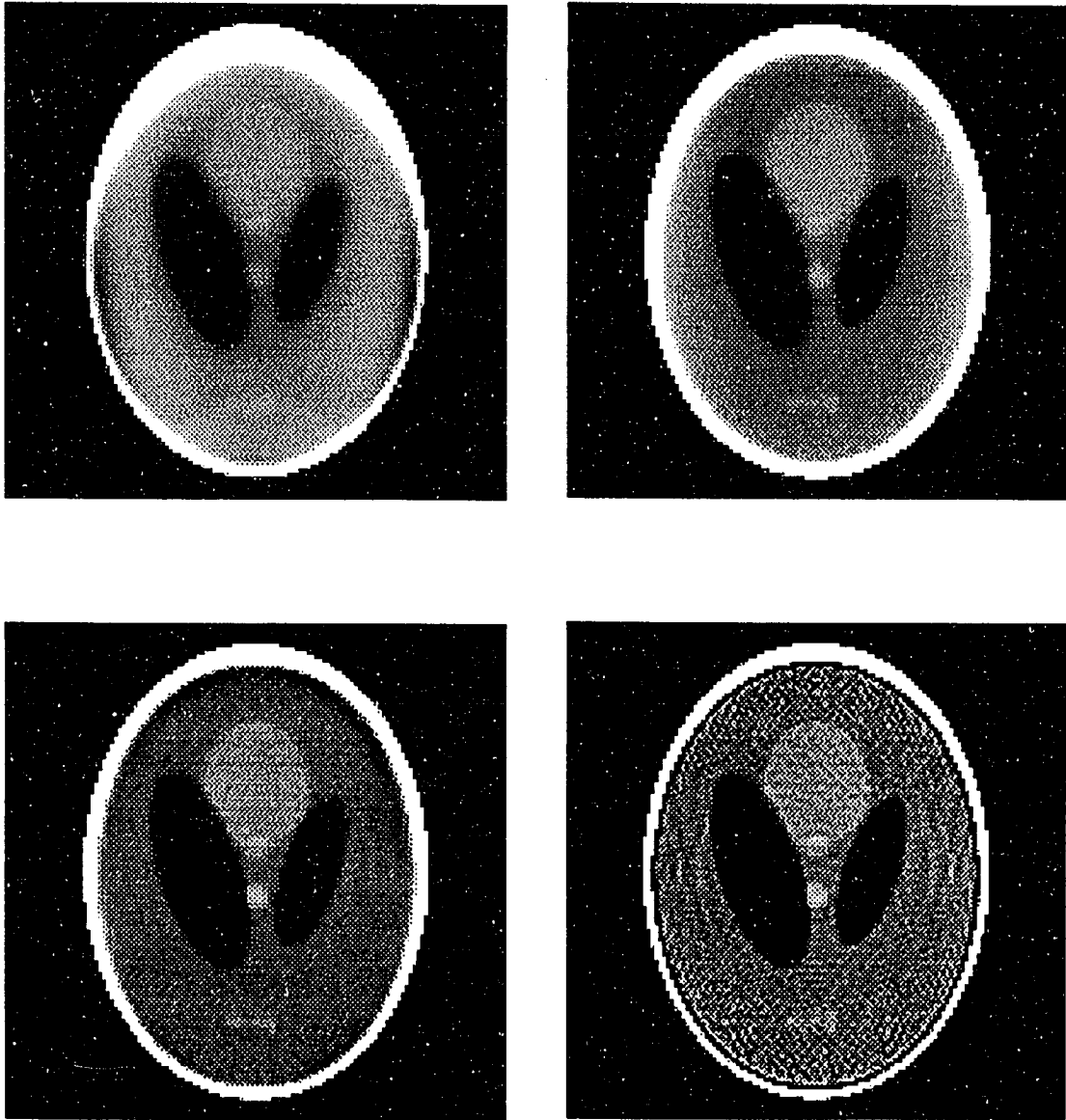


Fig. 3.12. Reconstructed image obtained using the SIRT at the 16<sup>th</sup>, 32<sup>nd</sup>, 64<sup>th</sup> and 256<sup>th</sup> iterations.

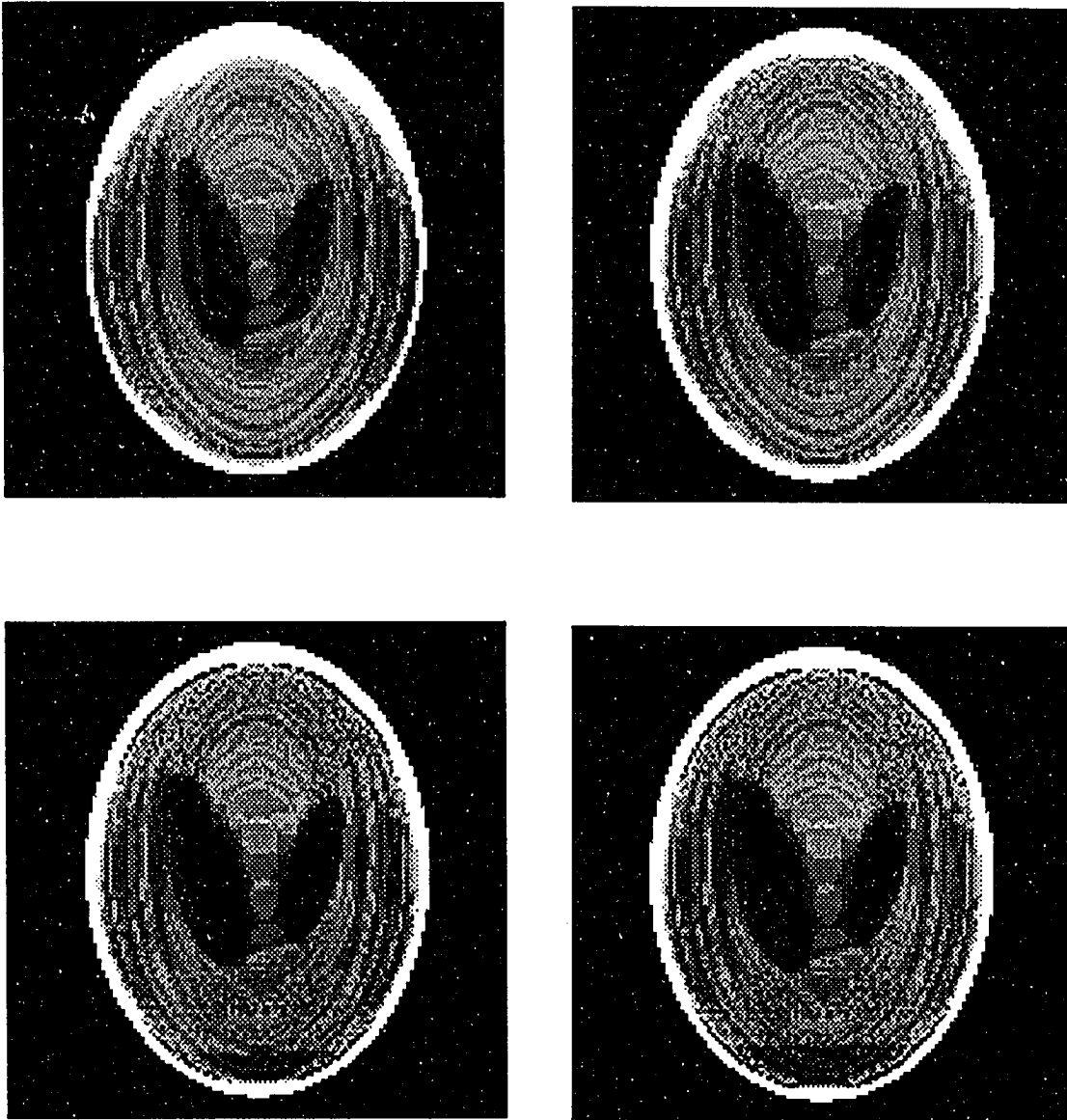


Fig. 3.13. Reconstructed images at 16<sup>th</sup>, 32<sup>nd</sup>, 64<sup>th</sup> and 128<sup>th</sup> iterations where the number of distinguishable gray levels of the forward projection SLM is set at 256..

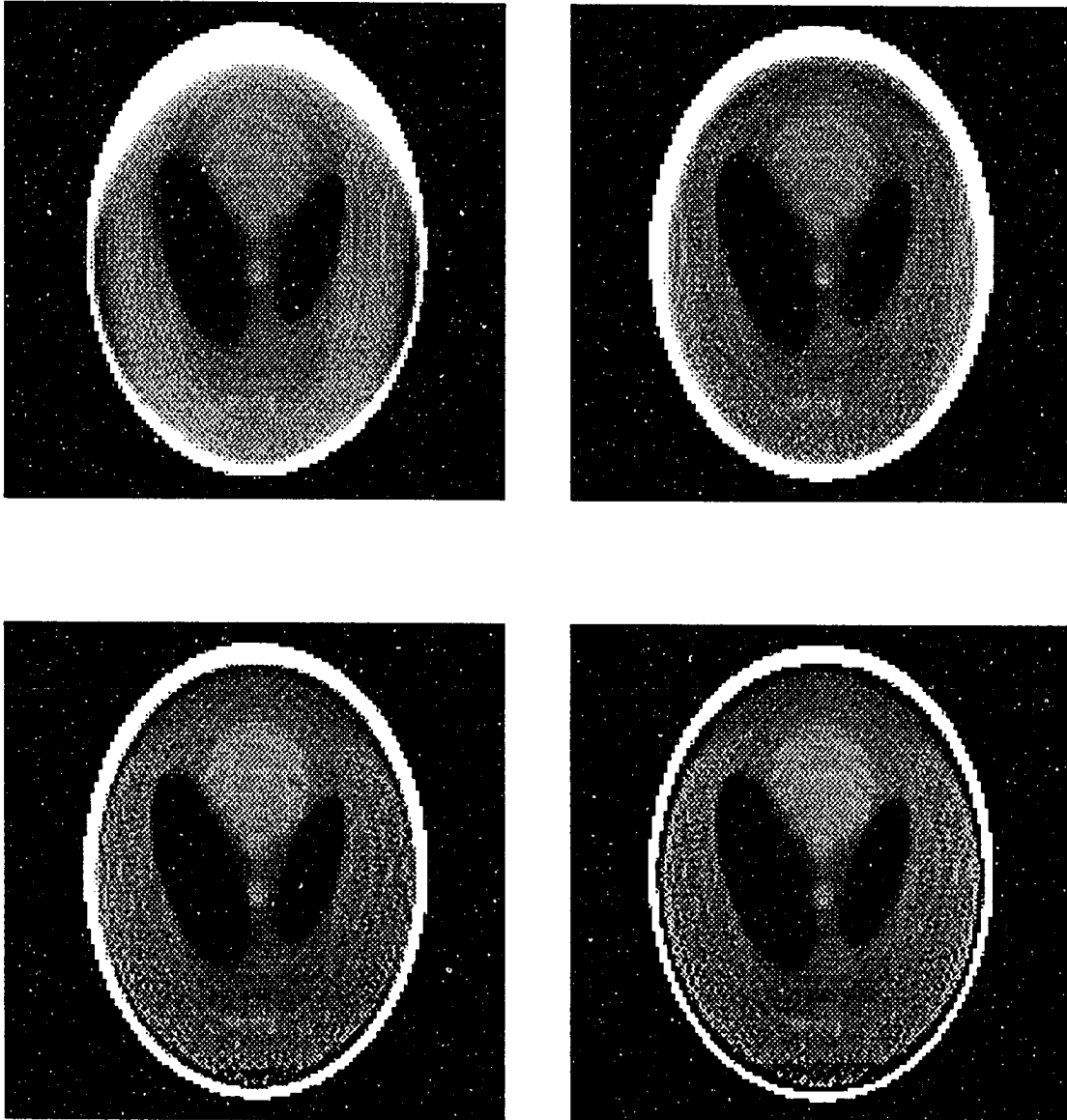


Fig. 3.14. Reconstructed images at the 16<sup>th</sup>, 32<sup>nd</sup>, 64<sup>th</sup> and 128<sup>th</sup> iterations where the number of distinguishable grey levels of the forward projection SLM is set at 1024.

### 3.5.4 Simulation of Device Nonlinearity

In this simulation, the nonlinear response curve in Fig. 3.7 is approximated using a fifth order polynomial

$$f(x) = [y - 3.808249] \times 202.3996$$

where

$$y = 0.000032051z^5 - 0.0033741z^4 + 0.063091z^3 - 0.41208z^2 + 1.1307z + 2.46$$

$$2.0 \leq z \leq 10.0 \quad (3.23)$$

$$\text{and } z = \frac{5 \times x}{256} + 4.5$$

The nonlinear function is employed during the back and forward projection operations separately. The result shown in Fig. 3.15 is consistent with the analysis given by eq. 3.19, where it was shown that the nonlinear nature of the SLM only contributes to a minor warping of the grey levels in the reconstructed images.

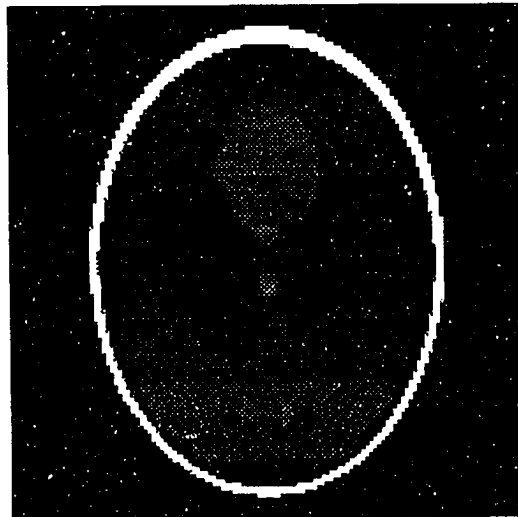


Fig. 3.15. Reconstructed image under the effect of nonlinearity on SLM arrays.

### 3.5.5 Divergence of SIRT under Random Noise

In this simulation, the system is underdetermined. The dimensions of the reconstructed image are  $256 \times 256$ . The number of projections are 120 and there are 121 ray-sums in each projection. Therefore, the ratio of  $M$  to  $N$  is 0.22 where  $M$  and  $N$  are dimensions of the matrix  $A$  in eq. 3.13. Uniformly distributed noise in the range of  $-0.5$  to  $+0.5$  is added to the reconstructed image after each iteration. The SNR is 48.27 dB. Fig. 3.16 shows the plot of the residuals corresponding to the number of iterations. Fig. 3.17 shows the reconstructed image at different iterations. The result clearly begins to diverge after approximately one hundred iterations.

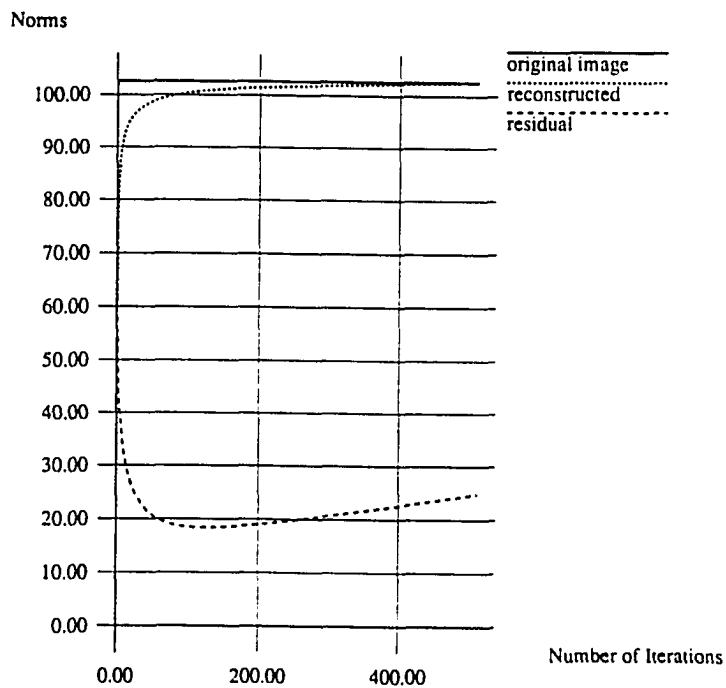


Fig. 3.16. A plot of residual vs. the number of iterations (SIRT,  $M:N = 0.22$ ).

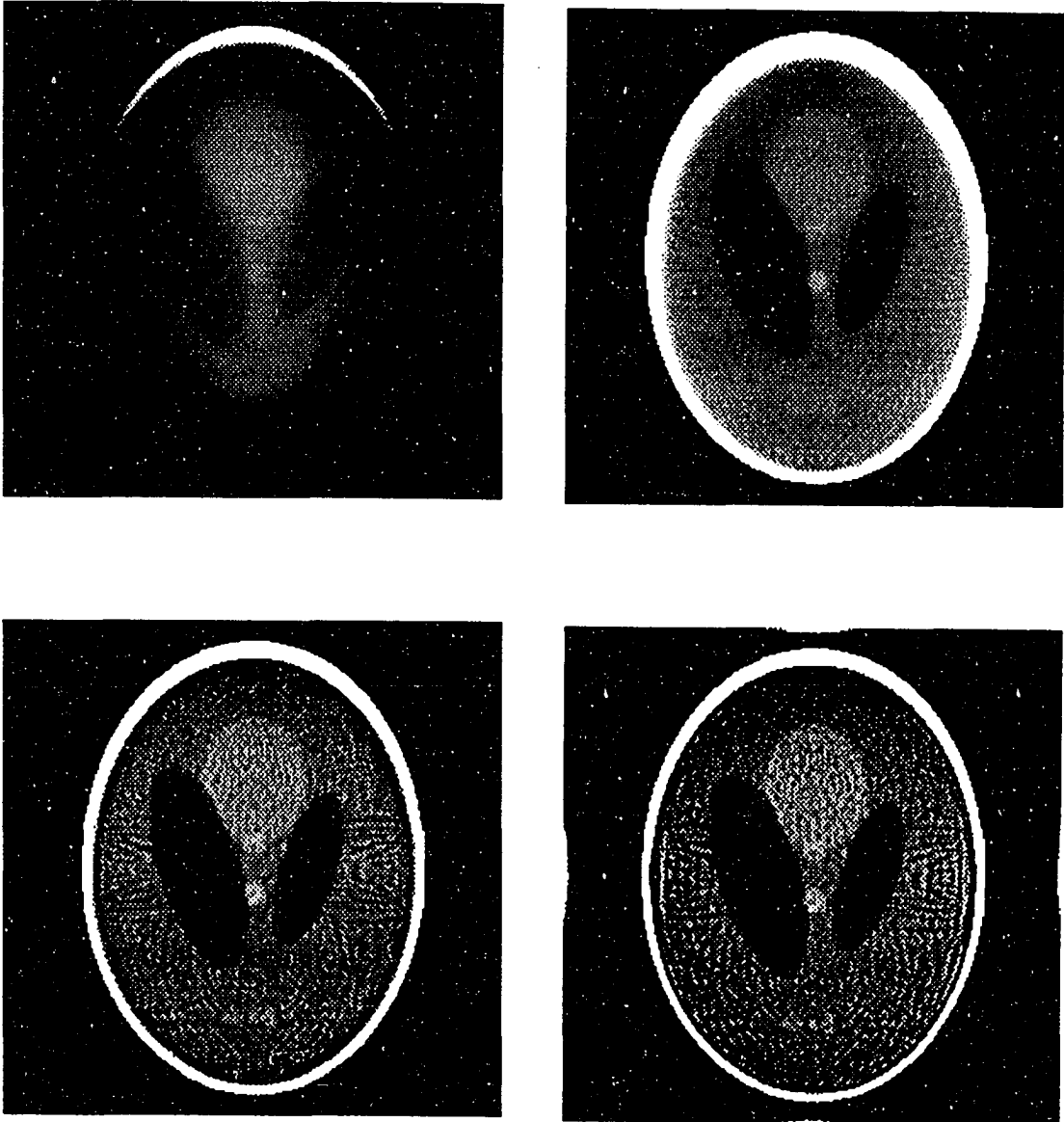


Fig. 3.17. Reconstructed images at the 16<sup>th</sup>, 32<sup>nd</sup>, 64<sup>th</sup> and 512<sup>th</sup> with additive noise in the image space.

### 3.6 Summary

The Simultaneous Iterative Image Reconstruction algorithm - SIRT has been discussed in this chapter from the point of view of the method of least squares solutions for overdetermined systems. A scheme for implementing the algorithm is also presented.

Optical computing offers the major advantages of massive parallelism and free space connectivity. These advantages can be exploited fully in tomographic image reconstruction. In the optical implementation of tomographic image reconstruction algorithm, the time consuming matrix-vector-multiplications associated with the back and forward projection operations are replaced by parallel optical projections. The inaccuracy associated with interpolations and approximations linked to tomographic projection operations are overcome since the intercepted fractional areas of free space optical projections are exact. In addition, iterative algorithms offer two major advantages over direct algorithms when implemented using optoelectronic devices. With iterative algorithms, the dynamic range of optoelectronic devices can be fully exploited. In addition, there is no need for filtering or convolution operations. The optoelectronic structures described in this Chapter can be built using TV devices and mechanical image rotators that are commercially available. In the future, the performance of the proposed structures can be considerably enhanced by using higher speed SLM's and static image rotation devices.

The presence of noise and optical distortion prevents optical implementations of direct reconstruction algorithms using optical Fourier Transforms with an acceptable level of performance. However, the accuracy of the reconstruction can be enhanced using the

feedback scheme proposed in this Chapter. In other words, a less accurate optical filter can be used with the optoelectronic implementation in order to speed up the reconstruction. An improved algorithm and optoelectronic structure which implements the Iterative Filtered Back Projection (IFBP) image reconstruction algorithm is presented in Chapter 5.

In many applications, reconstruction of high spatial resolution images from fewer measured data is desired. The situation represents an underdetermined systems since the number of unknowns to be solved for, is more than the amount of measured data. It has been pointed out that, for an underdetermined system, the conventional SIRT algorithm does not guarantee unique convergence if numerical errors are present during computation. This problem is remedied in a new technique called Projection Iterative Reconstruction Technique which is described in the following chapter. An optoelectronic system for implementing the algorithm follows introduction to the novel approach.

## **CHAPTER 4. PROJECTION ITERATIVE RECONSTRUCTION TECHNIQUE AND ITS OPTOELECTRONIC IMPLEMENTATION**

This Chapter introduces the Projection Iterative Reconstruction Technique (PIRT) as an iterative tomographic image reconstruction scheme for solving underdetermined systems. The PIRT guarantees convergence to a unique minimum-norm solution for an underdetermined system. Since, the state matrix associated with the PIRT is symmetric and positive definite, it allows application of the conjugate gradient method for solving underdetermined systems without the need for imposing explicit constraints.

In many applications of tomographic image reconstructions, images of higher spatial resolution are desired to be reconstructed from limited data. In all of these cases, the number of unknowns to be solved for, is more than the number of measurements. This results in an underdetermined system.

When a system is underdetermined, the SIRT algorithm described in Chapter 3 converges to the minimum-norm solution, if the initial value is selected properly and no numerical error is introduced during computing. However, numerical errors are unavoidable in most situations. This is particularly true for the optoelectronic implementation proposed in the previous chapter. In this case, the result obtained using SIRT will diverge as discussed in Section 3.2.3 and shown in Fig. 3.17. Consequently, there is interest in other algorithms where a unique solution is guaranteed when the system is underdetermined.

The conjugate gradient method is an efficient acceleration technique for solving large and sparse linear systems and has been used extensively in conjunction with the SIRT. Since, the conjugate gradient method is guaranteed to converge only when a system is symmetric and positive definite, it cannot be applied for solving underdetermined systems without imposing explicit constraints. Since the state matrix associated with the PIRT is symmetric and positive definite, the conjugate gradient method can be directly applied without the need for constraints.

Section 4.1 introduces the PIRT as a method based on the minimum-norm solution of the normal equation method and the basic iterative Richardson (RF) method for solving linear systems. Section 4.2 discusses issues related to the PIRT, including, solutions with *a priori* information, solutions under constraints, conditions of convergence and geometric considerations for underdetermined systems in tomographic image reconstruction. Section 4.3 describes the use of the conjugate gradient method for solving underdetermined systems. Section 4.4 represents a scheme for implementing the algorithm using optoelectronic devices. Simulation results and a Summary are presented in Section 4.5 and 4.6 respectively.

#### **4.1 Projection Iterative Reconstruction Technique**

The PIRT is an iterative tomographic image reconstruction algorithm which can be considered as a counterpart of the SIRT. The SIRT leads to the least-squares solution of the normal equations for overdetermined systems by correcting errors in the solution in the

image space iteratively. This is in contrast to the PIRT which yields the minimum-norm solution of the normal equations for underdetermined systems by building up a state space vector in the projection space iteratively.

#### 4.1.1 Minimum-Norm Solution

Consider a system,  $\mathbf{A} \mathbf{x} = \mathbf{b}$ , where  $M < N$ . If the  $M$  rows of the  $M \times N$  matrix  $\mathbf{A}$  are linearly independent, we have an underdetermined system and consequently there are an infinite number of solutions. However, the system has a unique minimum-norm solution. The solution of an underdetermined system which minimizes  $\|\mathbf{x}\|_2$  can be derived as the follows [74]

$$\begin{aligned}
 \text{If} \quad \mathbf{x} &= \mathbf{A}^T \mathbf{t} \\
 \text{where} \quad \mathbf{t} &= [t_1 \ t_2 \ \dots \ t_M]^T \\
 \text{then} \quad \mathbf{A} [\mathbf{A}^T \mathbf{t}] &= \mathbf{b} \\
 \text{or} \quad \mathbf{t} &= [\mathbf{A} \ \mathbf{A}^T]^{-1} \mathbf{b} \\
 \mathbf{x} &= \mathbf{A}^T [\mathbf{A} \ \mathbf{A}^T]^{-1} \mathbf{b}.
 \end{aligned} \tag{4.1}$$

The matrix  $[\mathbf{A} \ \mathbf{A}^T]$  is symmetric and positive definite and therefore a unique solution of  $\mathbf{t}$  exists.

The fact that  $\mathbf{x}$  represents the minimum-norm solution can be shown as follows. The solution of  $\mathbf{x}$  is a linear combination of the linearly independent rows of  $\mathbf{A}$ ,

$$\begin{aligned}
 \mathbf{x} &= \mathbf{A}^T \mathbf{t} \\
 &= t_1 \hat{\mathbf{a}}_1^T + t_2 \hat{\mathbf{a}}_2^T + \dots + t_M \hat{\mathbf{a}}_M^T
 \end{aligned} \tag{4.2}$$

where  $\hat{\mathbf{a}}_i$  is the  $i^{\text{th}}$  row of  $\mathbf{A}$ .

The solution vector  $\mathbf{x}$  minimizes the Euclidian distance from the origin because it is orthogonal to the null space of  $\mathbf{A}$ . This can be shown as follows:

$$\begin{aligned}
 \text{Let } \quad & \mathbf{z} \in \mathfrak{R}^N \quad \text{and} \quad \mathbf{z} \in \text{null space of } \mathbf{A} \\
 \text{then } \quad & \mathbf{A} \mathbf{z} = \mathbf{0} \\
 & \hat{\mathbf{a}}_i^T \cdot \mathbf{z} = 0, \quad \text{for all } i, i \in \{1, 2, \dots, M\}
 \end{aligned} \tag{4.3}$$

$$\text{or} \quad \mathbf{x}^T \cdot \mathbf{z} = 0$$

consequently  $\mathbf{x} \perp \mathbf{z}$  where  $\perp$  denotes orthogonality,

i.e.  $\mathbf{x} \perp$  null space of  $\mathbf{A}$ .

The minimum-norm solution of an underdetermined system can also be derived by minimizing  $(1/2)\mathbf{x}^T\mathbf{x}$  under the equality constraint  $\mathbf{A}\mathbf{x} = \mathbf{b}$  [76].

$$\frac{\partial}{\partial \mathbf{x}} \left\{ \frac{1}{2} \mathbf{x}^T \mathbf{x} - (\mathbf{A}\mathbf{x} - \mathbf{b})^T \boldsymbol{\lambda} \right\} = \mathbf{0}$$

$$\mathbf{x} - \mathbf{A}^T \boldsymbol{\lambda} = \mathbf{0}$$

$$\mathbf{A}^T \boldsymbol{\lambda} = \mathbf{x}$$

$$\mathbf{A} \mathbf{A}^T \boldsymbol{\lambda} = \mathbf{A} \mathbf{x} = \mathbf{b} \quad (4.4)$$

then

$$\boldsymbol{\lambda} = [\mathbf{A} \mathbf{A}^T]^{-1} \mathbf{b}$$

$$\mathbf{x} = \mathbf{A}^T \boldsymbol{\lambda}$$

$$= \mathbf{A}^T [\mathbf{A} \mathbf{A}^T]^{-1} \mathbf{b}$$

where the Lagrangian multiplier  $\boldsymbol{\lambda}$  is equivalent to the state vector  $\mathbf{t}$  in eq. 4.1.

The minimum-norm solution of an underdetermined system for the case of  $M=1$ ,  $N=2$  is shown in Fig. 4.1.

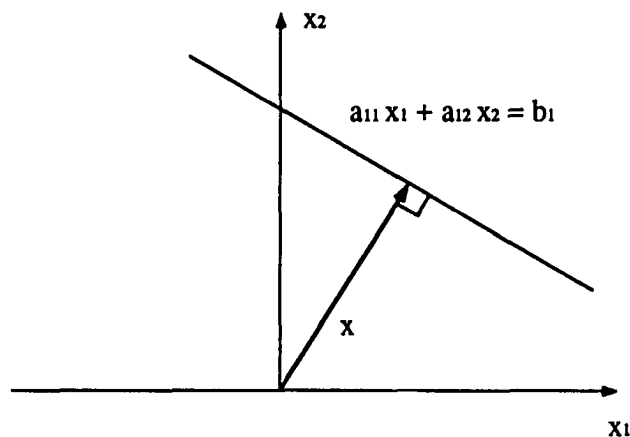


Fig. 4.1. The minimum-norm solution for an underdetermined system where  $M=2$  and  $N=1$  [76].

### 4.1.2 Iterative Method

When a system is underdetermined, i.e.  $M < N$  and all  $M$  rows of  $A$  are linearly independent, the SIRT cannot guarantee convergence to a unique solution since the  $N \times N$  matrix  $[A^T A]$  is not positive definite anymore. However, in eq. 4.1, the  $M \times M$  symmetric matrix  $[A A^T]$  is positive definite and therefore the state variable vector, i.e. the intermediate solution vector  $t$ , can be solved for iteratively. Consequently, the minimum-norm solution of an underdetermined system,  $Ax = b$ , can also be solved for by iteratively solving the equation  $[A A^T]t = b$ . The corresponding state and output equations can be written as

$$t(k) = t(k-1) + \alpha [b - A A^T t(k-1)] \quad (4.5)$$

$$\text{and } x(k) = A^T t(k)$$

where  $k$  is the iteration index and  $\alpha$  is the relaxation coefficient.  $\alpha$  has to be chosen such that the eigenvalues of  $[I - \alpha A A^T]$  lie within the unit circle.

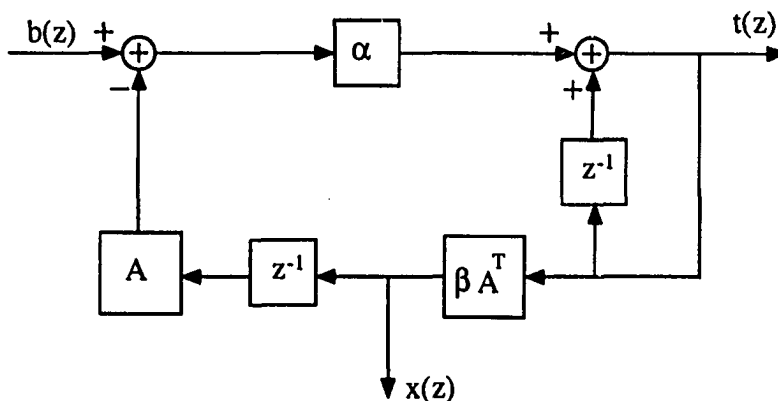


Fig. 4.2. A block diagram of the PIRT.

A block diagram summarizing the steps involved in PIRT is shown in Fig. 4.2. The convergence of eq. 4.5 can be proved by recursively using eq. 4.2 and finding the limit as  $k \rightarrow \infty$ .

$$\begin{aligned}
t(k) &= t(k-1) + \alpha [b - A A^T] t(k-1) \\
&= \alpha b + [I - \alpha A A^T] t(k-1) \\
&= \alpha b + \{[I - \alpha A A^T] [\alpha b + [I - \alpha A A^T] t(k-2)]\} \\
&= \alpha \{I + [I - \alpha A A^T]\} b + [I - \alpha A A^T]^2 t(k-2) \\
&\dots \\
&= \alpha \left\{ \sum_{n=0}^{k-1} [I - \alpha A A^T]^n \right\} b + [I - \alpha A A^T]^k t(0) \\
&= \alpha \{I - [I - \alpha A A^T]\}^{-1} \{I + [I - \alpha A A^T]^k\} b + [I - \alpha A A^T]^k t(0) \\
&= [A A^T]^{-1} \{I - [I - \alpha A A^T]^k\} b + [I - \alpha A A^T]^k t(0)
\end{aligned} \tag{4.6}$$

When  $\|I - \alpha A A^T\| < 1$ , and  $k \rightarrow \infty$ , then

$$[I - \alpha A A^T]^k \rightarrow 0 \tag{4.7}$$

and

$$\lim_{k \rightarrow \infty} t(k) = [A A^T]^{-1} b \tag{4.8}$$

for any finite  $t(0)$ .

The convergence can also be shown by taking z-transforms and invoking the final value theorem,

$$\begin{aligned}
t(z) &= t(z) z^{-1} + \alpha [ b(z) - A A^T t(z) z^{-1}] \\
&= [I - [I - \alpha A A^T] z^{-1}]^{-1} \frac{\alpha b}{1 - z^{-1}}
\end{aligned}$$

$$\begin{aligned}
\lim_{k \rightarrow \infty} t(k) &= \lim_{z \rightarrow 1} [(1 - z^{-1}) t(z)] \\
&= [A A^T]^{-1} b
\end{aligned} \tag{4.9}$$

$$\begin{aligned}
\text{Hence } \lim_{k \rightarrow \infty} x(k) &= A^T \lim_{k \rightarrow \infty} t(k) \\
&= A^T [A A^T]^{-1} b
\end{aligned}$$

This indicates that  $x(k)$  converges to the minimum-norm solution of the underdetermined system as shown in eq. 4.1. Since the state vector  $t$  is equivalent to the Lagrangian multiplier  $\lambda$  in eq. 4.7, this algorithm can be considered as an iterative method for determining the Lagrangian multiplier and the optimum solution simultaneously.

Alternatively, we can determine the minimum-norm solution of the cross-sectional image of an underdetermined system using the PIRT algorithm by rewriting equation 4.5 as

$$t(k) = t(k-1) + \alpha [ b - A x(k-1)] \tag{4.10}$$

$$x(k) = \beta A^T t(k)$$

where  $\beta$  is the coefficient used to normalize the back projections and  $t(k)$  is a state vector which is iteratively built up in the projection space. In this algorithm, the Lagrangian multiplier in the projection space and the minimum-norm solution in the image space are solved for simultaneously. The difference between the PIRT algorithm and the SIRT algorithm in respect of their computational procedure is that, with PIRT, there is an

additional state vector in the projection space and the error corrections are fed back to the projection space instead of in the image space. Consequently, the solution in the image space is uniquely determined by back projecting the reconstructed projections. In contrast, the SIRT does not identify a state vector explicitly and the error corrections are fed back in the image space. Consequently, in the case of PIRT, a unique minimum-norm solution is guaranteed when the system is underdetermined.

## 4.2 Properties of PIRT

In this section, several properties of the PIRT, particularly as they relate to common issues in image reconstruction, are discussed. Section 4.2.1 discusses the impact on the solution obtained with PIRT when an initial image in the recursive process is specified. Effects of constraints on the solution of the PIRT are discussed in Section 4.2.2. In Section 4.2.3, convergence properties of PIRT for overdetermined and undetermined systems are discussed. Issues concerning support regions of solutions and geometrical considerations of projections for underdetermined systems are presented in Section 4.2.4..

### 4.2.1 PIRT with Initial Estimate

In many applications, *a priori* information relating to the cross-sectional image can be obtained before applying iterative algorithms. An initial image can also be used in conjunction with the PIRT in order to improve the reconstruction result as well as speed. When an initial image is given, the solution obtained using PIRT minimizes the Euclidian

distance to the initial image in the image space. This is in contrast to SIRT which minimizes the residual in the projection space.

When the initial image is known, we only need to solve for an image that represents the difference corresponding to the actual measurements and the initial image. This difference in the image space can be obtained from the initial residual in the projection space. The initial residual is found by projecting the initial image into the projection space and comparing it to actual measurements. Finally, the reconstructed image is obtained by superimposing the difference on the initial image.

Let  $x_0$  denote the initial image. We rewrite  $A x = b$  as

$$A [x_0 + \bar{x}] = b_0 + \bar{b} \quad (4.11)$$

where

$$A x_0 = b_0$$

$$A \bar{x} = \bar{b},$$

$b_0$  represents the projections obtained from the initial image,  $\bar{b}$  is the difference between the measured projections and the projections from the initial image, and  $\bar{x}$  is the difference in the image space based on the information from the actual measurements and the initial image. The initial residual in the projection space is

$$\begin{aligned} \bar{b} &= b - b_0 \\ &= b - A x_0 . \end{aligned} \quad (4.12)$$

Therefore, only  $\tilde{\mathbf{x}}$ , the difference in the image space, need to be solved for in the iterative reconstruction process.

$$\begin{aligned}\tilde{\mathbf{t}}(\mathbf{k}) &= \tilde{\mathbf{t}}(\mathbf{k}-1) + [\tilde{\mathbf{b}} - \mathbf{A} \tilde{\mathbf{x}}(\mathbf{k}-1)] \\ \tilde{\mathbf{x}}(\mathbf{k}) &= \mathbf{A}^T \tilde{\mathbf{t}}(\mathbf{k})\end{aligned}\tag{4.13}$$

and

$$\mathbf{x}(\mathbf{k}) = \mathbf{x}_0 + \tilde{\mathbf{x}}(\mathbf{k})$$

This algorithm minimizes  $\|\tilde{\mathbf{x}}(\cdot)\|_2$  where  $\tilde{\mathbf{x}}(\cdot) \triangleq \lim_{\mathbf{k} \rightarrow \infty} \tilde{\mathbf{x}}(\mathbf{k})$ , i.e., the Euclidean norm of the

differences between the solution and the initial image,

$$\|\mathbf{x} - \mathbf{x}_0\|_2\tag{4.14}$$

It may be noted that, it is not necessary for the initial image,  $\mathbf{x}_0$ , to be the minimum-norm solution of  $\mathbf{A} \mathbf{x}_0 = \mathbf{b}_0$ .

#### 4.2.2 Convergence of PIRT under Constraints

Constraints are very often used in conjunction with the SIRT and other iterative image reconstruction algorithms. Although a variety of constraints can be applied, only those applied to the values of solutions are discussed in this section. The effects of the constraints on the support regions of solutions are considered in Section 4.2.4. The constraints applied to the values of a solution confine the solution within a boundary that is usually based on an appropriate physical reasoning. Such constraints can include non-negative values or bounds for the pixel gray levels. Constraints imposed in conjunction

with SIRT employed for solving an underdetermined system may not always lead to a unique solution.

When constraints are applied in conjunction with the PIRT for solving an underdetermined system, the solution does not get affected if the unconstrained solution is within the solution boundary. If the unconstrained minimum-norm solution is outside of the boundary, the solution converges to a minimum-norm solution in a reduced solution space provided that the minima exists within the reduced space and the constrained space is convex. In this case, the solution  $\mathbf{x}$  can be expressed as  $[\mathbf{x}_v^T \mid \mathbf{x}_c^T]^T$ , where  $\mathbf{x}_v$  is an  $N_v \times 1$  vector,  $\mathbf{x}_c$  is an  $N_c \times 1$  vector and  $N_v + N_c = N$ .  $\mathbf{x}_c$  is a vector of constant values which corresponds to the part of the solution which is constrained by the boundary.  $\mathbf{x}_v$  denotes the rest of variables to be solved. The problem is equivalent to solving a system with reduced dimensions

$$[\mathbf{A}_v \mid \mathbf{A}_c] \begin{bmatrix} \mathbf{x}_v \\ - \\ \mathbf{x}_c \end{bmatrix} = \mathbf{b} \quad (4.15)$$

$$\mathbf{A}_v \mathbf{x}_v = \mathbf{b} - \mathbf{A}_c \mathbf{x}_c = \mathbf{c}$$

$$\text{where } [\mathbf{A}_v \mid \mathbf{A}_c] = \mathbf{A}$$

$$\text{and } \mathbf{c} = \mathbf{b} - \mathbf{A}_c \mathbf{x}_c .$$

The dimension of the reduced system,  $\mathbf{A}_v \mathbf{x}_v = \mathbf{c}$ , is  $M \times N_v$  where  $N_v < N$ . The solution converges to the unique minimum-norm solution in the reduced space provided that the system is still underdetermined.

When more and more pixels are constrained to take constant values, the dimensions of the solution space may become smaller than the dimension of the measurements in the projection space. In this case, the originally underdetermined system is turned into an overdetermined system subject to the constraints. It is also possible that, after some pixels are constrained to take constant values, the number of linearly independent columns in the matrix  $A$  is less than  $M$  despite the fact that more than  $M$  pixels need to be solved for. In the latter case, the system become an undetermined system. In both of the above cases, the matrix  $[A, A_v^T]$  is not positive definite. The convergence properties of the PIRT is discussed in Section 4.2.3.

#### 4.2.3 Conditions of Convergence of PIRT

The state vector  $t$  in the projection space of the PIRT expressed by eq. 4.10 is only guaranteed to converge to a unique solution when the system is underdetermined or when the matrix  $A$  is square and full rank. The residual in the projection space will converge to zeros only when the rank of  $A$  is  $M$ . When the rank of  $A$  is less than  $M$ , the state variable,  $t$ , in the projection space will diverge as shown below.

Consider an overdetermined system, where the measured vector  $b$  can be decomposed into two orthogonal components

let  $\mathbf{b}_\perp \in \mathfrak{R}^M$  with

$$\mathbf{b}_\perp \in \text{null space of } \mathbf{A}^T$$

and

$$\mathbf{b}_\parallel \in \mathfrak{R}^M \text{ with}$$

$$\mathbf{b}_\parallel \in \text{range of } \mathbf{A}$$

(4.16)

then

$$\begin{aligned} \mathbf{b} &= \bar{a}_1 x_1 + \bar{a}_2 x_2 + \dots + \bar{a}_N x_N + \mathbf{b}_\perp \\ &= \mathbf{b}_\parallel + \mathbf{b}_\perp \end{aligned}$$

for  $\mathbf{b}_\parallel \perp \mathbf{b}_\perp$

where  $M > N$ , and  $\bar{a}_j$  is the  $j^{\text{th}}$  linearly independent column of  $\mathbf{A}$ . Under these conditions, the linear system can be decomposed into two independent systems

$$\mathbf{t}_\parallel(k) = \mathbf{t}_\parallel(k-1) + [\mathbf{b}_\parallel - \mathbf{A} \mathbf{A}^T \mathbf{t}_\parallel(k-1)]$$

and

$$\mathbf{t}_\perp(k) = \mathbf{t}_\perp(k-1) + [\mathbf{b}_\perp - \mathbf{A} \mathbf{A}^T \mathbf{t}_\perp(k-1)] \quad (4.17)$$

where

$$\mathbf{t}_\parallel(k) \in \text{range of } \mathbf{A}$$

$$\mathbf{t}_\perp(k) \in \text{null space of } \mathbf{A}^T$$

$$\text{for } \mathbf{t}_\parallel(0) = \mathbf{t}_\perp(0) = \mathbf{0}$$

Consider a measurement  $\mathbf{b}_\perp$  in the null space of  $\mathbf{A}^T$ ,  $\mathbf{b}_\perp \neq \mathbf{0}$  and  $\mathbf{A}^T \mathbf{b}_\perp = \mathbf{0}$ . The vector  $\mathbf{t}_\perp$  therefore linearly increases in proportion to the iteration number  $k$ :

since  $A^T t_{\perp}(k-1) \equiv 0$

$$\begin{aligned}
 t_{\perp}(k) &= t_{\perp}(k-1) + [b_{\perp} - A A^T t_{\perp}(k-1)] \\
 &= t_{\perp}(k-1) + b_{\perp} \\
 &= t_{\perp}(k-2) + 2 b_{\perp} \\
 &\dots\dots\dots \\
 &= k b_{\perp}, \quad \text{for } t_{\perp}(0) = 0
 \end{aligned} \tag{4.18}$$

and

$$\lim_{k \rightarrow \infty} \| t_{\perp}(k) \|_2 = \infty$$

This indicates that the state vector  $t$  has a tendency to diverge linearly as a function of the iteration number.

$$\lim_{k \rightarrow \infty} t(k) = \lim_{k \rightarrow \infty} [t_{\parallel}(k) + t_{\perp}(k)] = \infty . \tag{4.19}$$

When the system is overdetermined, the solution obtained using PIRT in the image space converges to the least squares solution despite divergence in the projection space.

Let  $x(\cdot)$  denote the final converged solution and  $x(\cdot)_j$ ,  $j = 1, 2, \dots, N$ , be the  $j^{\text{th}}$  element of  $x(\cdot)$ , then

$$\mathbf{b}_1 = \bar{\mathbf{a}}_1 x_1 + \bar{\mathbf{a}}_2 x_2 + \dots + \bar{\mathbf{a}}_N x_N$$

$$\mathbf{A} \mathbf{x}(\cdot) = \bar{\mathbf{a}}_1 x(\cdot)_1 + \bar{\mathbf{a}}_2 x(\cdot)_2 + \dots + \bar{\mathbf{a}}_N x(\cdot)_N$$

$$\text{since } \mathbf{b}_1 - \mathbf{A} \mathbf{x}(\cdot) = \mathbf{0}$$

$$\text{hence} \tag{4.20}$$

$$\bar{\mathbf{a}}_1 [x_1 - x(\cdot)_1] + \bar{\mathbf{a}}_2 [x_2 - x(\cdot)_2] + \dots + \bar{\mathbf{a}}_N [x_N - x(\cdot)_N] = \mathbf{0}$$

and all  $\bar{\mathbf{a}}_j$ 's are linearly independent

therefore,  $x_j - x(\cdot)_j = 0$ , for all  $j = 1$  to  $N$ .

Then the residual is

$$\mathbf{b}_\perp = \mathbf{b} - \mathbf{A} \mathbf{x}(\cdot) \tag{4.21}$$

The solution is equivalent to the one obtained by minimizing  $\|\mathbf{b} - \mathbf{A} \mathbf{x}(\cdot)\|_2$ .

#### 4.2.4 Geometric Considerations

It has been shown in Section 4.2.3 that, for the convergence of PIRT in the projection space, the system has to be underdetermined or determined. In this section, an important restriction on the projection geometry of the PIRT is introduced. It should be kept in mind that whenever the PIRT is used, none of the projections should cover the entire support region of the solution in the image space.

In the case where  $M \leq N$  for an  $M \times N$  matrix  $\mathbf{A}$ , a set of projections should be chosen so that all columns of the matrix  $\mathbf{A}$  are linearly independent in order to avoid having an indeterminate system. It can be shown that, if any two projections cover the entire

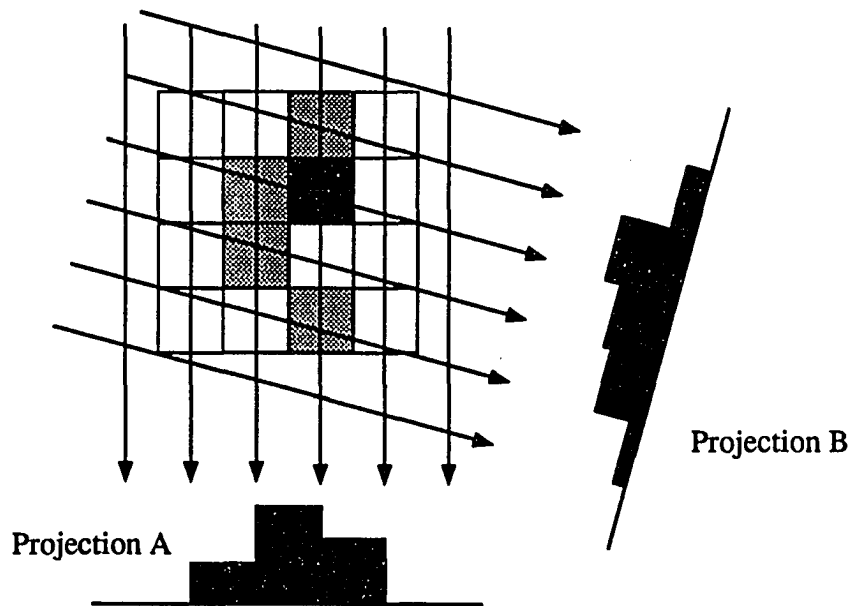


Fig. 4.3. Projection A and B cover the entire region of solution  $x$ .

support region of the solution  $x$  on the image plane as shown in Fig. 4.3, then the columns of  $A$  will become linearly dependent. The system then becomes indeterminate.

For an  $M \times N$  matrix  $A$ ,  $M \leq N$ , if a row of  $A$  can be expressed as a linear combination of other rows of  $A$ , i.e.

for any  $\alpha_i \in \mathfrak{R}$

$$\hat{a}_p^T = \sum_{i \neq p} \alpha_i \hat{a}_i^T \quad (4.22)$$

where  $\hat{a}_i^T$  is the  $i^{\text{th}}$  row of  $A$ ,  $i, p \in \{1, 2, \dots, N\}$

then the system is undeterminate.

If we assume that there are projections at angle  $\Theta_p$  and  $\Theta_q$  which cover the entire support region of the variable vector  $\mathbf{x}$  on the image plane, then both projections have the same total mass, i.e.

$$\sum_{i_p \in S_p} \hat{\mathbf{a}}_{i_p}^T \cdot \mathbf{x} = \sum_{i \in S_q} \hat{\mathbf{a}}_{i_q} \cdot \mathbf{x} = \sum_{j=1}^N \mathbf{x} \quad (4.23)$$

where  $S_p$  and  $S_q$  denote sets of indices of ray-sums corresponding to the projections at  $\Theta_p$  and  $\Theta_q$  respectively. Then

$$\hat{\mathbf{a}}_p^T \cdot \mathbf{x} = \left[ \sum_{i_j \in S_q} \hat{\mathbf{a}}_{i_q}^T - \sum_{\substack{i_p \neq p \\ i_p \in S_p}} \hat{\mathbf{a}}_{i_p}^T \right] \cdot \mathbf{x} \quad (4.24)$$

and

$$\hat{\mathbf{a}}_p^T = \sum_{\substack{i \neq p \\ i \in S_p \cup S_q}} \hat{\mathbf{a}}_i^T$$

Therefore, the system is indeterminate since  $\hat{\mathbf{a}}_p^T$  is a linear combination of the other rows of  $\mathbf{A}$ .

If the solution  $\mathbf{x}$  is constrained to be strictly in the convex support region on the image plane, defined by the support regions of projections as shown in Fig. 4.4, then the system becomes undetermined. This is a consequence of the fact that every projection covers the entire support region of the solution  $\mathbf{x}$ . In this case, constraints on the support region of solutions need to be somehow relaxed in order to prevent divergence of the state vector,  $\mathbf{t}$ .

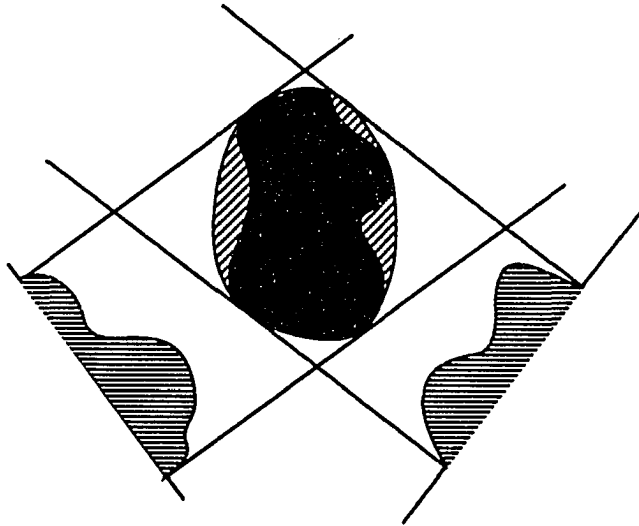


Fig. 4.4. A convex support region constrained by support regions of projections.

### 4.3 Conjugate Gradient Method for PIRT

An introductory review of the conjugate gradient method is given in Section 4.3.1. Section 4.3.2 presents a method utilizing this technique for tomographic image reconstruction for underdetermined systems.

#### 4.3.1 Conjugate Gradient Method

The conjugate gradient method has been extensively used as an acceleration technique for solving linear systems. Unlike other iterative methods which may involve an infinite number of iterations, the conjugate gradient method, computes the exact solution in a finite number of iterations. However, the convergence is guaranteed only when the system is symmetric and positive definite.

Consider the problem where we wish to minimize a quadratic function

$$F(\mathbf{x}) = \frac{1}{2} \mathbf{x}^T \mathbf{A} \mathbf{x} - \mathbf{b}^T \mathbf{x} \quad (4.25)$$

The gradient of  $F(\mathbf{x})$  is

$$\begin{aligned} \mathbf{r}(\mathbf{x}) &= \frac{\partial F(\mathbf{x})}{\partial \mathbf{x}} \\ &= \mathbf{A} \mathbf{x} - \mathbf{b} \end{aligned} \quad (4.26)$$

where,  $\mathbf{r}(\mathbf{x})$  is also the residual of  $\mathbf{A} \mathbf{x} - \mathbf{b}$ . When  $\mathbf{r}(\mathbf{x})$  is zero, then the corresponding  $\mathbf{x}$  is the solution of the linear system  $\mathbf{A} \mathbf{x} = \mathbf{b}$ .

The conjugate gradient method of solving the equation  $\mathbf{A} \mathbf{x} = \mathbf{b}$  involves the use of following iterative procedure

$$\mathbf{p}_k \leftarrow \mathbf{A} \mathbf{d}_k \quad (4.27)$$

$$\alpha_k = \frac{\mathbf{d}_k^T \mathbf{r}_k}{\mathbf{p}_k^T \mathbf{d}_k} \quad \text{or} \quad \frac{\mathbf{r}_k^T \mathbf{r}_k}{\mathbf{d}_k^T \mathbf{p}_k} \quad (4.28)$$

$$\mathbf{x}_{k+1} \leftarrow \mathbf{x}_k + \alpha_k \mathbf{d}_k \quad (4.29)$$

$$\mathbf{r}_{k+1} \leftarrow \mathbf{r}_k - \alpha_k \mathbf{p}_k \quad (4.30)$$

$$\beta_k = \frac{-\mathbf{p}_k^T \mathbf{r}_{k+1}}{\mathbf{p}_k^T \mathbf{d}_k} \quad \text{or} \quad \frac{\mathbf{r}_{k+1}^T \mathbf{r}_{k+1}}{\mathbf{r}_k^T \mathbf{r}_k} \quad (4.31)$$

$$\mathbf{d}_{k+1} \leftarrow \mathbf{r}_{k+1} + \beta_k \mathbf{d}_k \quad (4.32)$$

The initial values can be chosen as  $x_0 = 0$ ,  $d_0 = b$  and  $r_0 = b$ . In the iterative procedure,  $p_k$  and  $\alpha_k$  are the descent direction and descent step respectively,  $d_k$  and  $\beta_k$  represent the search direction and the search step.

In the iterative procedure described by eqs. 4.27 to 4.32, the search direction  $d_k$  is conjugate to all the previous search directions, i.e.

$$d_{k+1}^T A d_i = 0, \quad i = 0, \dots, k \quad (4.33)$$

This is accomplished by choosing the search direction step size  $\beta_k$  such that

$$d_{k+1}^T A d_k = 0, \quad \text{for all } k. \quad (4.34)$$

Eq. 4.31 is derived by substituting eqs. 4.32, 4.31, 4.30, 4.28 and 4.27 into eq. 4.34.  $\alpha_k$  represents the optimum step size in the linear search. The update equation, eq. 4.28, is derived from

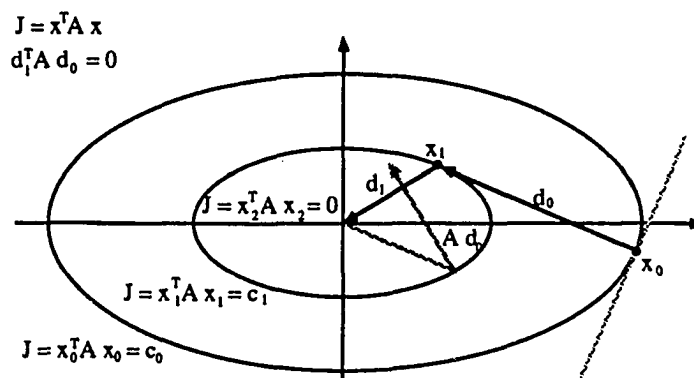


Fig. 4.5. The conjugate gradient method converges in N steps.

$$\frac{\partial F(\mathbf{x}_{k+1})}{\partial \alpha_k} = 0 \quad (4.35)$$

where the function,  $F(\mathbf{x})$ , is defined in eq. 4.25.

Since, all the search directions are conjugate to all previous search directions, the minimization along a given direction implies a minimization along all previous search directions also. Hence, for an  $N$  dimension problem, only  $N$  steps are needed to arrive at the solution provided there is no numerical error. If the system has  $M$  distinct eigenvalues, the conjugate gradient method converges in  $M$  steps rather than  $N$  steps. Examples of a two dimensional case are given in Fig. 4.5 and 4.6. In the example, the conjugate gradient method arrives at the solution in at most two steps whereas the steepest descend method requires an infinite number of steps.

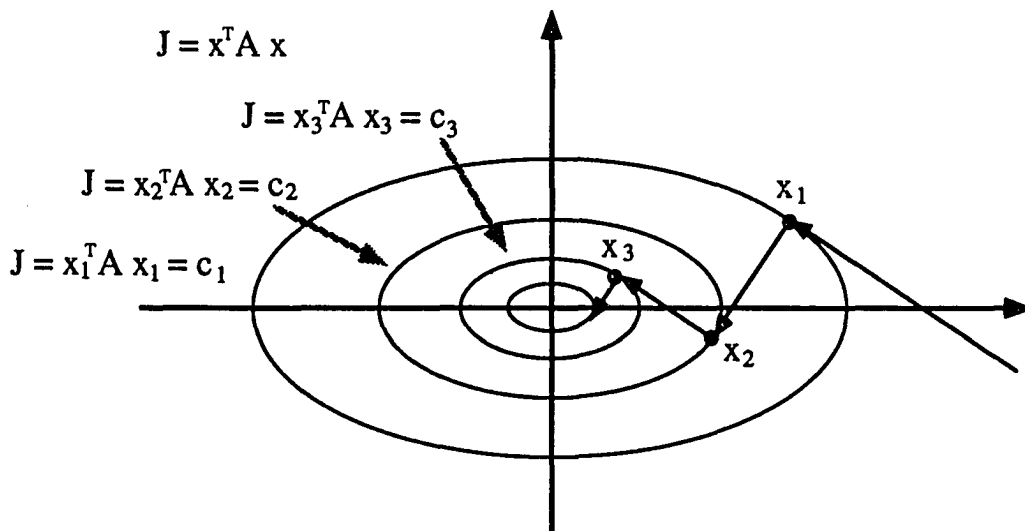


Fig. 4.6. The steepest descend method converges in an infinite number of steps.

### 4.3.2 SIRT-CG and PIRT-CG Algorithms

In order to guarantee the convergence of the conjugate gradient method, the matrix  $A$  has to be symmetric and positive definite. Otherwise, the relations given by eqs. 4.26, 4.33, 4.34 and 4.35 may not be valid.

When a system is overdetermined, the matrix  $[A A^T]$  in eq. 3.6 is symmetric and positive definite. Hence, the convergence of the conjugate gradient method is guaranteed. In this case, the descent direction  $p_k$  in eq. 4.27 is updated by

$$p_k \leftarrow A^T A d_k \quad (4.36)$$

Then the iterative procedure is

$$\begin{aligned} p_k &\leftarrow A^T A d_k \\ \alpha_k &= \frac{d_k^T r_k}{p_k^T d_k} \quad \text{or} \quad \frac{r_k^T r_k}{d_k^T p_k} \\ x_{k+1} &\leftarrow x_k + \alpha_k d_k \\ r_{k+1} &\leftarrow r_k - \alpha_k p_k \\ \beta_k &= \frac{-p_k^T r_{k+1}}{p_k^T d_k} \quad \text{or} \quad \frac{r_{k+1}^T r_{k+1}}{r_k^T r_k} \\ d_{k+1} &\leftarrow r_{k+1} + \beta_k d_k \end{aligned} \quad (4.37)$$

The corresponding initial values can be chosen as  $x_0 = \mathbf{0}$  and  $d_0 = r_0 = A^T b$ . Eq. 4.37 is the commonly used SIRT-CG type algorithm in image reconstruction.

When a system is underdetermined, the matrix  $[A A^T]$  in eq. 4.1 is symmetric and positive definite. The convergence of the conjugate gradient method is, once again,

guaranteed. In this case, eq. 4.27 is replaced by

$$p_k \leftarrow A A^T d_k \quad (4.38)$$

The state vector can be solved using the following procedure

$$\begin{aligned} p_k &\leftarrow A A^T d_k \\ \alpha_k &= \frac{d_k^T r_k}{p_k^T d_k} \quad \text{or} \quad \frac{r_k^T r_k}{d_k^T p_k} \\ t_{k+1} &\leftarrow t_k + \alpha_k d_k \\ r_{k+1} &\leftarrow r_k - \alpha_k p_k \\ \beta_k &= \frac{-p_k^T r_{k+1}}{p_k^T d_k} \quad \text{or} \quad \frac{r_{k+1}^T r_{k+1}}{r_k^T r_k} \\ d_{k+1} &\leftarrow r_{k+1} + \beta_k d_k \end{aligned} \quad (4.39)$$

where the corresponding initial values can be chosen as  $t_0 = \mathbf{0}$ ,  $d_0 = \mathbf{b}$  and  $r_0 = \mathbf{b}$  and the final solution is  $\mathbf{x} = A^T t$ . Eq. 4.39 represents the PIRT-CG algorithm for tomographic image reconstruction. It can also be solved without building up the state vector

$$\begin{aligned} p_k &\leftarrow A A^T d_k \\ \alpha_k &= \frac{d_k^T r_k}{p_k^T d_k} \quad \text{or} \quad \frac{r_k^T r_k}{d_k^T p_k} \\ x_{k+1} &\leftarrow x_k + \alpha_k A^T d_k \\ r_{k+1} &\leftarrow r_k - \alpha_k p_k \\ \beta_k &= \frac{-p_k^T r_{k+1}}{p_k^T d_k} \quad \text{or} \quad \frac{r_{k+1}^T r_{k+1}}{r_k^T r_k} \\ d_{k+1} &\leftarrow r_{k+1} + \beta_k d_k \end{aligned} \quad (4.40)$$

where the corresponding initial values can be chosen as  $\mathbf{x}_0 = \mathbf{0}$ ,  $\mathbf{d}_0 = \mathbf{b}$  and  $\mathbf{r}_0 = \mathbf{b}$ . The iterative procedure expressed in eq. 4.40 is similar to the algorithm used for solving unsymmetric systems [77-78].

For large and sparse systems, it is difficult to obtain the matrix-matrix product  $[\mathbf{A}^T \mathbf{A}]$  or  $[\mathbf{A} \mathbf{A}^T]$ . In this case, the conjugate gradient method can be used directly on the matrices  $\mathbf{A}$  and  $\mathbf{A}^T$  sequentially using matrix-vector-multiplications as shown in eq. 4.37 and eq. 4.37.

In the case of tomographic image reconstruction, the SIRT-CG algorithm was developed as an alternative to SIRT in order to improve convergence for both overdetermined and underdetermined systems.

When a system is overdetermined, the matrix  $[\mathbf{A}^T \mathbf{A}]$  is symmetric and positive definite. Hence, the conjugate gradient method can be applied in conjunction with the SIRT type algorithm with guaranteed convergence. Unfortunately, when the system is underdetermined, the matrix  $[\mathbf{A}^T \mathbf{A}]$  associated with the SIRT is not positive definite anymore. Hence, the acceleration technique does not lead to convergence if any errors are accumulated during the iterative process. However, with the PIRT type algorithm, the state space matrix  $[\mathbf{A} \mathbf{A}^T]$  is symmetric and positive definite when the system is underdetermined. Consequently, the PIRT-CG methods can be applied for solving underdetermined systems. Convergence of such algorithms is then guaranteed even if explicit constraints are not applied.

Since the residual in the algorithm expressed in eqs. 4.37, 4.39 or 4.40 is calculated recursively instead of obtaining from the current state  $\mathbf{t}(\mathbf{k})$  (or  $\mathbf{x}(\mathbf{k})$ ) and the original input  $\mathbf{b}$ , decoupling between the system and the original input can be caused by numerical errors or noise associated with optoelectronic devices. In order to avoid the decoupling, the residual  $\mathbf{r}_{k+1}$  can be updated using the true residual,  $[\mathbf{b} - \mathbf{A} \mathbf{x}_{k+1}]$ , instead of using the recursive approach. The PIRT-CG algorithm can be rewritten as follows

$$\begin{aligned}
 \mathbf{p}_k &\leftarrow [\mathbf{A} \ \mathbf{A}^T] \mathbf{d}_k \\
 \alpha_k &= \mathbf{r}_k^T \mathbf{r}_k / \mathbf{d}_k^T \mathbf{p}_k \\
 \mathbf{t}_{k+1} &\leftarrow \mathbf{t}_k + \alpha_k \mathbf{d}_k \\
 \mathbf{x}_{k+1} &\leftarrow \mathbf{A}^T \mathbf{t}_{k+1} \\
 \mathbf{r}_{k+1} &\leftarrow \mathbf{b} - \mathbf{A} \mathbf{x}_{k+1} \\
 \beta_k &= \mathbf{r}_{k+1}^T \mathbf{r}_{k+1} / \mathbf{r}_k^T \mathbf{r}_k \\
 \mathbf{d}_{k+1} &\leftarrow \mathbf{r}_{k+1} + \beta_k \mathbf{d}_k
 \end{aligned} \tag{4.41}$$

where  $\mathbf{t}_0 = \mathbf{0}$ ,  $\mathbf{d}_0 = \mathbf{b}$  and  $\mathbf{r}_0 = \mathbf{b}$ .

The matrix-vector-multiplications associated with the PIRT-CG can be performed using optical projections. This allows implementation of the algorithm using a high speed optoelectronic structure. Implementation details are presented in the next section.

#### 4.4 Optoelectronic Implementation

The algorithm of eq. 4.10 can also be expressed in terms of projections from different angles:

**repeat**

$$\mathbf{x}_{old} \leftarrow \mathbf{x}_{new}$$

$$\mathbf{x}_{new} \leftarrow \mathbf{0}$$

**for**  $q = 1$  **to**  $np$  **do**

$$\mathbf{t}_q \leftarrow \mathbf{t}_q + \alpha [\hat{\mathbf{b}}_q - \mathbf{A}_q \mathbf{x}_{old}]$$

$$\mathbf{x}_{new} \leftarrow \mathbf{x}_{new} + \beta \mathbf{A}_q^T \mathbf{t}_q$$

**end of for**

**until done**

(4.42)

where  $\mathbf{t}_q$ ,  $\mathbf{A}_q^T$ ,  $\hat{\mathbf{b}}_q$  and  $\mathbf{A}_q$  are submatrices or subvectors of  $\mathbf{t}$ ,  $\mathbf{A}^T$ ,  $\mathbf{b}$  and  $\mathbf{A}$  respectively corresponding to the  $q^{\text{th}}$  angle. The total number of projections from all measured angles is represented by  $np$ .

The proposed optoelectronic system for implementing PIRT underdetermined system is shown in Fig. 4.7. The structure is similar to that for the SIRT shown in Fig. 3.6. The implementation of the forward and back projection operations are explained in section 3.3. The complexity of operations is about the same as SIRT but extra storage is needed for the state vector  $\mathbf{t}$  in the projection space. In addition, the iterations are not carried out in the

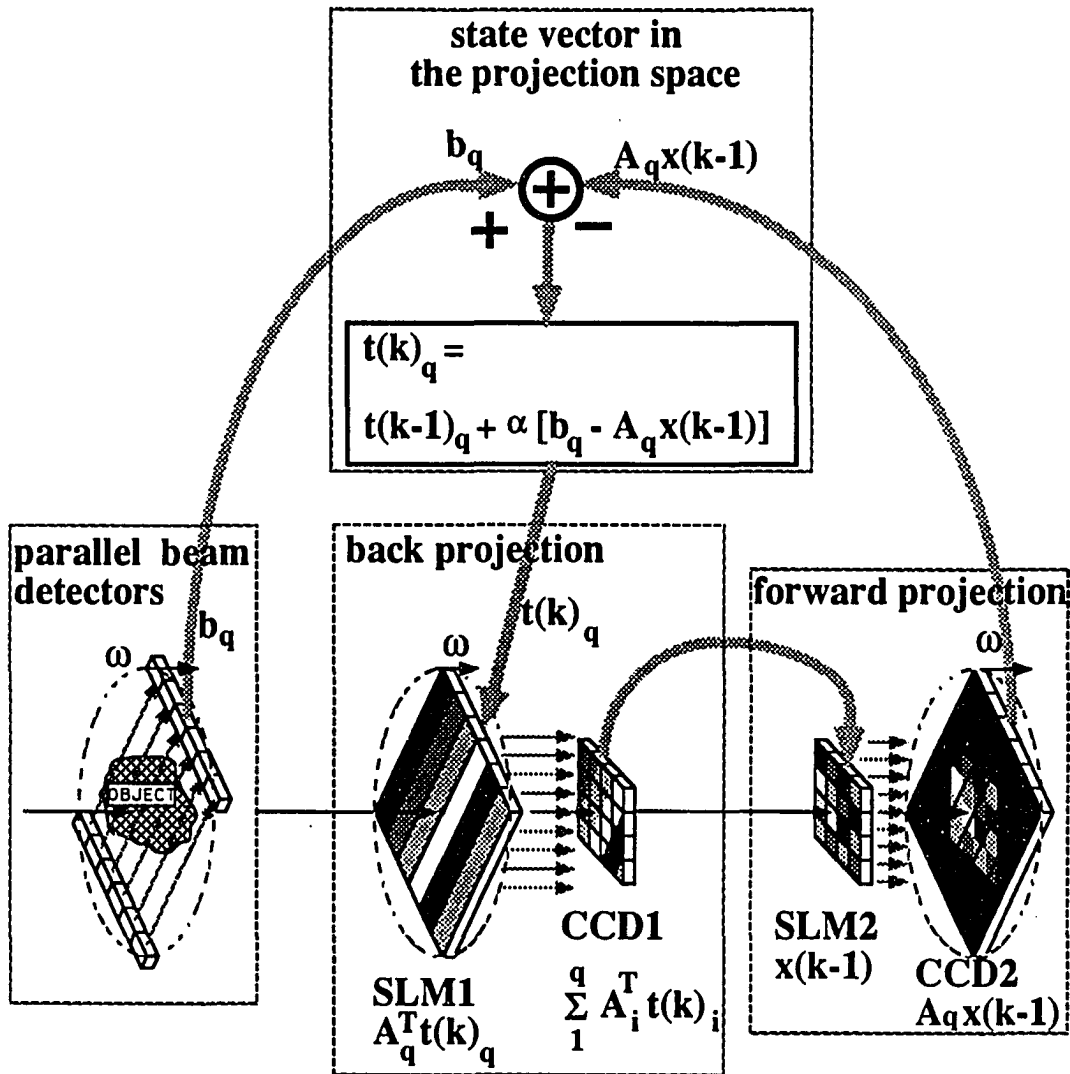


Fig. 4.7. An optoelectronic structure for the PIRT.

image space. Instead, a new image is reconstructed using only the updated state vector in the projection space.

The iterative procedure which can be implemented using the structure shown in Fig. 4.7 can be described as follows:

**procedure****constant**

$\mathbf{b}_q$ :  $q = 1$  to  $np$ , measured projection at the  $q^{\text{th}}$  angle;

**variable**

$\mathbf{t}_q$ :  $q = 1$  to  $np$ , state vector at the  $q^{\text{th}}$  angle;

$\mathbf{x}_{\text{new}}$ : in CCD1, reconstructed image;

$\mathbf{x}_{\text{old}}$ : in SLM2, reconstructed image from the previous iteration;

1. Update  $\mathbf{x}_{\text{old}}$  in SLM2 with  $\mathbf{x}_{\text{new}}$  in CCD1;  
reset  $\mathbf{x}_{\text{new}}$  in CCD1 to 0;
2. **for**  $q=1$  to  $np$  **do**
3.     Rotate to  $\Theta_q$ ;
4.     Forward project  $\mathbf{x}_{\text{old}}$ , the reconstructed image from the 2-D array SLM2 into the 1-D array CCD2, thereby generating  $[\mathbf{A}_q \mathbf{x}_{\text{old}}]$ .
5.     Update  $\mathbf{t}_q$  by  $\{\mathbf{t}_q + [\mathbf{b}_q - \mathbf{A}_q \mathbf{x}_{\text{old}}]\}$ ;  
   load  $\mathbf{t}_q$  into the 1-D array SLM1;
6.     Back project the state vector in the 1-D SLM1 into the 2-D CCD1. The result in CCD1 is a superimposed set of back projections:

$$\sum_{i=1}^q \mathbf{A}_i^T \mathbf{t}_i$$

7.     **end of for**
8.     **end of the iteration.**

The conjugate gradient method can also be implemented using the structure shown in Fig. 4.7. In the accelerated algorithm described by eq. 4.41, there are two matrix-vector-multiplications associated with the matrix  $[A A^T]$ . Using the optoelectronic structure, these matrix-vector-multiplications are performed by passing the vectors  $\mathbf{d}$  and  $\mathbf{t}$  through the back projection and the forward projection operators separately. The reconstructed image is obtained without additional cost since the output vector  $\mathbf{x}$  represents the intermediate result obtained after back projecting  $\mathbf{t}$ . The rest of the calculations in the algorithm are simple vector-vector or scalar operations and therefore, do not require any special structures.

## 4.5 Simulation of PIRT

The simulation results presented in this section are in agreement with the analytical properties with respect to PIRT. The performance of the PIRT has been verified in respect of convergence properties both for the basic as well as the modified version employing the conjugate gradient algorithm. The test phantom and methods used for simulating have been explained in Section 3.5.

### 4.5.1 Simulation of Basic PIRT

Fig. 4.8 shows the reconstructed image obtained using the basic PIRT while Fig. 4.10 presents plots of Euclidian norms of the image and the residual as a function of the number of iterations. The residual is the distance between the reconstructed image and the original image. The reconstructed images are  $128 \times 128$  and consequently  $N = 16,384$ . The

number of projections are 120 and there are 121 ray-sums in each projection. Therefore,  $M = 14,520$ . The ratio of  $M$  to  $N$  for the underdetermined system is 0.886. In order to study the convergence characteristics, constraints have not been imposed.

#### 4.5.2 Simulation of PIRT-CG

Fig. 4.9 and Fig. 4.10 show results obtained using the conjugate gradient method. Fig. 4.9 shows the reconstructed image while Fig. 4.10 gives the plots of the Euclidian norms of the solution and the residual as a function of the number of iterations. The corresponding values of the original images, the reconstructed images and the residuals obtained using the two methods are listed in Table 4.1. The images reconstructed using the basic PIRT are relatively smooth compared to those obtained using the conjugate gradient method. However, the residual of the conjugate gradient method at the 8<sup>th</sup> iteration (16.06363) is approximately the same as that obtained using the basic method at the 82<sup>th</sup> iteration (16.07527). The residual obtained using the basic PIRT at the 8<sup>th</sup> iteration is 34.65206.

**Table 4.1. Residuals of Reconstructed Images Using PIRT and PIRT-CG.**

iteration/ algorithm	0	1	2	4	8	16	32	64	82
PIRT	102.54	61.16	49.68	41.57	34.62	28.40	22.53	17.54	16.08
PIRT-CG	102.54	57.32	38.97	26.51	16.06	11.41	10.35	9.80	9.58

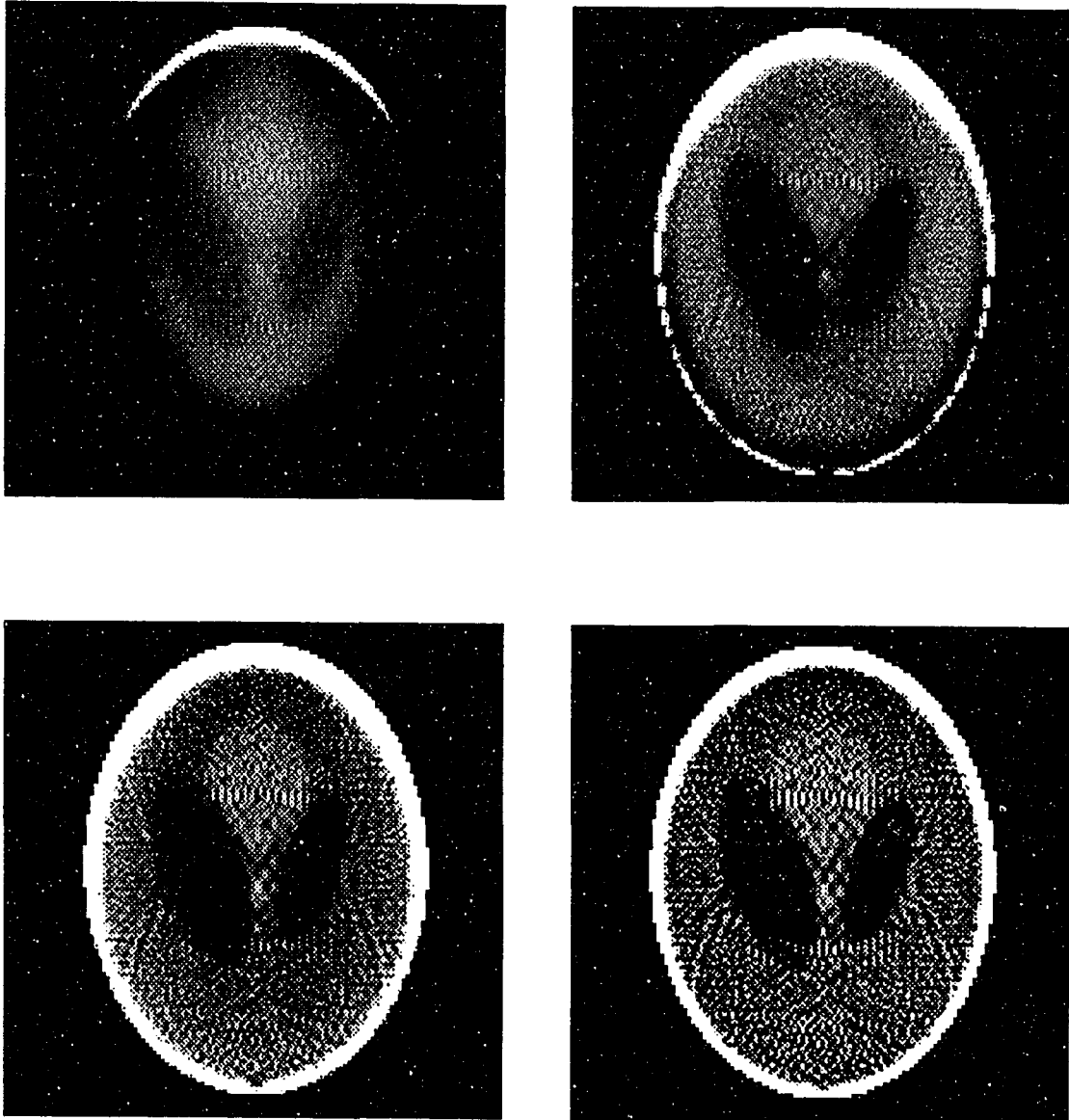


Fig. 4.8. Reconstructed images using PIRT at the 8<sup>th</sup>, 16<sup>th</sup>, 32<sup>nd</sup> and 64<sup>th</sup>.

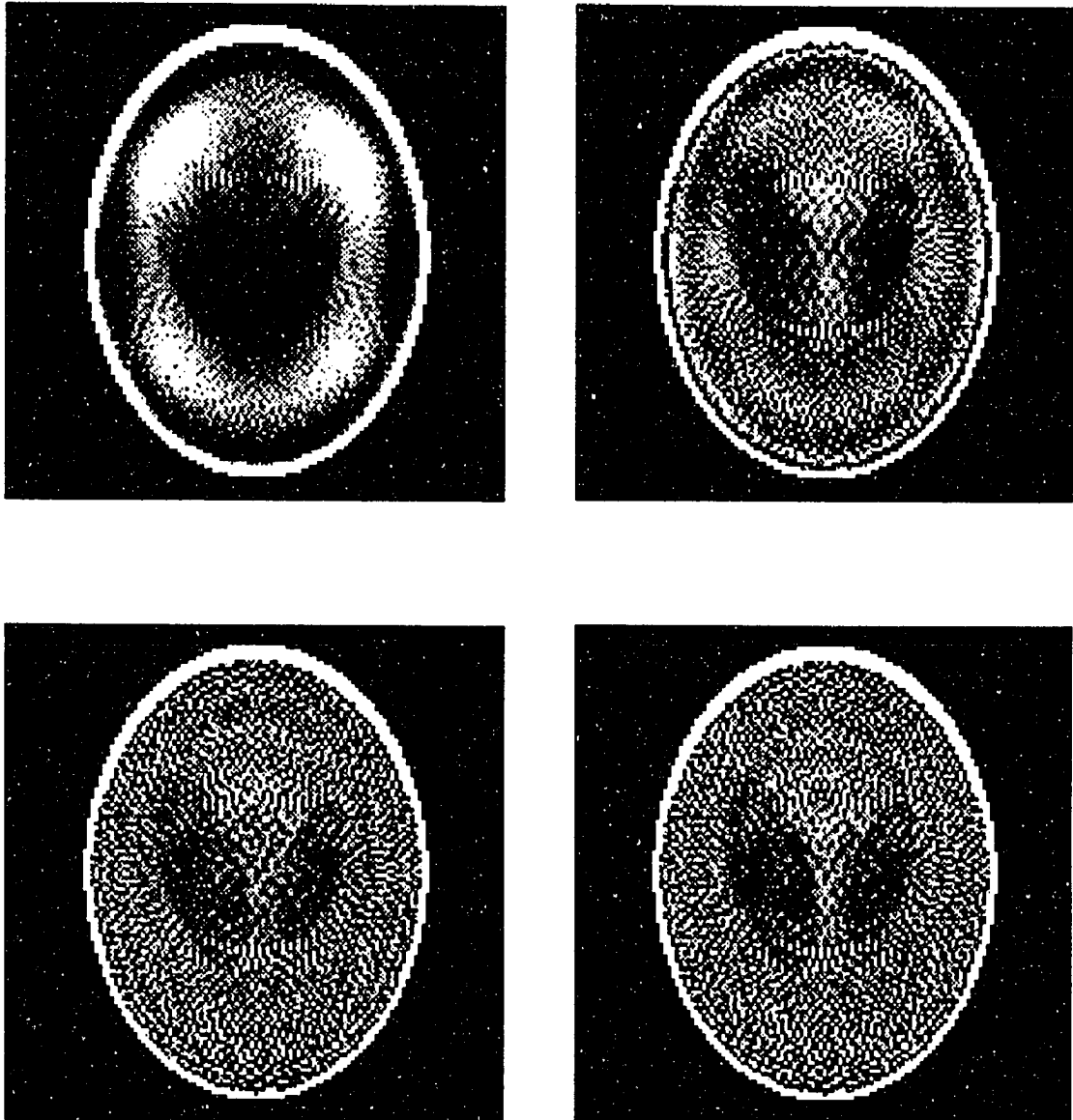


Fig. 4.9. Reconstructed images using the PIRT-CG at the 8<sup>th</sup>, 16<sup>th</sup>, 32<sup>nd</sup> and 64<sup>th</sup> iterations.

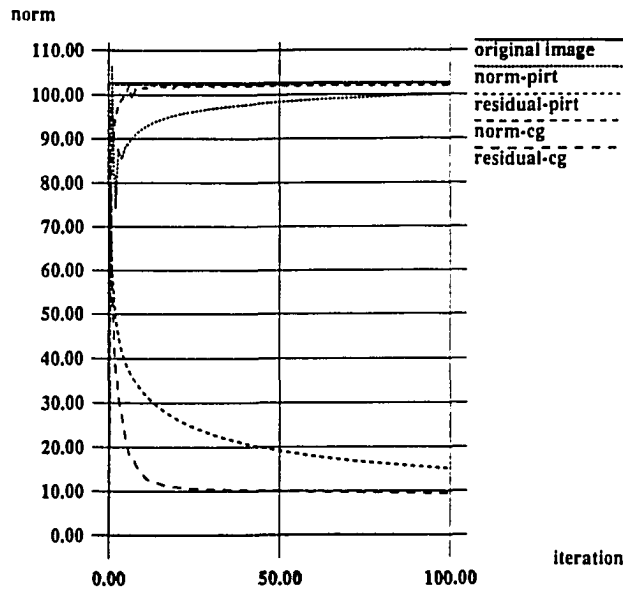


Fig. 4.10. A plot of residuals of reconstructed images vs. the original phantom using PIRT and CG-PIRT.

#### 4.5.3 Results Obtained using PIRT with Random Noise

In this simulation, the system is severely underdetermined. The dimensions of the reconstructed image are  $256 \times 256$ . The number of projections are 120 and there are 121 ray-sums in each projection. Therefore, the ratio of the  $M$  to  $N$  is 0.222 where  $M$  and  $N$  are dimensions of the matrix  $A$  in eq. 4.10. Uniformly distributed noise in the range of  $-0.5$  to  $+0.5$  is added to the reconstructed image after each iteration. The resulting SNR is 48.27 dB. Fig. 4.11 and Fig. 4.12 show clearly that the PIRT converges monotonously even with the additive noise. In contrast, the SIRT algorithm fails to converge as shown in Fig. 3.17.

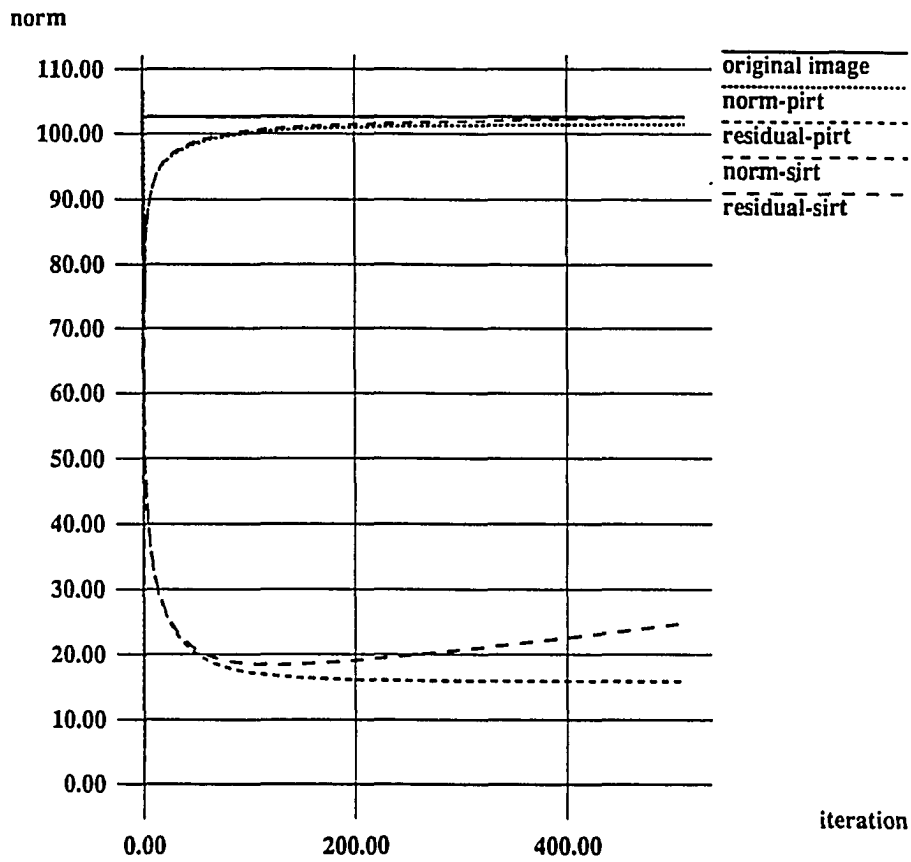


Fig. 4.11. A plot of residuals of reconstructed images with additive noise using PIRT and SIRT algorithms.

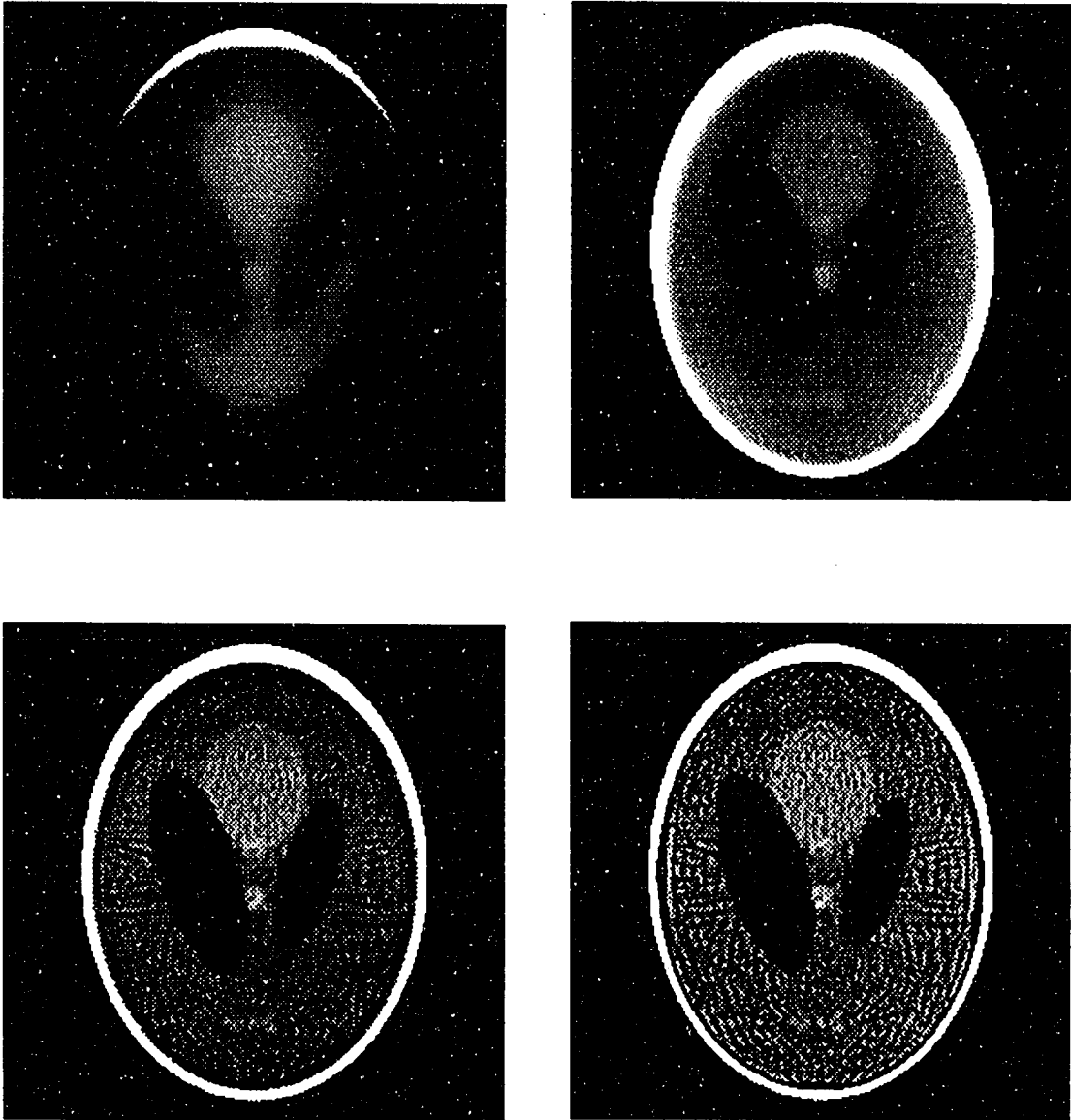


Fig. 4.12. Reconstructed images using PIRT with additive noise at the 16<sup>th</sup>, 32<sup>nd</sup>, 64<sup>th</sup> and 512<sup>th</sup> iterations.

#### 4.6 Summary

The tomographic image reconstruction algorithm - PIRT proposed in this Chapter is obviously superior to SIRT in respect of its convergence properties for underdetermined systems. This algorithm guarantees that the solution converges to the unique minimum-norm solution in the image space. With *a priori* information, this algorithm minimizes the Euclidian distance between the reconstructed image and the initial image in the image space. When constraints are applied and the minimum-norm solution is outside the constraint boundary, the solution converges to a unique minimum-norm solution in the reduced solution space. It also allows the application of acceleration techniques, such as conjugate gradient method, directly to the underdetermined system without the need for imposing explicit constraints.

Optoelectronic implementations of the PIRT similar to those for the SIRT shown in Chapter 3 are also presented. When the system is underdetermined, the PIRT guarantees convergence in contrast to the SIRT which fails to converge.

## **CHAPTER 5. ITERATIVE FILTERED BACK PROJECTION AND ITS OPTOELECTRONIC IMPLEMENTATION**

In this chapter, the Iterative Filtered Back Projection (IFBP) technique is presented. This algorithm [9] is based on the strategy of iteratively applying the Filtered Back Projection (FBP) method to approach the weighted minimum least square error in the frequency domain. In addition, a scheme for implementing the system using optoelectronic devices is given.

The Filtered Back Projection (FBP) is considered as a direct method for tomographic image reconstruction [10, 12]. The FBP and the corresponding convolution algorithms are commonly used in medical and industrial applications because of their lower computational demands. In some situations, reconstructed images can be distorted due to several factors, such as those introduced by aliasing from undersampling, finite filter bandwidth, limited views of projections, finite dynamic range of optoelectronic devices, and especially, speckle noise associated with optical transforms. The iterative approach introduced in this Chapter can be used to improve the quality of reconstructed images by applying error corrections repeatedly[9]. It will be shown that the errors introduced by the FBP procedures can be minimized in terms of the weighted mean square error in the frequency domain. Although FBP procedures can be considered as a method for estimating the inverse of the Radon transform, the accuracy is poor when the inverse is obtained using optical transforms.

However, optical transforms can be used to accelerate the iterative reconstruction procedure based on the method proposed in Chapter 3.

In Section 5.1, the IFBP method is presented after a brief review of the FBP. In Section 5.2, properties of the optical Fourier Transform are described first. An optoelectronic complementary filter structure is then introduced, where the bipolar radius filter of the FBP is implemented using a low pass optical complementary filter. In Section 5.3, the optoelectronic implementation of the IFBP is presented. Simulation results are given in Section 5.4. Section 5.5 presents a summary of the chapter.

## **5.1 Filtered Back Projection Method and Iterative Implementation**

In this section, the Fourier Slice Theory and the FBP tomographic image reconstruction method are reviewed first. The IFBP is then introduced followed by a discussion relating to the convergence properties in terms of least square errors in the frequency domain.

### **5.1.1 Filtered Back Projection Method**

#### **Fourier Slice Theorem**

The Fourier Slice Theorem can be stated as follows [10]: The Fourier transform of a parallel projection of an image  $f(x,y)$  taken at angle  $\theta$  is equal to the 1-D slice of the two-dimensional transform,  $F(u, v)$ , subtending an angle  $\theta$  with the  $u$ -axis. In other words, the Fourier transform of  $P(\theta, \rho)$  is identically equal to  $F(u, v)$  along the axis  $u'$  in Fig. 5.1-b.

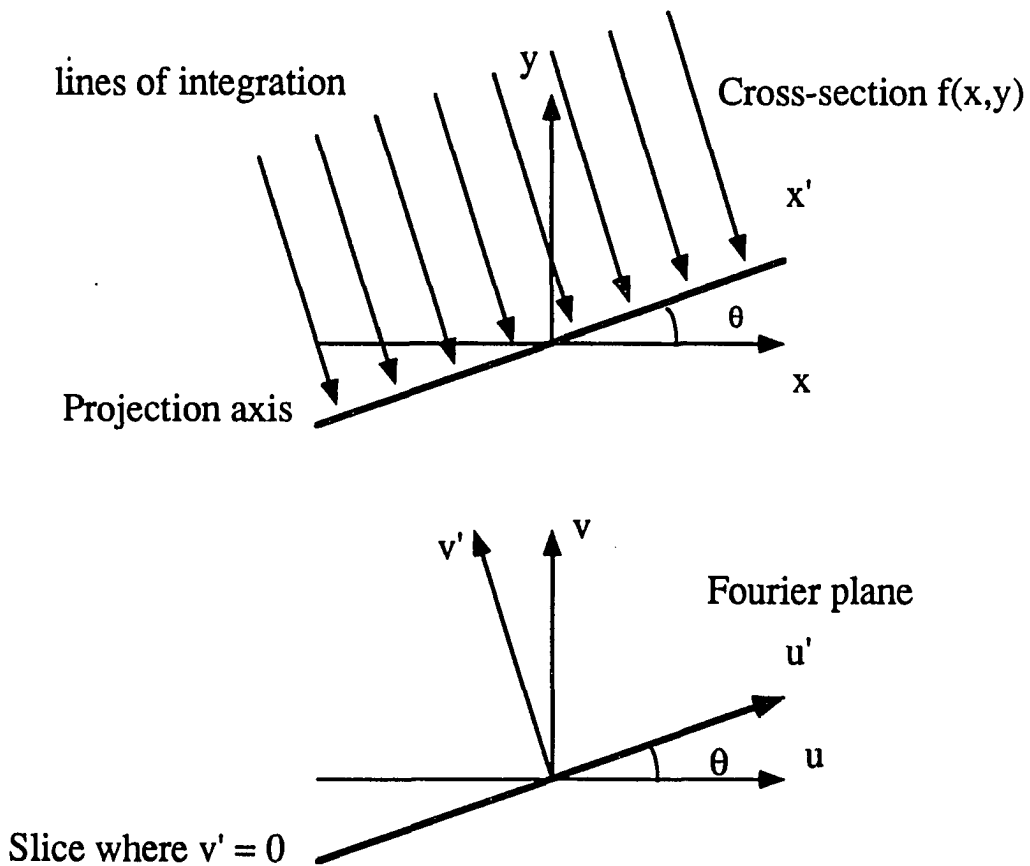


Fig.5.1. a) A projection taken from the  $x$ - $y$  plane at angle  $\theta$  perpendicular to the axis  $x'$ .  
 b) The Fourier representation of the projection in the  $u$ - $v$  plane is on the axis  $u'$  at a angle  $\theta$  to  $u$ .

In Fig. 5.1-a, a projection is taken on the  $x$ - $y$  plane of a cross-sectional image by line integrating  $f(x, y)$  in a direction perpendicular to the  $x'$  axis where the angle between the  $x'$  axis and the  $x$  axis is  $\theta$ . As shown in Fig. 5.1-b, the Fourier Transform of this projection can be obtained by computing  $F(x, y)$  along  $u'$  where the angle between axis  $u'$  and axis

u is also  $\theta$ . Consequently, the entire frequency plane can be established by taking projections at various values of  $\theta$  from 0 to  $\pi$  and then transferring the information into the frequency domain.

### Filtered Back Projection Tomographic Image Reconstruction Method

A cross-sectional image can be reconstructed using the 2-D Inverse Fourier Transform to map the information from the u-v plane to the x-y plane as shown in eq. 5.1. When the Inverse Fourier Transform is expressed in a polar raster coordinate system, an additional term,  $\rho$  representing the radius in the frequency plane, is introduced in the integral. Since the integrations are separable, the first integration within the brackets is equivalent to the filtering at a given angle  $\theta$  using a filter whose kernel is  $|\rho|$ .

$$\begin{aligned}
 f(x, y) &= \int_{-\infty}^{\infty} \int_{-\infty}^{\infty} F(u, v) e^{j2\pi(u x + v y)} du dv \\
 &= \int_0^{2\pi} \int_0^{\infty} P(\theta, \rho) e^{j2\pi(x \rho \cos\theta + y \rho \sin\theta)} \rho d\rho d\theta \\
 &= \int_0^{\pi} \left\{ \int_{-\infty}^{\infty} P(\theta, \rho) |\rho| e^{j2\pi\rho r} d\rho \right\} d\theta \\
 &= \int_0^{\pi} Q(\theta, r) d\theta
 \end{aligned} \tag{5.1}$$

where  $r = x \cos \theta + y \sin \theta$ ,  $(\theta, \rho)$  and  $(\theta, r)$  are the radii and the angles along the polar raster scans corresponding to the  $u$ - $v$  and  $x$ - $y$  planes respectively. In eq. 5.1,  $f(x, y)$  is the value of the image at the coordinate  $(x, y)$ .  $F(u, v)$  is the Fourier representation of  $f(x, y)$  on the  $u$ - $v$  plane.  $P(\theta, \rho)$  is the Fourier presentation of a projection at angle  $\theta$  and radius  $\rho$ , and is equal to  $F(u, v)$  on the  $\theta$ - $\rho$  plane.  $Q(\theta, r)$  is the filtered projection on the  $\theta$ - $r$  plane. As shown in eq. 5.1, the filtered back projection  $Q(\theta, r)$  at a given  $\theta$  can be obtained by computing only the 1-D Fourier Transform and filtering it using a 1-D filter kernel shown in Fig. 5.2.

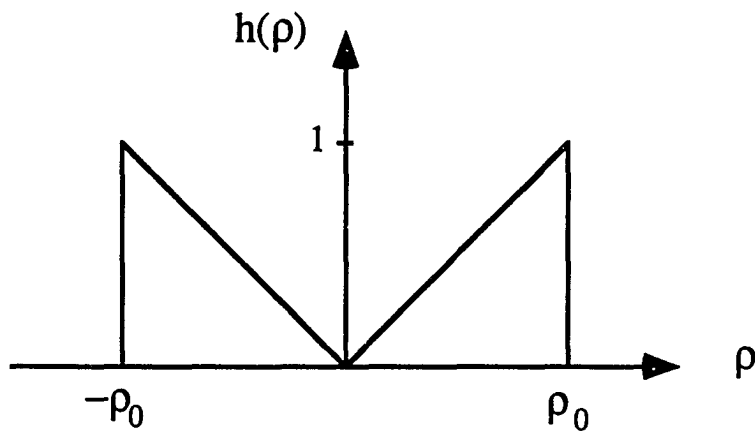


Fig. 5.2. Spatial frequency response of the radius filter.

The representation of eq. 5.1 in discrete form is the Filtered Back Projection (FBP) method which can be expressed as

$$\begin{aligned} x(i_1, i_2) &= \sum_{\theta=0}^{\pi} \sum_{\rho=-\rho_0}^{\rho_0} P(\theta, \rho) |\rho| e^{j2\pi\rho r} \\ &= \sum_{\theta=0}^{\pi} Q(\theta, r) \end{aligned} \quad (5.2)$$

where  $r = i_1 \cos\theta + i_2 \sin\theta$ ,

$i_1$  and  $i_2$  are coordinates in the discrete image plane, and  $x(i_1, i_2)$  represents the grey level of the  $(i_1, i_2)^{\text{th}}$  pixel. In eq. 5.2, the 1-D filtering operation can be performed separately and the result overlapped on the image plane. Since all the indices in eq. 5.2 are in the discrete form, interpolations are usually used.

It has been shown in Section 3.1 and Fig. 3.1, projections can also be represented by means of weighting factor  $w(i, j)$ 's which are the fractional areas intercepted by ray-sums of projections and pixels of the image. Therefore, the discrete form of the filtered back projection method of eq. 5.2 can also be expressed in terms of the back projection matrix,  $A^T$ . Using linear operator matrices, the FBP procedure can be expressed as

$$\begin{aligned} \mathbf{x} &= \sum_{q=1}^{mp} \mathbf{A}_q^T \mathbf{F}_{\text{INV}_q} \mathbf{R}_q \mathbf{F}_q \mathbf{b}_q \\ &= \mathbf{A}^T \mathbf{F}_{\text{INV}} \mathbf{R} \mathbf{F} \mathbf{b} \end{aligned} \quad (5.3)$$

where, the matrix  $A^T$  is the back projection operator matrix, the vector  $\mathbf{b}$  contains the measured projections defined in Section 3.1, the matrices  $\mathbf{F}$  and  $\mathbf{F}_{\text{INV}}$  are linear operators

representing Fourier and Inverse Fourier Transform operations respectively, the diagonal matrix  $\mathbf{R}$  is the kernel of the radius filter and  $n_p$  is the total number of projections. The matrices and vectors with the subscript  $q$  correspond to the  $q^{\text{th}}$  projection angle.

### 5.1.2 Iterative Filtered Back Projection Method

When the system is overdetermined, the FBP procedure in eq. 5.3 can be used iteratively to minimize the square errors in the frequency domain. An iterative procedure based on the basic Richardson (RF) method is given by the following difference equation

$$\mathbf{x}(k) = \mathbf{x}(k-1) + \alpha \mathbf{A}^T \mathbf{F}_{\text{INV}} \mathbf{R} \mathbf{F} [\mathbf{b} - \mathbf{A} \mathbf{x}(k-1)] \quad (5.4)$$

where  $k$  is the index of iterations,  $\alpha$  is the relaxation factor, matrices  $\mathbf{A}$  and  $\mathbf{A}^T$  are the forward projection operator matrix and back projection operator matrix as defined in eqs. 3.2 and 3.4. Fig. 5.3 shows the block diagram for the iterative filtered back projection algorithm.

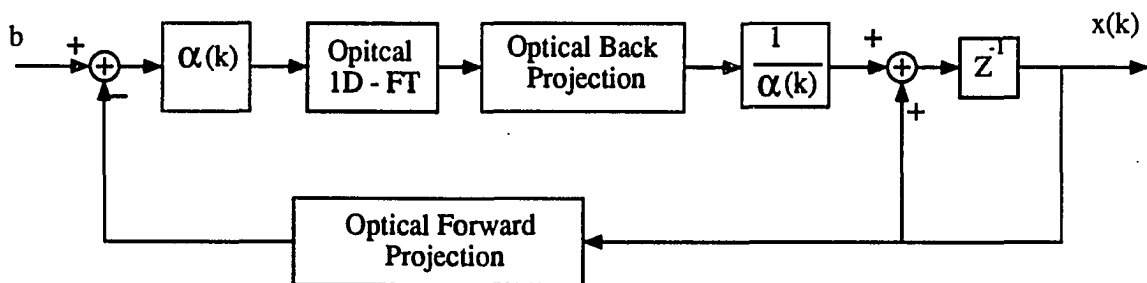


Fig. 5.3. A block diagram of the IFBP.

### Convergence of the solution

The IFBP expressed in eq. 5.4 can be considered as a time-invariant linear multi-variable feedback system with step input. The reconstructed image is the steady-state output which can be found using the z-transform and invoking the final value theorem. Using z-transforms, the difference equation in eq. 5.4 can be written as

$$\begin{aligned} \mathbf{x}[z] &= \mathbf{x}[z] z^{-1} + \alpha \mathbf{A}^T \mathbf{F}_{\text{INV}} \mathbf{R} \mathbf{F} [\mathbf{b}[z] - \mathbf{A} \mathbf{x}[z] z^{-1}] \\ &= [\mathbf{I} - [\mathbf{I} - \alpha \mathbf{A}^T \mathbf{F}_{\text{INV}} \mathbf{R} \mathbf{F} \mathbf{A}] z^{-1}] \alpha \mathbf{A}^T \mathbf{F}_{\text{INV}} \mathbf{R} \mathbf{F} \mathbf{b} \frac{z^{-1}}{1 - z^{-1}} \end{aligned} \quad (5.5)$$

Obviously, when the matrix  $[\mathbf{A}^T \mathbf{F}_{\text{INV}} \mathbf{R} \mathbf{F} \mathbf{A}]$  is non-singular and  $\alpha$  is chosen such that all eigenvalues of  $[\mathbf{I} - \alpha \mathbf{A}^T \mathbf{F}_{\text{INV}} \mathbf{R} \mathbf{F} \mathbf{A}]$  are within the unit circle, eq. 5.5 converges to

$$\begin{aligned} \lim_{k \rightarrow \infty} \mathbf{x}(k) &= \lim_{z \rightarrow 1} \mathbf{x}[z] \frac{1 - z^{-1}}{z^{-1}} \\ &= [\mathbf{A}^T \mathbf{F}_{\text{INV}} \mathbf{R} \mathbf{F} \mathbf{A}]^{-1} \mathbf{A}^T \mathbf{F}_{\text{INV}} \mathbf{R} \mathbf{F} \mathbf{b} \end{aligned} \quad (5.6)$$

Since the Inverse Fourier Transform matrix  $\mathbf{F}_{\text{INV}}$  is the conjugate transpose of the Fourier Transform matrix  $\mathbf{F}$ , i.e.,  $\mathbf{F}_{\text{INV}} = \mathbf{F}^*$ , and the diagonal matrix  $\mathbf{R}$  can be decomposed as  $\mathbf{R} = (\mathbf{R}^{\frac{1}{2}})^T \mathbf{R}^{\frac{1}{2}}$ , the algorithm minimizes

$$\begin{aligned} &\| \mathbf{R}^{\frac{1}{2}} \mathbf{F} \mathbf{A} \mathbf{x} - \mathbf{R}^{\frac{1}{2}} \mathbf{F} \mathbf{b} \|_2 \\ &= \| (\mathbf{R}^{\frac{1}{2}} \mathbf{F})(\mathbf{A} \mathbf{x} - \mathbf{b}) \|_2 \end{aligned} \quad (5.7)$$

where  $\| \cdot \|_2$  denotes the Euclidean norm of a vector. Eq. 5.7 shows that the solution of

IFBP is obtained by minimizing the least square error of the filtered projections in the frequency domain with a square root radius filter.

### **Convergence of the algorithm**

The diagonal matrix  $\mathbf{R}$  in eq. 5.4 represent the radius filter kernel as shown in Fig. 5.2. Unfortunately, the zero and near zero values in the radius filter operator matrix, reduce the rank of the system. For an  $M \times N$  system  $\mathbf{A} \mathbf{x} = \mathbf{b}$ , where  $M$  and  $N$  are the column and row dimensions of the matrix  $\mathbf{A}$  respectively, the dimensions of  $\mathbf{R}$  are  $M \times M$ . When the number of nonzero entries in the diagonal matrix  $\mathbf{R}$  is less than  $N$ , the system is singular and convergence is not guaranteed. In order to have enough nonzero entries in  $\mathbf{R}$ , the system has to be overdetermined, i.e., the number of projection data should be larger than the number of pixels in the reconstructed image.

### **Acceleration using the conjugate gradient method**

As described in Section 5.3, the conjugate gradient method can be used as an acceleration technique for solving overdetermined and underdetermined systems. When the system is not singular, the matrix  $[\mathbf{A}^T \mathbf{F}^T (\mathbf{R}^{1/2})^T \mathbf{R}^{1/2} \mathbf{F} \mathbf{A}]$  in the IFBP method is positive and symmetric definite. Therefore, the convergence of the IFBP can be accelerated using the conjugate gradient method. A unique solution is guaranteed.

## 5.2 Optical Implementation of The Radius Filter

In this section, the optical Fourier Transform using a two lens system is briefly described. An optical complementary filtering structure implementing the radius filter of the FBP is then introduced.

### 5.2.1 Fourier Transform by Lens

Consider a two lens coherent optical system as shown in Fig. 5.4, where  $F_1$  and  $F_2$  are the focal lengths of the lenses respectively. If an image,  $f(x, y)$ , is placed at the front focal plane of the first lens, its Fourier Transform in the spatial frequency domain,  $g(u,v)$ , is obtained at the back focal plane [12, 50, 79]:

$$\begin{aligned}
 g(u, v) &= \frac{c_1}{F_1} \iint f(x, y) e^{-j 2 \pi \frac{x u + y v}{\lambda F_1}} dx dy \\
 &= \frac{c_1}{F_1} \mathcal{F}\left\{\frac{u}{\lambda F_1}, \frac{v}{\lambda F_1}\right\}
 \end{aligned} \tag{5.8}$$

where  $c_1$  is a constant and  $\ell$  is the wave length of the monochromatic light. The image at the back focal plane of the second lens is a "flipped" Inverse Fourier Transform of  $g(u,v)$ :

$$\begin{aligned}
 h(x', y') &= \frac{c_2}{F_2} \iint g(u, v) e^{-j 2 \pi \frac{x'u+y'v}{\lambda F_2}} du dv \\
 &= c_3 \frac{F_1}{F_2} \iint F\left\{\frac{u}{\lambda F_1}, \frac{v}{\lambda F_1}\right\} e^{j 2 \pi \left\{(-x')\left(\frac{u}{\lambda F_1}\right)+(-y')\left(\frac{v}{\lambda F_1}\right)\right\}} d\frac{u}{\lambda F_1} d\frac{v}{\lambda F_1} \\
 &= c_3 \frac{F_1}{F_2} f\left(-\frac{F_1}{F_2} x', -\frac{F_1}{F_2} y'\right) \tag{5.9}
 \end{aligned}$$

where  $c_2$  and  $c_3$  are constants and  $F_2 / F_1$  is the magnification coefficient.

If a spatial frequency mask is placed between the back focal plane of the first lens and the front focal plane of the second lens,  $h(x', y')$  represents a filtered version of the original image.

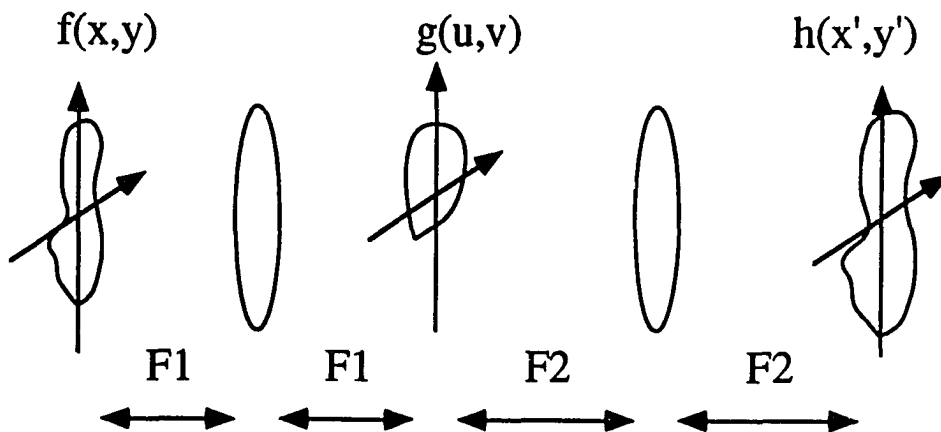


Fig. 5.4. A two lens system implementing a 2-D Fourier transform spatial filter.

In coherent optical systems, the representations of  $f(x, y)$ ,  $g(u, v)$ ,  $h(x', y')$  and the filter mask are usually given in terms of the magnitude of the light. In contrast, in an incoherent optical system, the intensity is used instead of the magnitude. In optical information processing, coherent optical Fourier filtering usually suffers from speckle noise caused by the granularity of imaging devices and dust [79]. This is considered to be one of the major obstacles in optoelectronic implementations of tomography.

### **Frequency Response of Coherent Optical System**

The finite passband in the Coherent Transfer Function (CTF), within which the coherent imaging system exists, passes all frequency components without amplitude and phase distortion [79]. At the boundary of this pass band, the frequency response drops to zero, implying that the frequency components outside the passband are completely attenuated. The frequency response of a circular aperture is shown in Fig. 5.5. The cutoff frequency in terms of the image spatial frequency is

$$\rho_0 = \frac{D}{2 \lambda F} \quad (5.10)$$

where  $D$  is the diameter of the aperture.

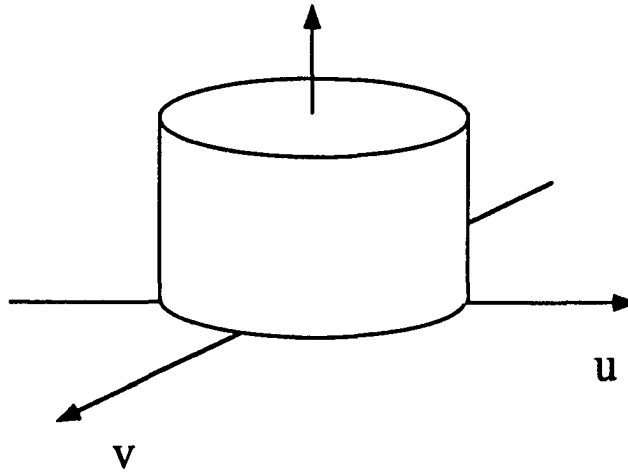


Fig. 5.5. Frequency response of CTM for a circular aperture.

### Frequency Response of Incoherent Optical System

For incoherent optical systems, the spatial frequency spectrum of the image can be obtained by applying the complex weighting factor  $H(\rho)$  to the spatial frequency spectrum of the object intensity. The function  $H(\rho)$  is known as the optical transfer function (OTF) and the modulus  $|H|$  is the modulation transfer function (MTF) [79].

The OTF for the aberration-free lens system of a circular aperture can be found to be

$$H(\rho) = \begin{cases} \frac{2}{\pi} \cos^{-1} \left( \frac{\rho}{2 \rho_0} \right) - \frac{\rho}{\pi \rho_0} \sqrt{1 - \left( \frac{\rho}{2 \rho_0} \right)^2}, & \rho \leq 2 \rho_0 \\ 0, & \text{otherwise} \end{cases} \quad (5.11)$$

where  $\rho_0$  is given in eq. 5.10. The spectrum of  $H(\rho)$  is shown in Fig. 5.6.

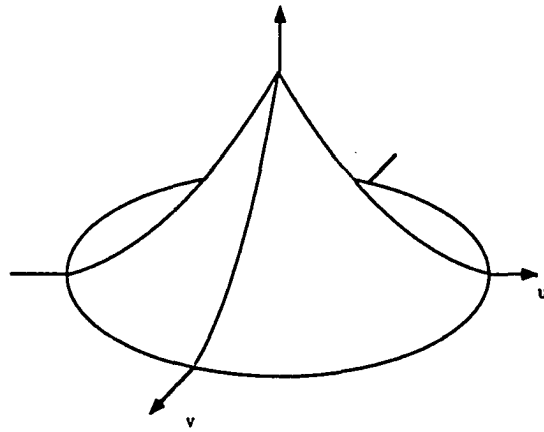


Fig. 5.6. The frequency response of the OTF for a circular aperture.

### 5.2.2 Optical Complementary Radius Filter

The 1-D radius filter in the filtered back projection method has a frequency response given by

$$h(\rho) = \frac{\rho}{\rho_0}, \quad 0 \leq \rho \leq \rho_0 \quad (5.12)$$

where  $\rho_0$  is the cut-off frequency. The frequency response is shown in Fig. 5.2. The filtered output is

$$g(r) = \text{IFT}\{ \text{FT}\{ f(r) \} \cdot h(\rho) \} \quad (5.13)$$

where  $g(r)$  and  $f(r)$  are the output and the input of the filter, respectively.

Since  $h(0) = 0$ , the zero frequency component should be eliminated completely and the dynamic range of the outputs must be bipolar. However, in an optoelectronic system, photo detectors can only detect intensity of light, and consequently both input signal and output signal should be biased to non-negative values. Therefore, the optical filter is

required to be able to separate the zero frequency component of the bias and the zero frequency component of the signal. The zero frequency component of the bias should be passed while suppressing the zero frequency component of the signal. These requirements are contradictory. In order to circumvent the conflicting requirements, an optical complementary filter is proposed. The complementary radius filter decomposes the original radius filter into two components, one is the filtered complementary function of the input while the other is the original input. The output of radius filter is obtained by superimposing the filtered signal on the original input. The frequency response of the low pass complementary filtering channel is given by

$$\begin{aligned}\bar{h}(\rho) &= d(\rho) - h(\rho) \\ &= \frac{\rho_0 - \rho}{\rho_0}\end{aligned}\tag{5.14}$$

$$\text{where } d(\rho) = \begin{cases} 1, & |\rho| \leq \rho_0 \\ 0, & \text{otherwise.} \end{cases}$$

The frequency response is shown in Fig. 5.7. The output of the filter can be described as follows

$$\begin{aligned}g'(r) &= \left[\frac{c}{2} + f(r)\right] + \text{IFT}\{\text{FT}\left\{\frac{c}{2} - f(r)\right\} \cdot \bar{h}(\rho)\} \\ &= \frac{c}{2} + \text{IFT}\{\text{FT}\{f(r)\}\} + \text{IFT}\{\text{FT}\left\{\frac{c}{2}\right\} \cdot \bar{h}(\rho)\} + \text{IFT}\{\text{FT}\{f(r)\} \cdot [-\bar{h}(\rho)]\} \\ &= c + \text{IFT}\{\text{FT}\{f(r)\} \cdot [d(\rho) - \bar{h}(\rho)]\} \\ &= c + \text{IFT}\{\text{FT}\{f(r)\} \cdot h(\rho)\} \\ &= c + g(r)\end{aligned}\tag{5.15}$$

where  $g'(r)$  is the output of the complementary filter and  $c/2$  is the value of the zero frequency component bias light intensity applied to both the filtered and unfiltered channels. The terms  $[c / 2 + f(r)]$  and  $[c / 2 - f(r)]$  in eq. 5.15 represent biased nonnegative inputs applied to the optical filter. This filter can be implemented by a two lens system with symmetrical positive and negative response SLM's. Fig. 5.8 shows I/O response curves of a pair of symmetric positive and negative SLM's [49].

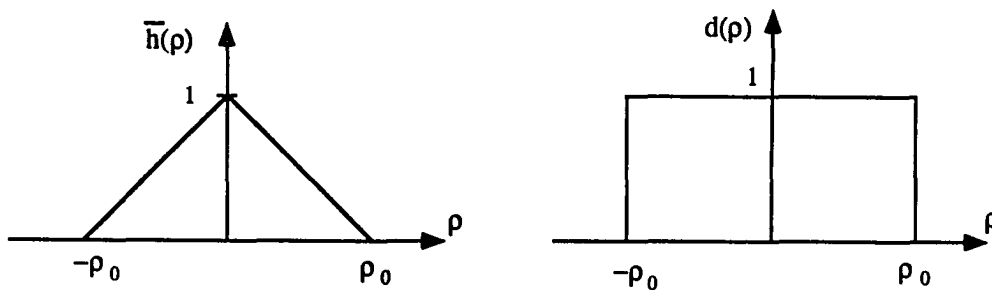


Fig. 5.7. The frequency responses of the negative and positive channels of the complementary filter.

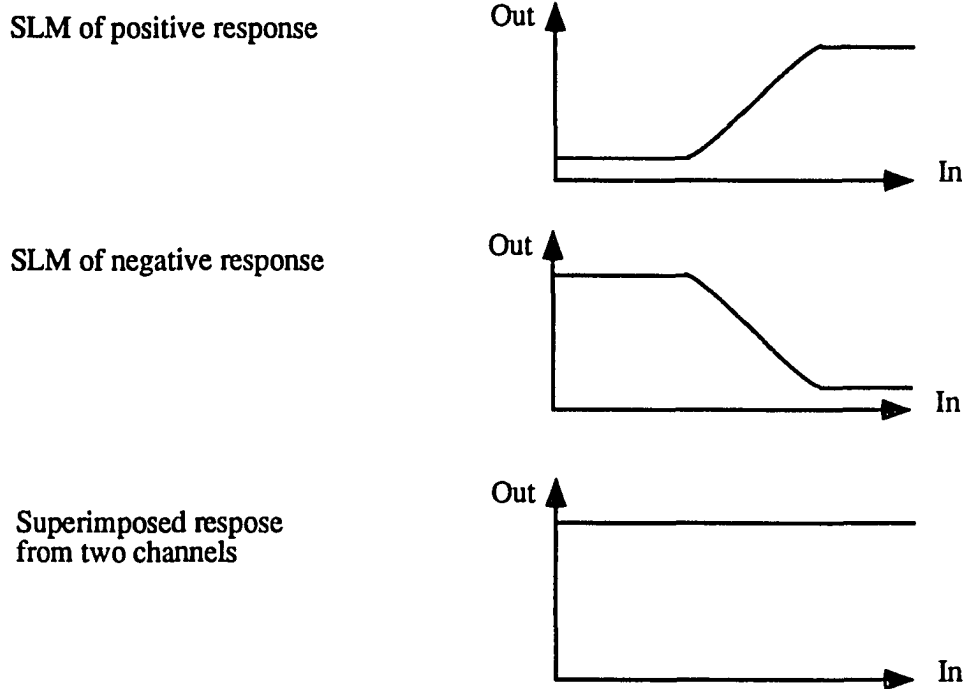


Fig. 5.8. The characteristic curves of a negative response SLM and a positive response SLM.

The dynamic range of the filtered output is  $c \pm c / 2$  representing about 33 % loss in the dynamic range. However, the loss can be compensated for in the form of a zero frequency component bias in the input to the next optically addressed SLM.

Using the complementary radius filter structure, the high pass spatial frequency response of the radius filter is replaced by a low pass response characteristic. In addition, the proposed feedback scheme offers increased tolerance to distortion introduced at the filter stage. The complementary radius can be implemented using incoherent optical systems, such as, the Ronchi pupil and optical transfer function (OTF) synthesis techniques [46].

### 5.3 Optoelectronic Implementation

#### 5.3.1 Model implementation

The iterative procedure of the IFBP in eq. 5.4 can be rewritten as a summation in terms of operations of each projection angle. Let  $q$  be an index of projections and  $q = 1, 2, \dots, n_p$ , and  $n_p$  be the number of angles, then

$$\begin{aligned} \mathbf{x}(k) = & \mathbf{x}(k-1) + \\ & \alpha \sum_{q=1}^{n_p} \frac{\mathbf{A}_q^T}{\mu(k)} \mathbf{F}_{\text{INV}_q} \mathbf{R}_q \mathbf{F}_q \mu(k) [\hat{\mathbf{b}}_q - \mathbf{A}_q \mathbf{x}(k-1)] \end{aligned} \quad (5.16)$$

where  $\mu(k)$  is inserted as a scaling factor used to keep optoelectronic devices working at their full dynamic range and  $\alpha$  is a relaxation coefficient. Variables in eq. 16 with subscript  $q$  represent the corresponding submatrices and subvector at the  $q^{\text{th}}$  projection angle respectively.

#### 5.3.2 Optoelectronic structure

Fig. 5.9 shows an optoelectronic structure for implementing the IFBP algorithm. There are three major functional blocks in the structure which implement the back and projection, the forward projection, and the optical radius filter. Implementations of forward and back projections are similar to those used for the implementing SIRT and are described in detail in Section 3.3. Amplifiers are inserted prior to optical filtering. Magnitudes of the error terms are scaled by the factor  $\mu(k)$  up to the full device range before filtering is performed. During the back projection, the error correction terms are re-scaled

correspondingly down to their correct magnitudes by varying the exposure period. As the number of iterations increase, the magnitudes of the errors decrease. Therefore, the distortion caused by the noise associated with the optical transform and the finite dynamic range of the device are minimized by reducing relative errors using the feedback scheme.

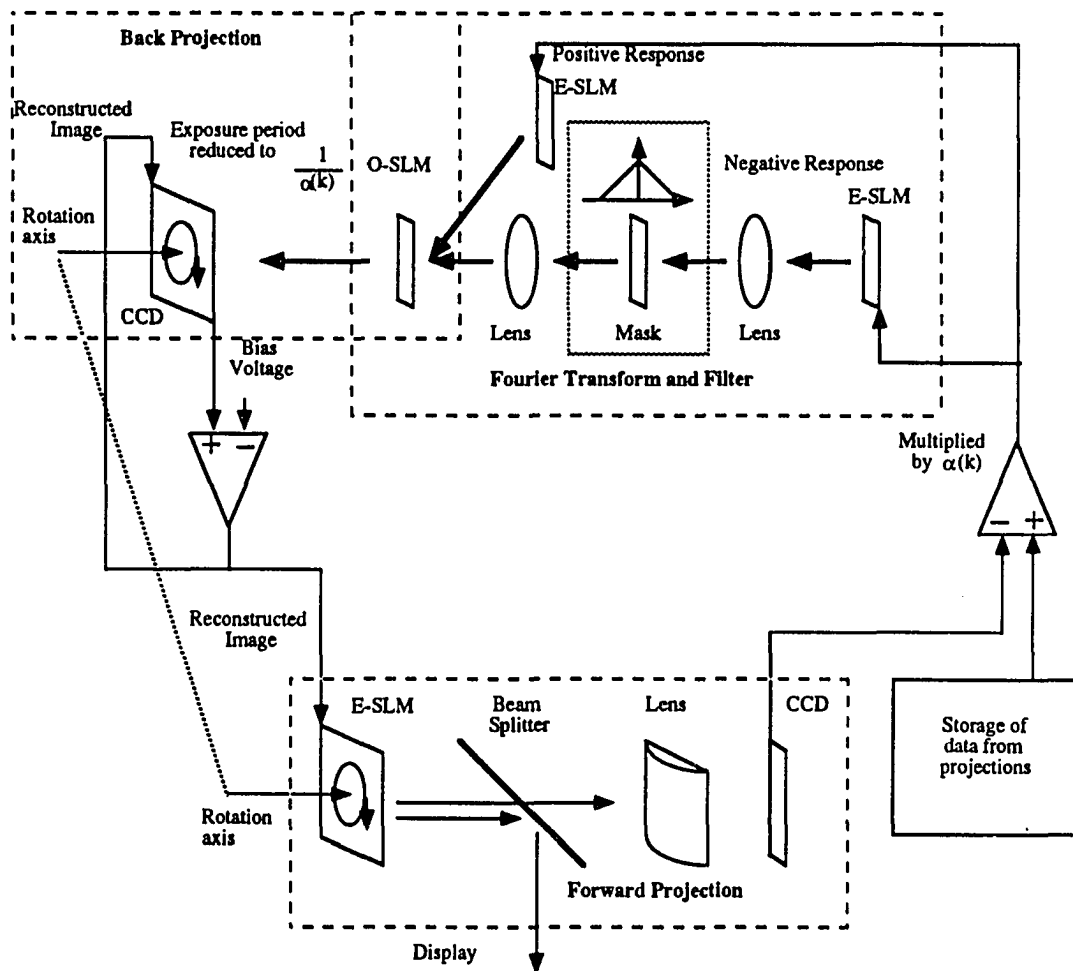


Fig. 5.9. The structure of an optoelectronic implementation of the IFBP.

#### 5.4 Simulation Studies

Fig. 5.10 shows the result obtained by simulating the IFBP algorithm for synthesizing a  $128 \times 128$  image. The dynamic range of the SLM's and the filter are set at 256 and  $\pm 16$  respectively. The system is overdetermined ( $M > N$ ) to the same degree as that employed for the simulation of the SIRT in sections 3.5.2 and 3.5.3. The result shows that the first reconstructed image is distorted due to the poor accuracy associated with the filtering.

The distortion is corrected after the second and third iteration. When these results are compared with the results obtained in the simulation of the SLM/CCD implementation of SIRT in Fig. 3.15, it is seen that the number of iterations required to obtain the same level of performance is significantly lower when the IFBP method is employed. In addition, the distortion is reduced when the numbers of distinguishable dynamic ranges of the SLM's are set at the same level as before, i.e., 256.

Fig. 5.11 shows reconstructed image ( $32 \times 32$ ) converging to the original cross-section. The number of projections is 60 and projections are taken from a  $32 \times 32$  original cross-sectional image.

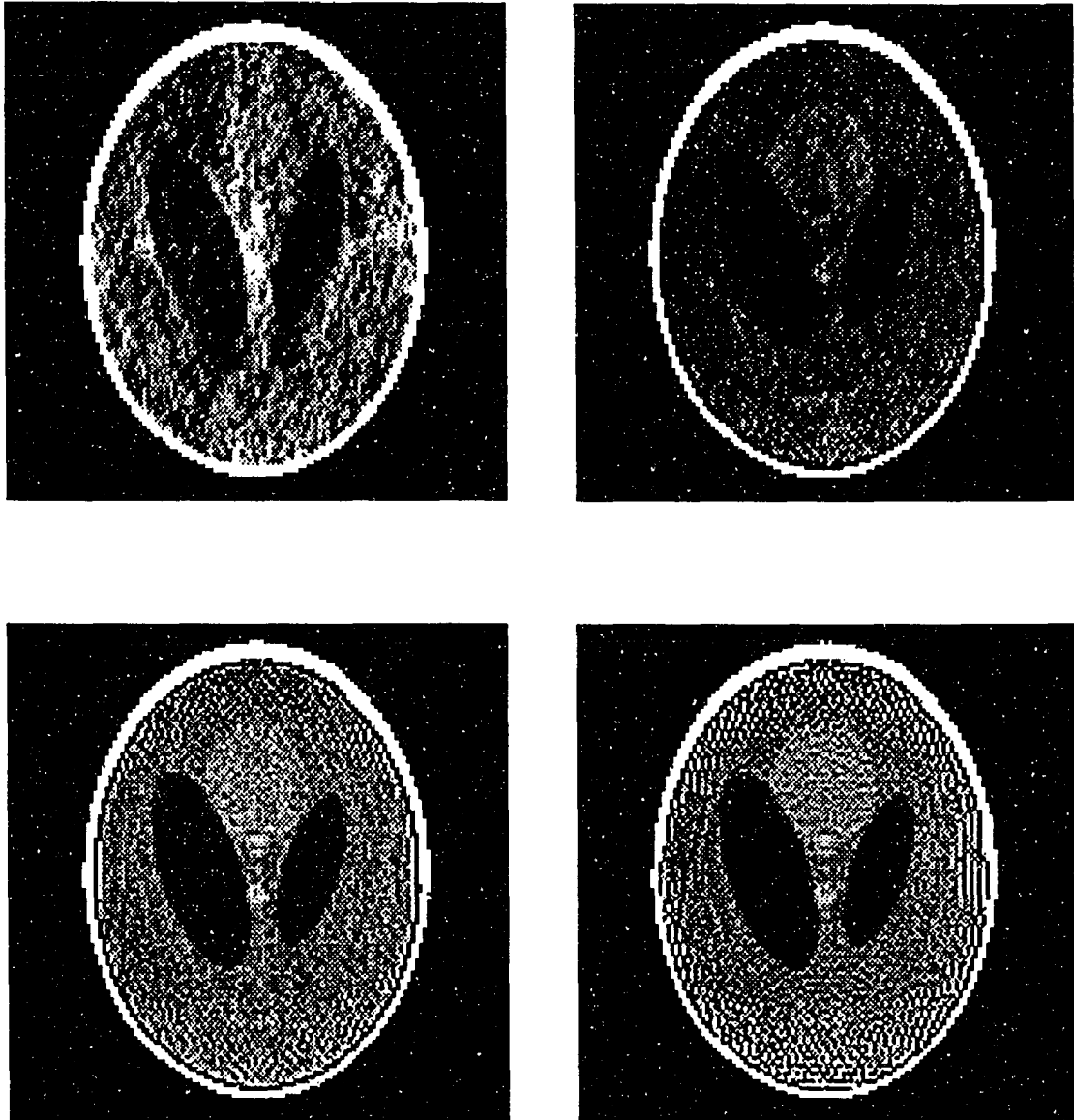


Fig. 5.10. Reconstructed images obtained using the IFBP at the 1<sup>st</sup>, 2<sup>nd</sup>, 3<sup>rd</sup> and the 64<sup>th</sup> iterations with finite numbers of distinguishable grey levels ( $\pm 16$  for the filter and 256 for SLM's)

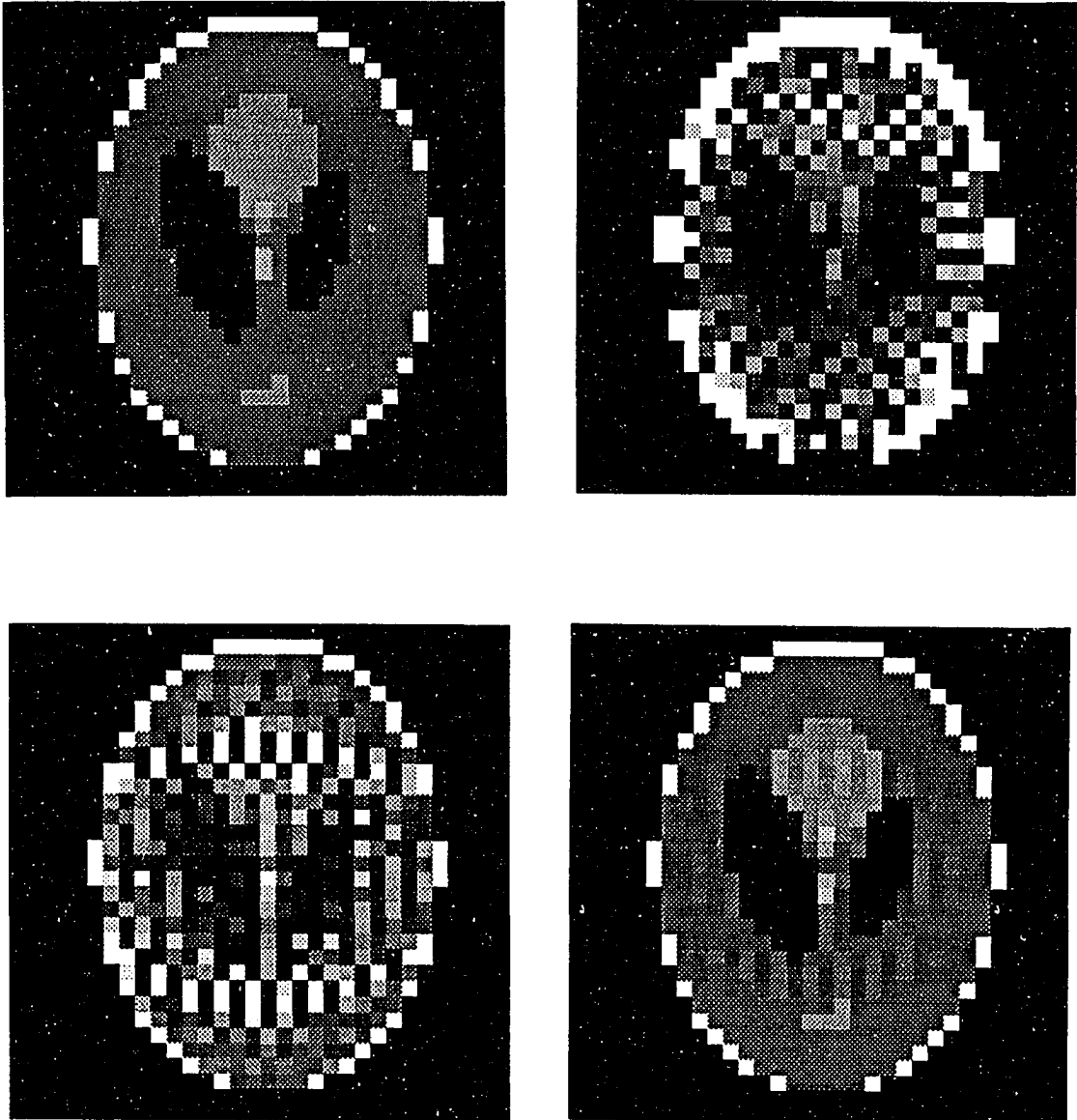


Fig. 5.11. An original  $32 \times 32$  phantom and the reconstructed images using the IFBP at the 1<sup>st</sup>, 256<sup>th</sup> and 30,720<sup>th</sup> iterations.

### 5.5 Summary

The IFBP algorithm is an iterative version of the FBP algorithm. With the IFBP, iterative reconstructions are speeded up significantly and distortion in the reconstructed images is reduced. When the system is overdetermined, the solution of IFBP minimizes the least square errors of the filtered projections in the frequency domain with a square root radius filter.

The potential application of this algorithm is in high speed and low cost optoelectronic systems. Inaccuracies associated with optical systems is minimized within a few iterations. The structure can also be used to implement the Projection Space Iterative Reconstruction-Reprojection (PIRR) algorithm in limited view tomography applications [26-27].

## **CHAPTER 6. PIRT WITH PARTIAL CONVOLUTION AND CONSIDERATIONS FOR BUILDING A PROTOTYPE**

In Chapter 5, the PIRT and PIRT-CG algorithms together with schemes for implementing them using optoelectronic devices were discussed. In this Chapter, another accelerated method utilizing an FIR filter is proposed. In addition, a hybrid prototype using off-the-shelf devices for implementing the algorithms is proposed.

The convolution back projection method (CBP) for direct tomographic image reconstruction utilizes spatial domain FIR filtering instead of frequency domain filtering for the filtered back projection method (FBP). An hybrid structure implementing digital FIR filtering and optical back projection has been proposed by Gmitro, et. al. [48]. However, the large size of the FIR filter increases the cost and processing time. In addition, distortions caused by the optical back projection stage cannot be avoided. The PIRT iterative procedure, not only allows distortion to be corrected, but also the length of the FIR filter can be significantly reduced. It will be shown that the reconstruction can be accelerated process considerably by using only a few taps. It will also be shown that the PIRT with partial convolution (PIRT-PC) converges to the minimum-norm solution for an underdetermined system. In order to circumvent the limitations of finite dynamic range of the both back projection and forward projection SLM's, an alternative iterative procedure - called the residual iterative reconstruction technique (RIRT) is presented.

The rationale behind optical implementations of tomographic forward and back projections has been described extensively in literature. The optical forward projection processor is also called optical Radon Transformer [45-46] and employs the same principle as the optical Hough transform feature space processor [45, 46, 80]. Optical back projection processors have been used for implementing direct reconstruction algorithms [44-48]. The optoelectronic implementations of iterative algorithms using CCD and SLM arrays were discussed previously [5, 6, 8, 9]. A hybrid prototype consisting of an SLM/CCD back projection processor, a digital auxiliary image processor, an SLM/CCD forward projection processor and an auxiliary projection processor is proposed in the chapter. The SLM and the CCD arrays in the back projection processors are a linear FLC SLM (Ferroelectric Liquid Crystal SLM) array and a commercial CCD image detecting array respectively. The SLM and CCD arrays in the forward processor consists of a LCTV SLM (Liquid Crystal TV SLM) panel and a linear CCD detector array respectively. The auxiliary processors in the image and projection spaces can be built using commercial microprocessors. The two additional electronic digital microprocessor-based auxiliary processors are important for flexibility and ensuring stability.

In an analog electrically addressed SLM, the output light intensity is proportional to the applied voltage. Several distinguishable gray levels can be obtained using such SLM's. In the case of binary SLM's, the output can be either in the "ON" or "OFF" states. Analog SLM's are very often used in image and signal processing applications. However, commercial available analog SLM's, such as the LCTV, can only operate at the speed of

about 100 Hz. Binary SLM's, such as FLC SLM, can however be operated at a rate of about 100 KHz. In many applications, analog SLM's operating at KHz rates are desired. In this Chapter, a method of implementing high speed analog SLM's for generating multiple gray levels using fast binary SLM's is described.

The CBP method is briefly reviewed in Section 6.1. In Section 6.2, the PIRT-PC technique is introduced while Section 6.3 discusses the alternative residual iterative procedure. Section 6.4 presents a hybrid prototype for implementing iterative tomographic reconstruction procedures. In Section 6.5, methods for implementing high speed continuously variable analog SLM using available binary SLM's are introduced. Discussions relating to dynamic ranges of reconstruction are presented in Section 6.6. Simulation results modeling off-the-shelf devices are presented in Section 6.7. Section 6.8 summarizes the information presented in the Chapter.

### 6.1 Convolution Back Projection Method

The convolution back projection method can be derived from the filtered back projection method discussed in Section 6.1. A filtered projection in eq. 5.1 can be described as

$$Q(\theta, r) = \int_{-p_0}^{p_0} P(\theta, \rho) H(\rho) e^{j2\pi\rho r} d\rho \quad (6.1)$$

$$\text{where } H(\rho) = \begin{cases} |\rho| & |\rho| < \rho_0 \\ 0 & \text{otherwise} \end{cases}$$

and  $P(\theta, r)$  is the Fourier representation of the measured projections. The frequency response is shown in fig. 5.2. The impulse response,  $h(r)$  in the spatial domain, is given by the inverse Fourier transform of  $H(\rho)$  which is [10]

$$\begin{aligned}
 h(r) &= \int_{-\infty}^{\infty} H(\rho) e^{j2\pi\rho r} d\rho \\
 &= 2 \int_0^{\rho_0} \rho \left( \frac{e^{j2\pi\rho r} + e^{-j2\pi\rho r}}{2} \right) d\rho \quad (6.2) \\
 &= 2 \rho_0 \left[ \frac{\sin 2\pi r \rho_0}{2\pi r \rho_0} - \frac{1}{2} \left( \frac{\sin r \rho_0}{r \rho_0} \right)^2 \right]
 \end{aligned}$$

In the discrete case, we substitute the sampling interval  $T = 1/2 \rho_0$  in eq. 6.2, to obtain the impulse response  $h(i)$ ,  $i = -\infty$  to  $\infty$ ,

$$h(i) = 2 \rho_0 \left[ \frac{\sin \pi i}{\pi i} - \frac{1}{2} \left( \frac{\sin \pi i / 2}{\pi i / 2} \right)^2 \right] \quad (6.3)$$

which is shown in Fig. 6.1. The impulse response can be rewritten as

$$h(i) = \begin{cases} \rho_0 & i = 0 \\ 0, & i \text{ even} \\ -\rho_0 \cdot \frac{4}{\pi^2} \cdot \frac{1}{i^2}, & i \text{ odd} \end{cases} \quad (6.4)$$

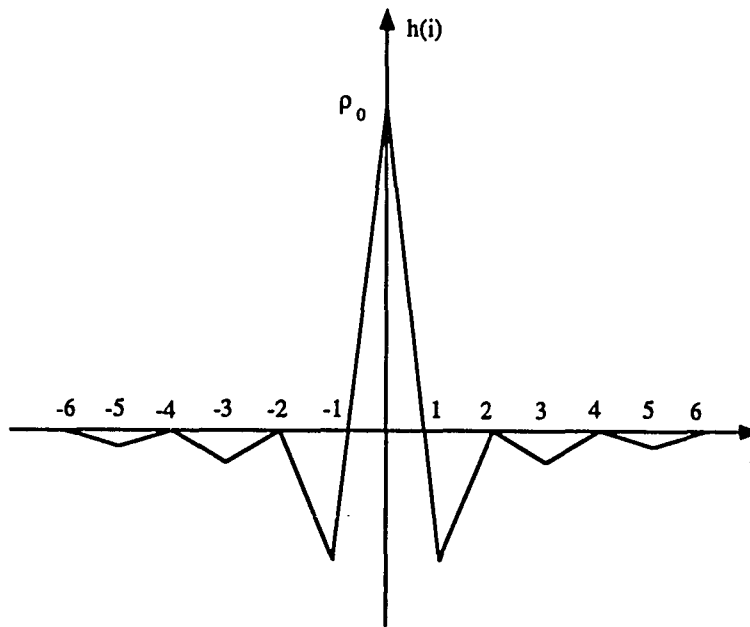


Fig. 6.1. The impulse response of the radius filter.

Using the convolution theorem, the filtered projection in eq. 6.1 can be written as

$$Q(\theta, r) = \int_{-\infty}^{\infty} b(\theta, r') h(r - r') dr' \quad (6.5)$$

where  $b(\theta, r)$  is the measured projection. In discrete form

$$Q(\theta, i) = \sum_{k=-\infty}^{\infty} h(k) b(\theta, i - k) \quad (6.6)$$

As in the case of the FBP method described by eq. 5.2, the cross-sectional image can be reconstructed by superimposing all filtered projections at different projection angles in the image plane. Using the convention defined in eq's. 1.1 to 1.3, the convolution back

projection method can be expressed in matrix form. We truncate  $h[i]$  and incorporate a finite number of samples in the impulse response the matrix  $\mathbf{H}$ . Then, the reconstruction scheme can be expressed as

$$\mathbf{x} = \mathbf{A}^T \mathbf{H} \mathbf{b} \quad (6.7)$$

where  $\mathbf{H}$  is an  $M \times M$  matrix representing the zero-padded convolution operation given by

$$\mathbf{H} = \begin{bmatrix} \tilde{\mathbf{H}} & \mathbf{0} & \mathbf{0} & \dots & \mathbf{0} \\ \mathbf{0} & \tilde{\mathbf{H}} & \mathbf{0} & \dots & \mathbf{0} \\ & & & \dots & \\ \mathbf{0} & \mathbf{0} & \mathbf{0} & \dots & \tilde{\mathbf{H}} \end{bmatrix} \quad (6.8)$$

$$\tilde{\mathbf{H}} = \begin{bmatrix} h(0) & h(1) & h(2) & \dots & h(m-1) \\ h(1) & h(0) & h(1) & \dots & h(m-2) \\ h(2) & h(1) & h(0) & \dots & h(m-3) \\ & & & \dots & \\ h(m-1) & h(m-2) & h(m-3) & \dots & h(0) \end{bmatrix}$$

and  $m$  is the number of ray-sums per projection. The matrix  $\mathbf{H}$  is not only symmetric but also positive definite because it is diagonally dominant for any finite  $m$ . The diagonal dominant nature can be shown as follows,

$$\begin{aligned}
\sum_{\substack{i=-\infty \\ i \neq 0}}^{\infty} |h(i)| &= \left( 2 \cdot \frac{4 \rho_0}{\pi^2} \right) \cdot \left( \sum_{j=1}^{\infty} \frac{1}{(2j-1)^2} \right) \\
&= \left( \frac{8 \rho_0}{\pi^2} \right) \cdot \left( \frac{\pi^2}{8} \right) \\
&= \rho_0
\end{aligned} \tag{6.9}$$

and

$$h(0) = \sum_{\substack{i=-\infty \\ i \neq 0}}^{\infty} |h(i)| = \rho_0$$

Therefore, when  $m$  is finite,

$$h(0) > \sum_{\substack{-m \\ -m, m \neq 0}}^m |h(i)| \tag{6.10}$$

## 6.2 Projection Iterative Reconstruction Technique

### Employing Partial Convolution (PIRT -PC)

It has been shown that, when the dimensions of the system are finite,  $\mathbf{H}$  is symmetric and positive definite and the inverse,  $\mathbf{H}^{-1}$ , exists. A reduced order convolution scheme can be used as an FIR filter to accelerate the convergence of the PIRT algorithm. The improved algorithm can be expressed as

$$\mathbf{t}_k = \mathbf{t}_{k-1} + \alpha \mathbf{H} [\mathbf{b} - \mathbf{A} \mathbf{x}_{k-1}] \quad (6.11)$$

$$\mathbf{x}_k = \beta \mathbf{A}^T \mathbf{t}_k$$

where  $\beta = 1 / \|\mathbf{A} \mathbf{A}^T\|_2$  is used to normalize the projections and  $\alpha$  is chosen so that  $\|\mathbf{I} - \alpha \beta \mathbf{A} \mathbf{A}^T\|_2 < 1$ . The solution will converge to the minimum-norm solution provided the system is underdetermined

$$\begin{aligned} \lim_{k \rightarrow \infty} \mathbf{t}_k &= [\beta \mathbf{H} \mathbf{A} \mathbf{A}^T]^{-1} \mathbf{H} \mathbf{b} \\ &= \frac{1}{\beta} [\mathbf{A} \mathbf{A}^T]^{-1} \mathbf{b} \end{aligned} \quad (6.12)$$

and

$$\lim_{k \rightarrow \infty} \mathbf{x}_k = \mathbf{A}^T [\mathbf{A} \mathbf{A}^T]^{-1} \mathbf{b}$$

Eq. 6.11 represents the basic PIRT accelerated by partial convolutions (PIRT-PC). The coefficients of the  $n^{\text{th}}$  order filter are given by

$$h(i) = \begin{cases} \rho_0, & i = 0 \\ -\rho_0 \cdot \frac{4}{\pi^2} \cdot \frac{1}{i^2}, & i \text{ odd and } i \leq n \\ 0, & \text{otherwise.} \end{cases} \quad (6.13)$$

Employing the reduced convolution, reconstructions of the high frequency components are speeded up. Usually, only a few taps are needed in order to accelerate the convergence of high frequency components. When the order of the FIR filter reduces to zero,  $\mathbf{H}$  becomes an identity matrix reducing the approach to the basic PIRT.

### 6.3 Residual Iterative Reconstruction Techniques

Let  $\mathbf{r}_k$  denote the residual in the projection space. A tomographic reconstruction system using the information contained in the residual to arrive at the minimum-norm solution can be described as follows

$$\begin{aligned}
 \mathbf{r}_k &= \mathbf{r}_{k-1} - \alpha \mathbf{A} \mathbf{A}^T \mathbf{H} \mathbf{r}_{k-1} \\
 &= \mathbf{r}_{k-1} + \mathbf{A} \mathbf{d}_{k-1} \\
 \mathbf{d}_k &= \alpha \mathbf{A}^T \mathbf{H} \mathbf{r}_k \\
 \mathbf{x}_k &= \mathbf{x}_{k-1} + \mathbf{d}_k
 \end{aligned} \tag{6.14}$$

where  $\mathbf{H}$  is the partial convolution matrix and  $\alpha$  is chosen so that  $\|\mathbf{I} - \alpha \mathbf{A} \mathbf{A}^T \mathbf{H}\| < 1$ . The initial values can be chosen as  $\mathbf{r}_0 = \mathbf{b}$  and  $\mathbf{x}_0 = \mathbf{0}$ . The method described by eq. 6.14 is similar to the steepest descent method with a fixed descent step  $\alpha$ . The matrix  $\mathbf{H}$  can be considered as a preconditioning matrix. The algorithm expressed by eq. 6.9 will be referred to as the residual iterative reconstruction technique (RIRT).

The convergence properties can be derived as follows. By substituting  $\mathbf{r}_{k-m}$  by  $[\mathbf{I} - \alpha \mathbf{A} \mathbf{A}^T] \mathbf{r}_{k-(m+1)}$  into eq. 6.14 recursively until  $m = k - 1$ , we obtain

$$\begin{aligned}
 \mathbf{r}_k &= [\mathbf{I} - \alpha \mathbf{A} \mathbf{A}^T \mathbf{H}] \mathbf{r}_{k-1} \\
 &= [\mathbf{I} - \alpha \mathbf{A} \mathbf{A}^T \mathbf{H}]^k \mathbf{r}_0
 \end{aligned} \tag{6.15}$$

and

$$x_n = \sum_{k=0}^n \alpha A^T H r_k \quad (6.16)$$

Substituting eq. 6.15 into eq. 6.16

$$\begin{aligned} x_n &= \alpha A^T H \left\{ \sum_{k=0}^n [I - \alpha A A^T H]^k \right\} r_0 \\ &= \alpha A^T H \{ I - [I - \alpha A A^T H] \}^{-1} \\ &\quad \left\{ [I - \alpha A A^T H] \left\{ \sum_{k=0}^n [I - \alpha A A^T H]^k \right\} \right\} r_0 \\ &= A^T [A A^T]^{-1} \{ I - [I - \alpha A A^T H]^{n+1} \} r_0 \end{aligned} \quad (6.17)$$

When  $\| I - \alpha A A^T \|_2 < 1$ , and  $n \rightarrow \infty$ ,

$$[I - \alpha A A^T]^{n+1} \rightarrow 0 \quad (6.18)$$

The solution,  $x_n$ , converges to

$$\lim_{n \rightarrow \infty} x(n) = A^T [A A^T]^{-1} r_0 \quad (6.19)$$

where  $r_0 = b$

An alternative iterative procedure can be written as

$$r_k = r_{k-1} - \alpha A A^T H r_{k-1} \quad (6.20)$$

$$t_k = t_{k-1} + \alpha H r_k$$

The final solution is

$$\mathbf{x} = \mathbf{A}^T \lim_{k \rightarrow \infty} \mathbf{t}_k \quad (6.21)$$

For an under determined system, the solution obtained using the algorithms described by eqs. 6.14 and 6.20 are the same if numerical errors are ignored. If the system is overdetermined, the state vector  $\mathbf{t}$  given by eq. 6.10 will diverge in the projection space.

#### 6.4 A Hybrid Prototype for Iterative Reconstruction Algorithms

Optoelectronic architectures for implementing a variety of iterative reconstruction algorithms have been outlined in previous Chapters. This section describes a hybrid prototypic system that can be built to establish the proof of principle. The hybrid system employs off-the-shelf devices.

Fig. 6.2 shows a line diagram outlining the basic building blocks in the system. The building blocks include

- . An Optoelectronic Back Projection Processor.
- . An Optoelectronic Forward Projection Processor.
- . An Image Space Auxiliary Processor.
- . A Projection Space Auxiliary Processor.

Each of the building blocks is described briefly in the following sections.

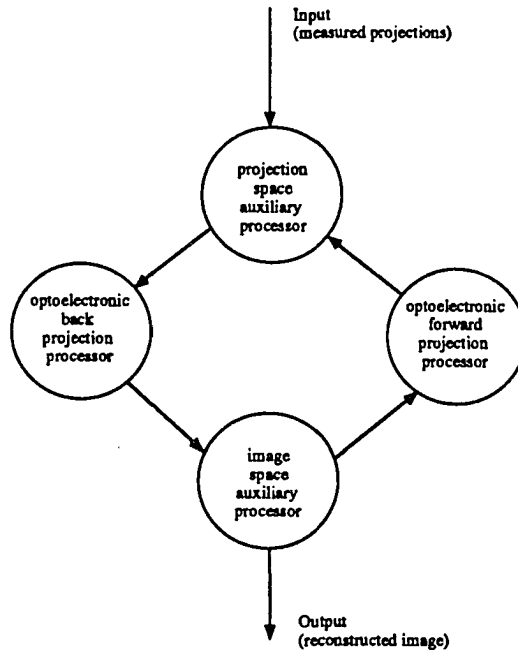


Fig. 6.2. A line diagram of the proposed hybrid prototype.

#### 6.4.1 The optoelectronic back projection processor

The back projection operations in tomographic image reconstruction involves mapping the data in the projection space into the image space from all the measured projection angles. The optoelectronic back projection processor shown in Fig. 6.3 performs the tomographic back projection operations. It consists of:

- . a linear array of analog SLM's and a cylindrical lens.
- . an image detection array.
- . an image rotator.

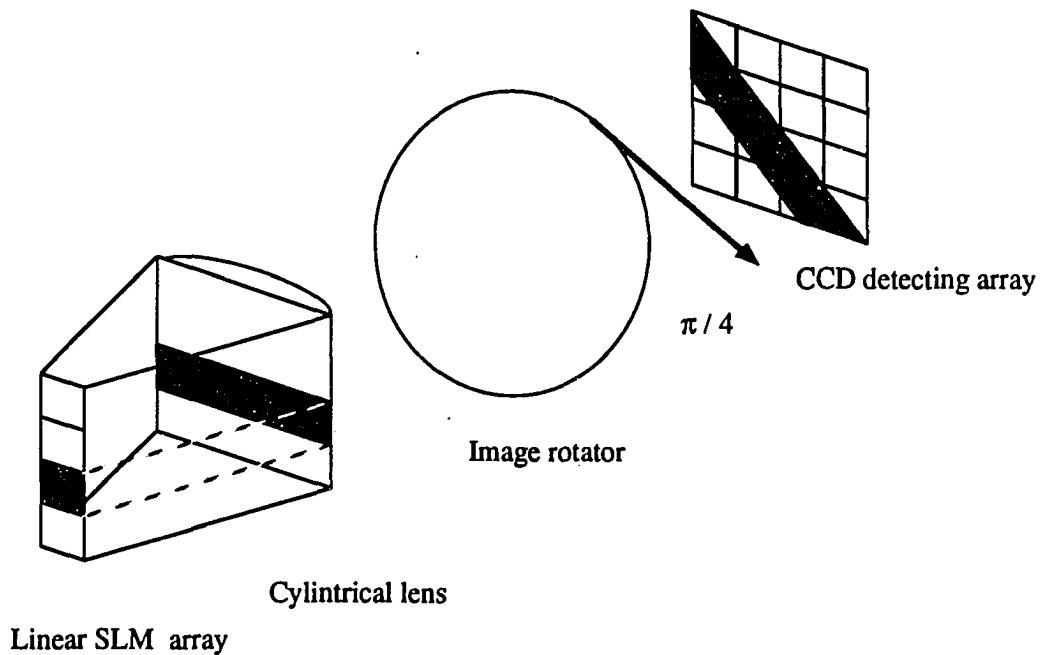


Fig. 6.3. The back projection processor. The projection data is back projected into the image space at the same angle as when the original measured projection was taken.

The transmissivity of the linear SLM array represents the magnitudes of the data in the projection space corresponding to a projection angle. The pattern in the linear array is then "stretched" into an array of strips as shown in Fig. 6.3. The linear SLM array is not specified deliberately since a wide range of choices are available. Among those choices is the Ferroelectric Liquid Crystal (FLC) SLM..

The image detection array integrates the projection data, corresponding to the area intercepted on the pixel by the light beam, at all the projection angles. The image detection array can be a CCD image detector or a commercial CCD TV camera.

A complete set of back projections involves performing back projection operations at all the projection angles over an angle of  $180^\circ$ . The purpose of the image rotator is to rotate the projection pattern to the corresponding projection angle relative to the image detector. The most commonly used image rotator consists of a dove prism image rotator [48] driven by a stepper motor. Fig. 6.4 shows a dove prism image rotator where the prism is rotated 0, 45 and 90 degrees and the image is rotated 0, 90, and 180 degrees correspondingly.

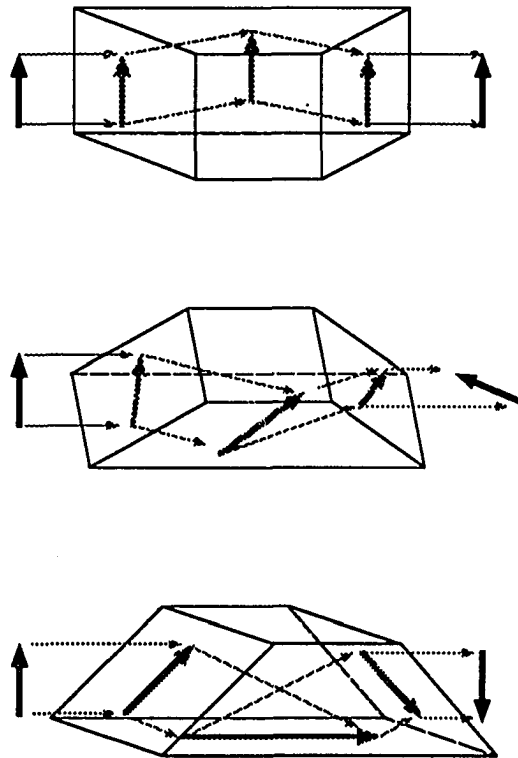


Fig. 6.4. A dove prism is rotated 0, 45, and 90 degrees counter-clock wise and an image is rotated 0, 90, and 180 degrees correspondingly.

The dove prism image rotator is not electronically connected to the mechanical rotating part. However, optical distortions may be introduced by the prism. The operation can also be performed by rotating the linear SLM array and the lens "back and forth" over a range of 180°. Alternative approaches using a static structure can also be employed.

#### **6.4.2 The optoelectronic forward projection processor**

The optoelectronic forward projection processor as shown in Fig. 6.5 performs the forward projection operation to map the data in the image space into the projection space.

It consists of:

- . an image display array.
- . a linear projection detector array and a cylindrical lens.
- . an image rotator.

The image display array displays a reconstructed image using either a two dimensional analog SLM or a commercial liquid crystal projection TV. The linear projection detector array detects the image generated by the cylindrical lens. The linear projection detector array can be a linear CCD array. The role and the design of the image rotator is identical to the one described in the preceding section.

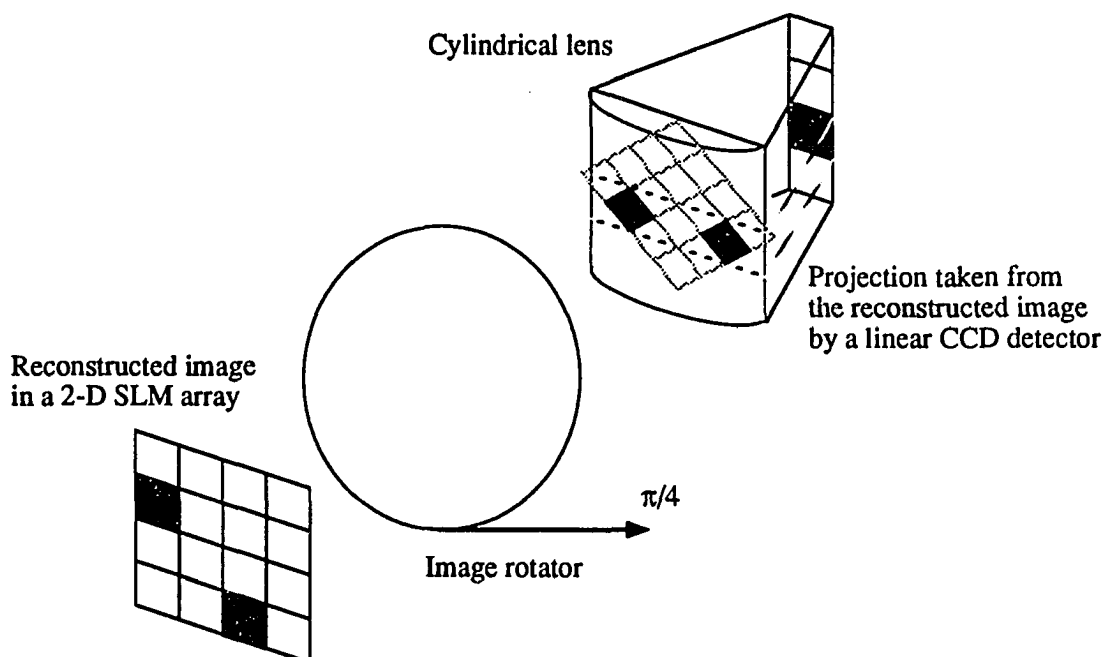


Fig. 6.5. The forward projection processor. The reconstructed image is forward projected into the projection space at the same angle at which the original measured projection was taken.

#### 6.4.3 The image space auxiliary processor

Since operations of image addition can be performed directly on the CCD array, a separate image auxiliary processor may not be required. However, when the performance of devices is not guaranteed, additional flexibility and improvement in accuracy can be gained by employing an auxiliary processor. The processor is required to be able to store a frame of the image and perform simple pixel by pixel addition or subtraction. Real-time digital video image processors which are commercially available can be used to perform these operations.

#### **6.4.4 The projection space auxiliary processor**

The basic functions of this auxiliary space processor are:

- . to receive data from the forward projection detector arrays.
- . perform simple arithmetic operations.
- . store projections.
- . send data to the back projection linear SLM array.

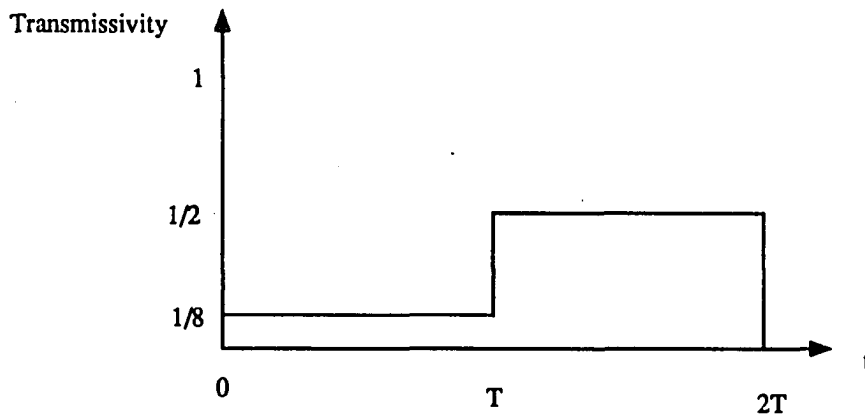
This basic auxiliary processor can be built using either a commercial digital microprocessor or a special purpose processor.

#### **6.5 Implementation of High Speed Analog SLM using Binary SLM**

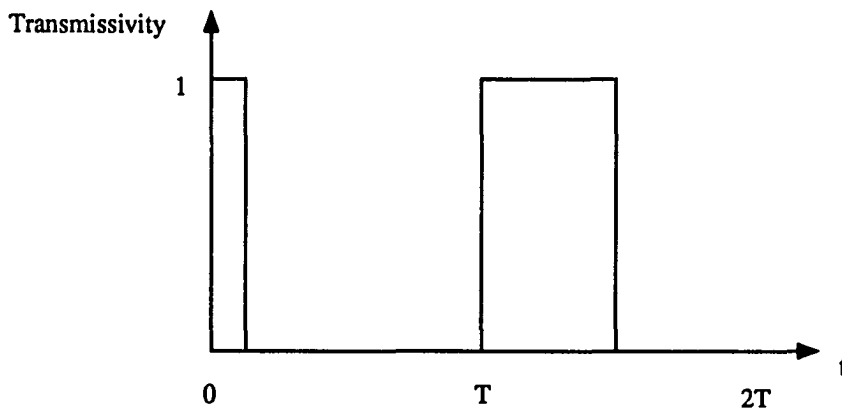
Most commercial analog SLM's are developed for building television displays. Examples include liquid crystal SLM panels used for image projectors. The refresh or update periods for analog SLM's are typically in the range of video frame rates, i.e., one to ten milliseconds. Unfortunately, the algorithms described earlier involve several hundreds of projections in each iteration. If such analog SLM's are used for implementing the 1-D back projections, then the resulting processing period will be in the range of a few seconds. In order to increase the processing speed, high speed 1-D analog SLM's are required. This can be accomplished by controlling the duration of exposure instead of relying on the need for varying the gray levels continuously.

CCD detectors are essentially integrating devices generating charge / voltage levels proportional to the intensity of the incident light and the exposure period. When the CCD

array is coupled with a SLM array, the charge / voltage levels in the CCD can be controlled by varying either the intensity of the light being integrated or the "ON" period of the SLM. Since most fast SLM's are binary in nature, we proposed to use the latter approach to control the CCD signal. The timing diagram of scheme is shown in Fig. 6.6.



a) Analog SLM



b) Implementation of analog SLM using binary SLM by time dividing.

Fig. 6.6. Scheme relying on the control of exposure period.

This circuit consists of a comparator, an address counter, a timing counter, timing memories, and registers as shown in Fig. 6.7. Values of grey levels of the SLM cells are preloaded into the timing memories. A cell is switched "OFF" when the value of the timing counter is larger than the value stored in the corresponding timing memory. The cell remains "ON" otherwise. During each timing counter clock period, the contents of the timing memories are read out sequentially with the address generated by the address counter.

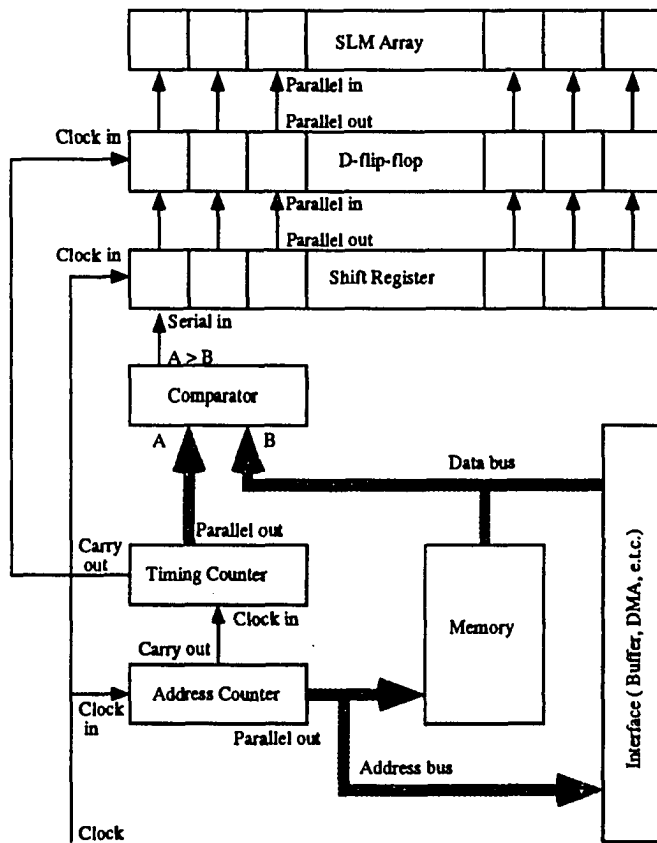


Fig. 6.7. A circuit implementing an analog SLM array using a binary SLM array.

An example involving four SLM cells and sixteen gray levels is shown in Fig. 6.8. The address counter is clocked at a period  $T_{\text{address}}$ . The timing counter is clocked by the carry output of the address counter whose period is  $T_{\text{timing}}$ . The period  $T_{\text{timing}} = m \times T_{\text{address}}$  where  $m$  is the number of SLM cells driven by the circuit. During each  $T_{\text{timing}}$ , all the timing parameters in the memories are scanned out and compared with the output of the timing counter. If the value read out from the memory is less the value of the counter, then the corresponding SLM cell is set to one, else it is reset to zero. The maximum number of gray levels which can be represented is given by

$$n = \frac{T_{\text{total}} - T_{\text{update}}}{T_{\text{address}} \times m} \quad (6.22)$$

where  $T_{\text{total}}$  is the frame period for an analog SLM and  $T_{\text{update}}$  is the time required for updating the memories. When the number of SLM cells is large, the speed depends on the speed of the circuit at which it can be driven.

After all the  $n$  gray levels are counted, the memories are updated by the external data with a fast memory access technique, such as a direct memory access scheme (DMA). When a large number of SLM cells are to be driven, the cells can be partitioned into blocks. The size of blocks depends on the desired driving speed.

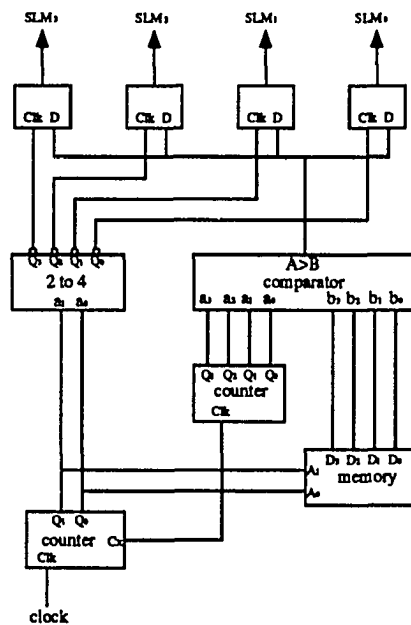


Fig. 6.8. An example for four SLM cells and sixteen gray levels.

### 6.5.1 Compensation Scheme

When the timing clock period is less than the SLM settling time, the resolution deteriorates. The problem can be circumvented by setting a constant zero bias exposure time which is equal to the minimum SLM settling time. The additional offset can be subtracted from the output of each CCD detector.

### 6.6 Methods for Eliminating The Effects of Limited Dynamic Range

The dynamic range of reconstructed image is mainly affected by three factors:

- a) The nonnegative offset associated with the projection data may reduce the actual dynamic range to approximately 10 %.

- b) The finite dynamic range of the back projection 1-D SLM array.
- c) The finite dynamic range of the forward projection 2-D SLM array.

The first effect can be eliminated by back projecting the positive and negative projection data separately. In addition, the error caused by the finite contrast ratio can also be minimized by using the dual projection scheme.

The RIRT described in eq. 6.14 provides a method for minimizing distortions caused by the finite dynamic ranges of the SLM arrays. In the iterative procedure, only back and forward projections of residuals are involved. In a stable feedback system, the magnitude of the residual will vanish as the number of iterations increase. Therefore, the vanishing residuals can always be adjusted to fit the maximum dynamic range of the SLM arrays and then rescaled back appropriately using the auxiliary processors after optical projections.

## 6.7 Results of Simulation

### 6.7.1 Acceleration using PC

Fig. 6.9 shows the reconstructed Shepp and Logan phantom at the 8<sup>th</sup>, 16<sup>th</sup>, 32<sup>nd</sup>, and 64<sup>th</sup> iterations when a third order FIR filter ( $n-3, n-1, n, n+1, n+3$ ) is used. Fig. 6.10 shows the reconstructed images obtained using the basic PIRT at the same iterations. Figs. 6.11 and 6.12 are cross-sections of reconstructed images using PIRT-PC and PIRT respectively where the number of iterations are 4, 8, 16 and 32. It is apparent that the convergence of high frequency components is accelerated considerably when a short FIR filter is used. However, the speed of convergence of the low frequency components does not improve.

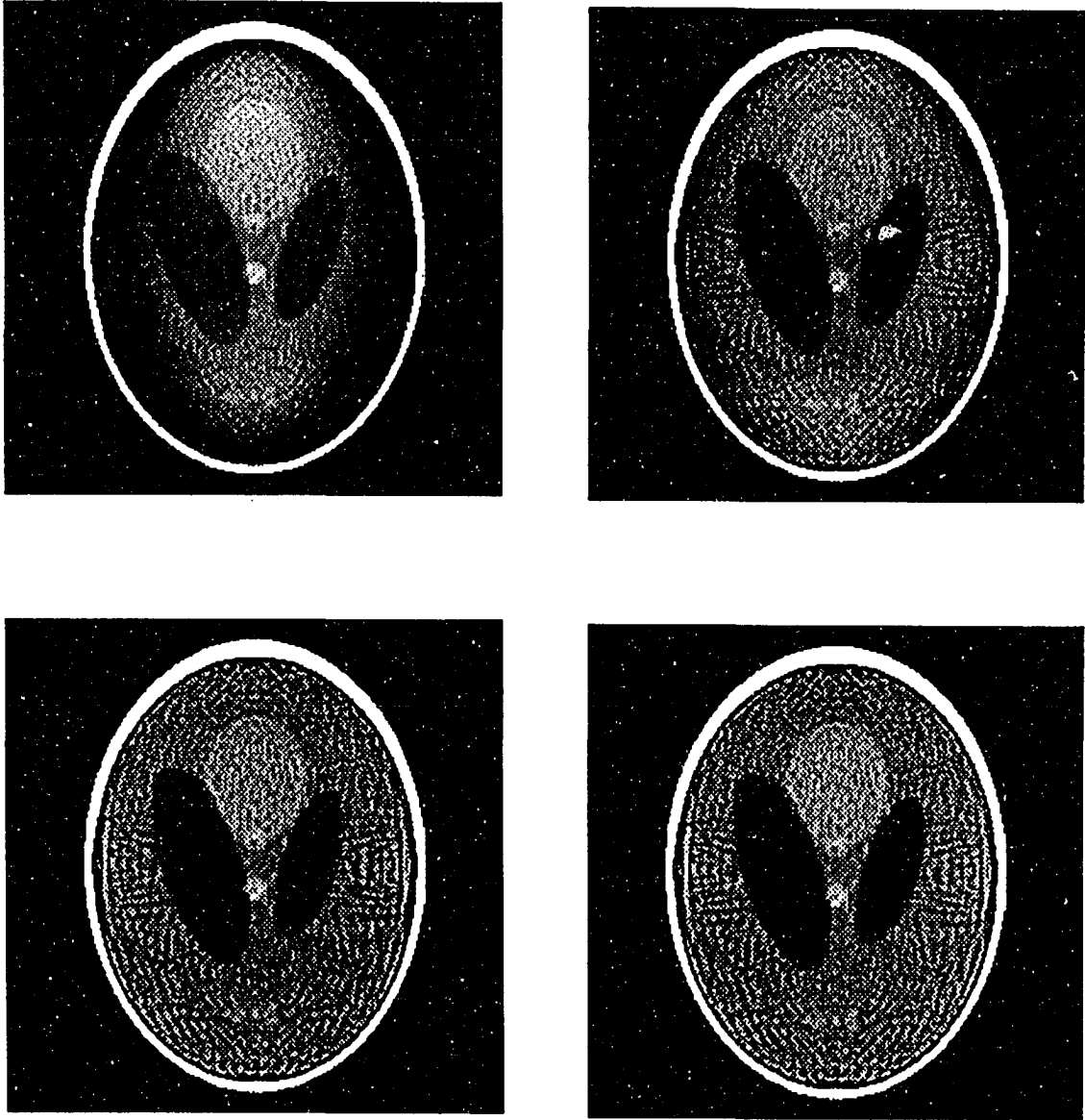


Fig. 6.9. Reconstructed image at the 8<sup>th</sup>, 16<sup>th</sup>, 32<sup>nd</sup> and 64<sup>th</sup> iterations obtained using PIRT-PC.

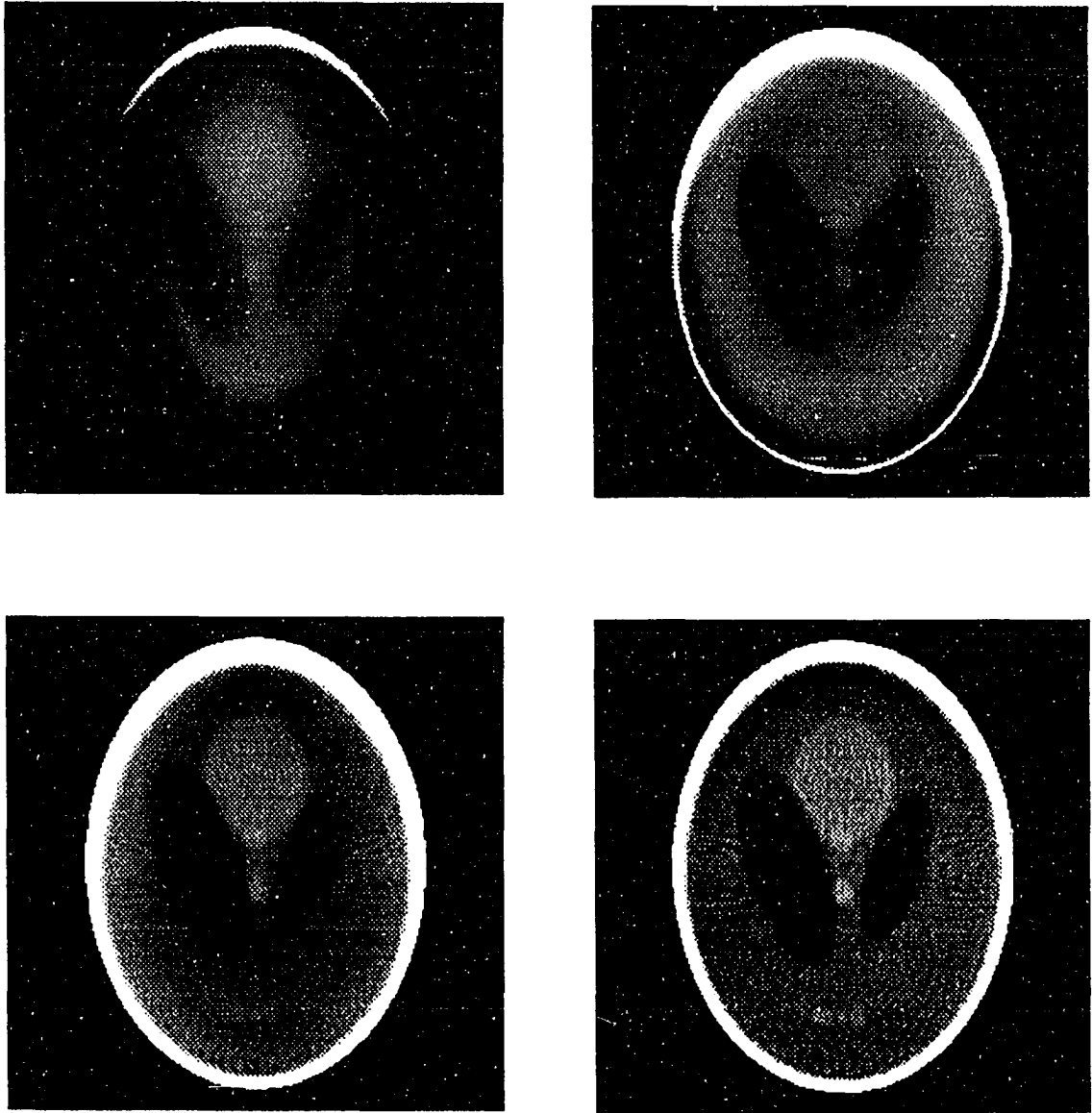


Fig. 6.10. Reconstructed image at the 8<sup>th</sup>, 16<sup>th</sup>, 32<sup>nd</sup> and 64<sup>th</sup> iterations obtained using basic PIRT.

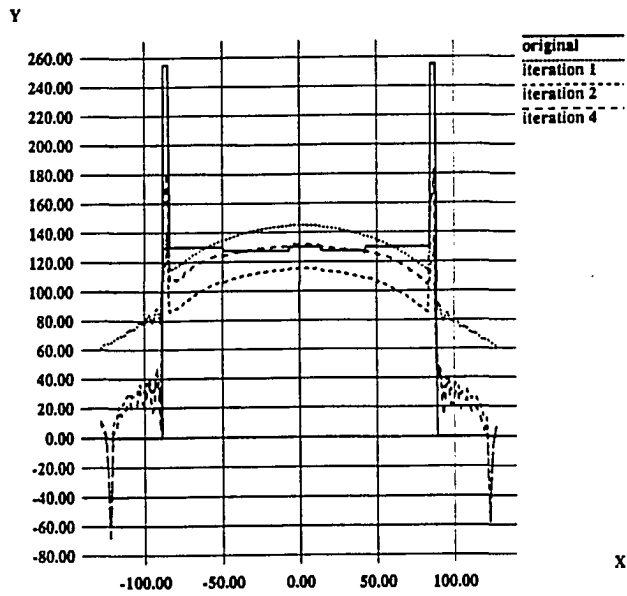


Fig. 6.11. Cross-sections of reconstructed image at the 1<sup>st</sup>, 2<sup>nd</sup>, 4<sup>th</sup> and 8<sup>th</sup> iterations obtained using PIRT-PC.

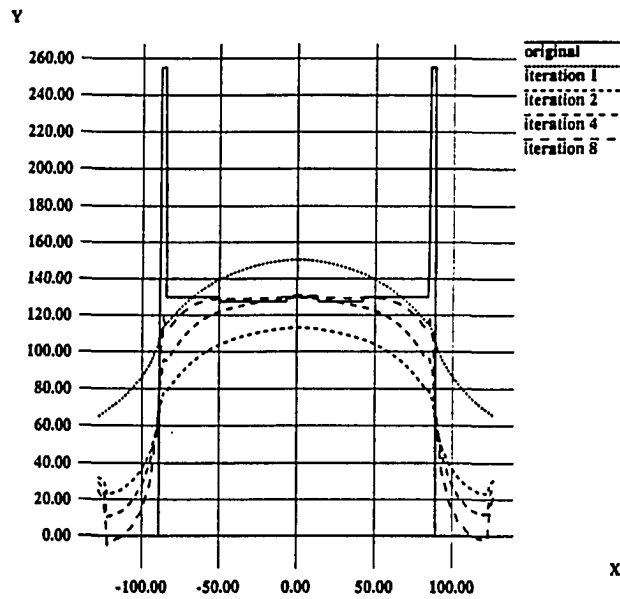


Fig. 6.12. Cross-sections of reconstructed image at the 1<sup>st</sup>, 2<sup>nd</sup>, 4<sup>th</sup> and 8<sup>th</sup> iterations obtained using basic PIRT.

Figs. 6.13 and 6.14 show plots of the cross sections at the 32<sup>nd</sup> and 64<sup>th</sup> iterations respectively. The error across the image, as shown in Fig. 6.13, is less than 1 % of the entire dynamic range except for regions where the variation is sharp. The plot shown in Fig. 6.14 indicates that there is very little improvement in the result after 32 iterations. If commercial video devices operating at 30 frames per second are employed, then the reconstruction time, with an expected contrast resolution of less than 1 %, is about 1 second.

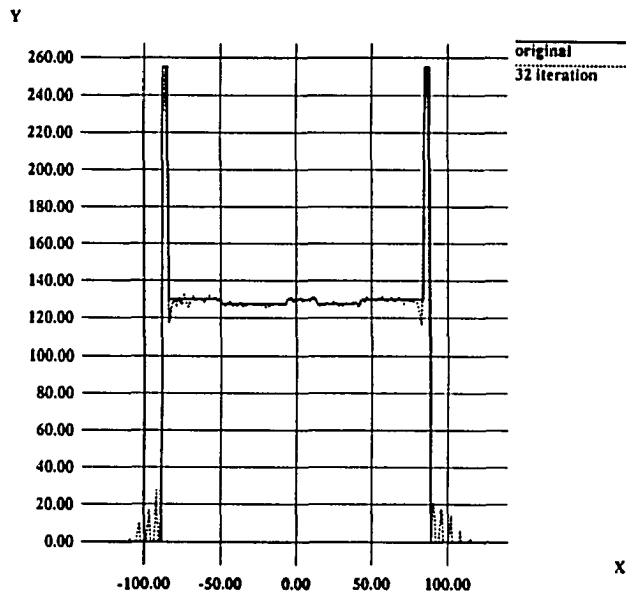


Fig. 6.13. Cross-sections of reconstructed image at the 32<sup>nd</sup> iteration obtained using PIRT-PC with constraints and assuming finite dynamic range.

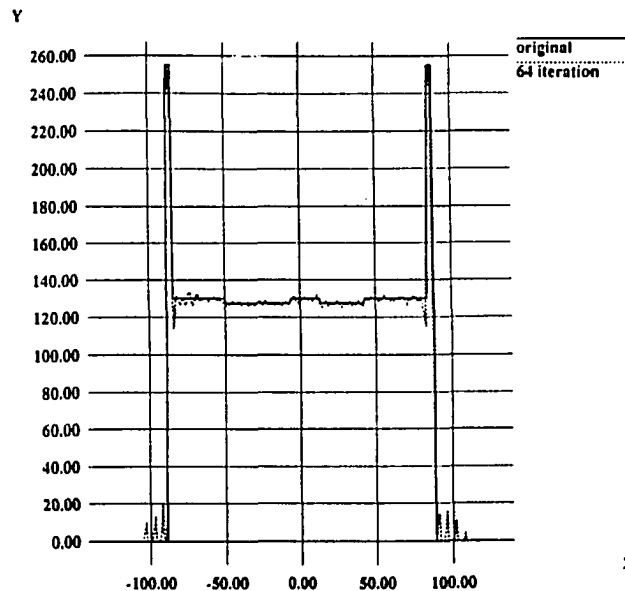


Fig. 6.14. Cross-sections of reconstructed image at the 64<sup>th</sup> iteration obtained using PIRT-PC with constraints and assuming finite dynamic range.

### 6.7.2 Reduction of Effects Caused by Finite SLM Dynamic Range

Finite dynamic ranges ( numbers of distinguishable grey levels ) of both forward and back projection SLM arrays represent the dominant source of distortion in the structure. The dynamic ranges of the available CCD arrays are much higher than those of available SLM arrays and consequently the effects can be neglected. In the simulation, 256 distinguishable gray levels are imposed by normalizing the state variable  $t$  and the reconstructed image  $x$  and quantizing them into 255 distinguishable levels before projecting. In addition, the reconstructed image is constrained to be within the range 0 to 255. Fig. 6.15 shows reconstructed images at the 8<sup>th</sup>, 16<sup>th</sup>, 32<sup>nd</sup> and the 64<sup>th</sup> iterations. The results show that, compared to the image obtained by PIRT-PC without quantization as seen in Fig. 6.9, the distortion is insignificant.

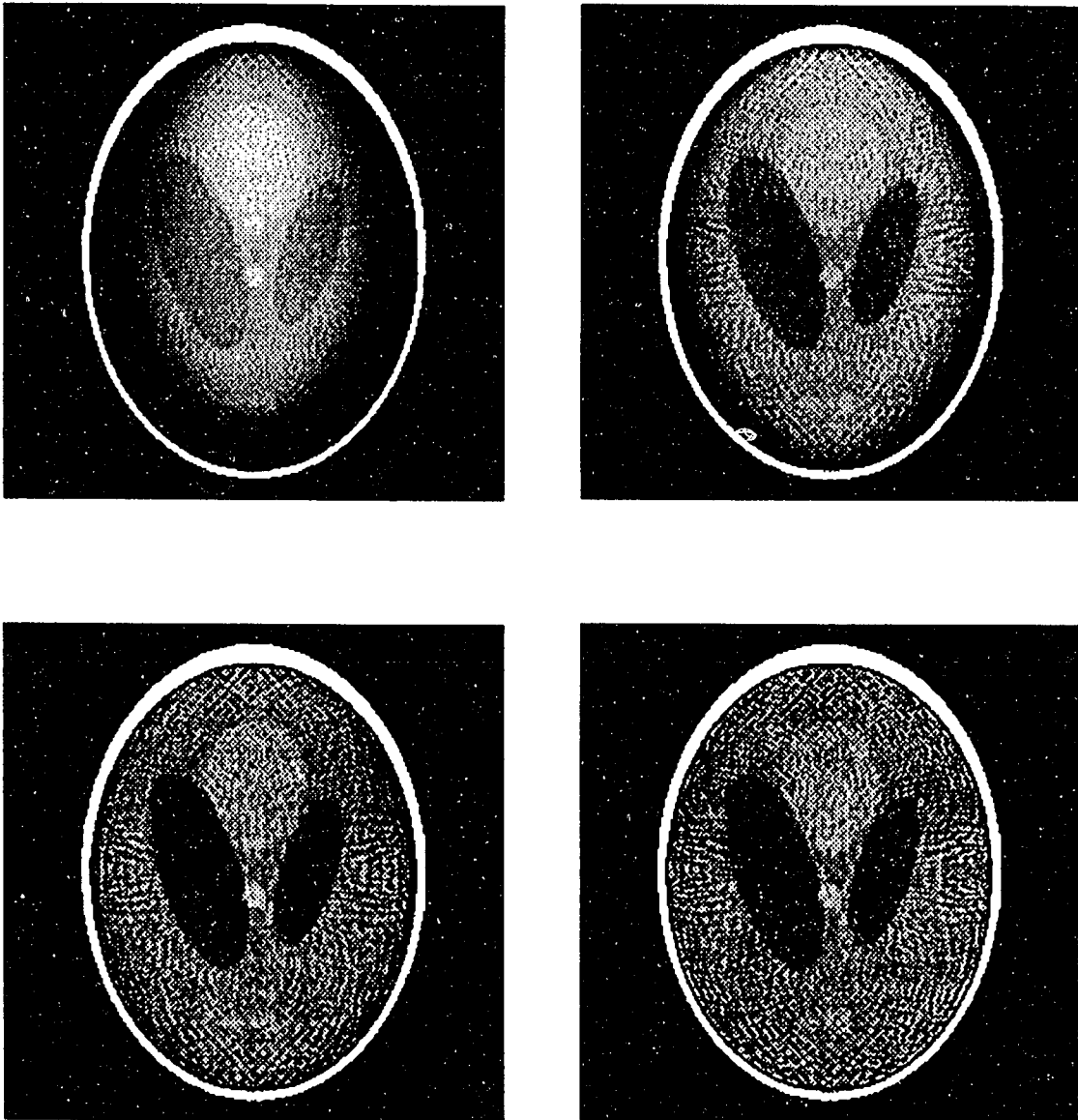


Fig. 6.15. Reconstructed image at the 8<sup>th</sup>, 16<sup>th</sup>, 32<sup>nd</sup> and 64<sup>th</sup> iterations obtained using PIRT-PC with constraints and assuming finite dynamic range.

### 6.7.3 Effect of Nonnegative Bias

If all projections are biased to nonnegative values, then, only about ten percent of the dynamic range in the image space is available. Fig. 6.16 shows a plot of the cross-section of a reconstructed image using this strategy. However, if projections are separated into positive and negative projections and back projected separately, then, there is no degradation in the useful dynamic range in the image space as shown by the plot in Fig. 6.17.

## 6.8 Summary

The PIRT-PC proposed in this Chapter is a combination of PIRT and reduced CBP. This algorithm is capable of reducing the cost associated with a full size convolution with CBP, correct the errors of reduced length convolutions, and possesses superior convergence properties relating to PIRT. In addition, the method guarantees the minimum-norm solution for an underdetermined system.

The proposed hybrid prototype described in this Chapter represents a practical design which can be built using off-the-shelf video and optoelectronic devices. The prototype design represents a first step. The additional electronic processors in the projection and the image space not only offer flexibility which is necessary while building the first prototype. But also enables us to investigate other algorithms. In comparison with existing approaches,

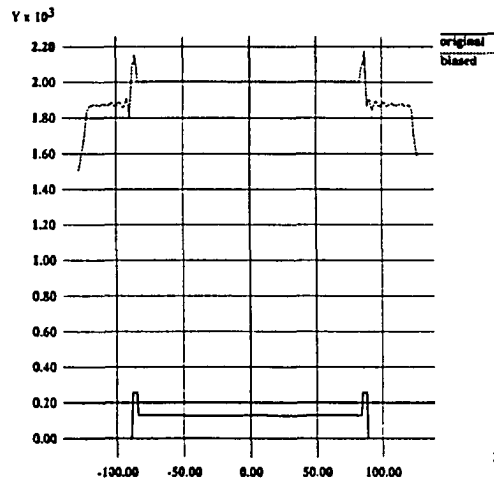


Fig. 6.16. A cross-section of an image where all projections are biased to non-negative values.

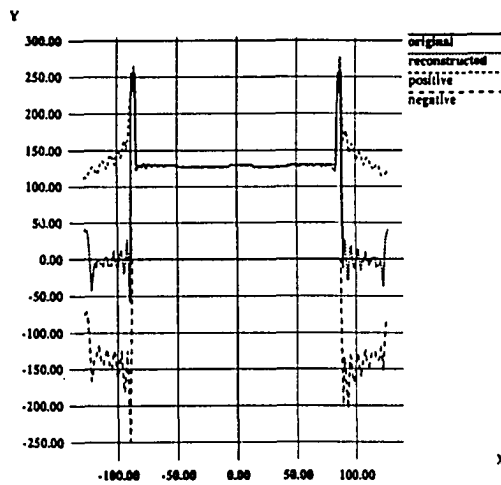


Fig. 6.17. Cross-sections of two reconstructed images where the images are reconstructed by processing positive and negative projections separately.

the proposed structure offers

- \* reduced dependency on the accuracy of filter devices.
- \* reduced dependency on the precision and dynamic range of optoelectronic devices.
- \* significant reduction in the cost of filtering devices.

## CHAPTER 7. CONCLUSIONS

Several iterative tomographic image reconstruction methods have been presented in this dissertation. These methods are based on the projection iterative reconstruction technique. In contrast to conventional approaches, the algorithms described in this dissertation offer superior results when the tomographic system is underdetermined and computational errors are present.

---

New system concepts, involving the use of optoelectronic devices for implementing iterative tomographic image reconstruction algorithms, have also been proposed in this dissertation. The optoelectronic feedback structures built with conventional optical and imaging devices offer high speed reconstructions with quality levels required in medical applications.

### 7.1 Comparison of PIRT and SIRT

In this dissertation, the PIRT algorithm has been developed for tomographic image reconstruction. As shown in Table 7.1, the new algorithm differs from the conventional iterative algorithms, such as SIRT, in that it solves for a state vector in the projection space in contrast to conventional algorithms which solve for the solution in the image space. The feed back process in PIRT is performed in the projection space. Hence, iterative error

corrections in the image space are avoided. The feedback scheme in SIRT is implemented in the image space leading to complications in optoelectronic implementations.

When a system is underdetermined, the new algorithm PIRT is superior to the conventional SIRT algorithm since it guarantees a unique minimum-norm solution. The properties of the two algorithms are compared in table 7.2.

However, the PIRT is not useful for solving overdetermined systems since the state vector may diverge in the projection space as show in table 7.3.

**Table. 7.1. SIRT and PIRT Algorithms**

<i>algorithm</i>	<i>SIRT</i>	<i>PIRT</i>
expression	$x(k)=x(k-1)+A^T(b-Ax(k-1))$	$t(k)=t(k-1)+(b-AA^Tt(k-1))$
feedback	image space	projection space

**Table. 7.2. Comparison of Performance for Underdetermined Systems**

<i>algorithm</i>	<i>SIRT</i>	<i>PIRT</i>
solution	not unique	minimum-norm
convergence	not unique	guaranteed
cg method	does not converge	guaranteed
initial image	no unique solution	minimum norm of difference
with constraint	no unique solution	minimum-norm in reduce space

**Table. 7.3. Comparison of Performance for Overdetermined Systems**

<i>algorithm</i>	<i>SIRT</i>	<i>PIRT</i>
solution	least squares	least squares
convergence	guaranteed	diverges in projection space

## 7.2 Summary of The Proposed Algorithms

The tomographic reconstruction algorithms described in this dissertation include PIRT, PIRT-CG, PIRT-PC, RIRT and IFBP.

The PIRT is a basic iterative algorithm for solving large sparse underdetermined systems. The PIRT is considered as a counterpart of the conventional iterative algorithm SIRT. The PIRT solves for the minimum-norm solution of normal equations whereas the conventional algorithms are based on a strategy for computing the least squares solutions. The PIRT guarantees unique solutions for underdetermined systems while conventional algorithms provide unique solutions when systems are overdetermined.

The PIRT-CG method differs from the conventional SIRT-CG methods in that it applies the conjugate gradient acceleration method to solve for a state vector in the projection space instead of directly solving for a solution vector in the image space. Therefore, when the system is underdetermined, the algorithm does not diverge since the matrix of the state equation is not singular.

The PIRT-PC method is another accelerated PIRT type algorithm in which a short order FIR filter is used to speed up the convergence of high frequency components. Results show that when a third order filter is used, the convergence can be accelerated significantly. The PIRT-PC is a simple and efficient algorithm, and should therefore be preferred for optoelectronic implementations.

The RIRT recursively eliminates the residue in the projection space instead of building a state vector. RIRT algorithms are equivalent to SIRT, PIRT, PIRT-CG, PIRT-PC

or the steepest descent type algorithms depending on the acceleration technique used. When computational errors exist, the algorithm does not guarantee uniqueness of the solution.

The IFBP is a SIRT type algorithm whose convergence properties are improved by using a spatial frequency filter. This algorithm is mainly useful for optoelectronic implementations since optical devices can be used to build a fast spatial frequency domain filter although the accuracy is relatively poor. The structure uses a feedback scheme to eliminate distortions associated with optical transforms.

### **7.3 Summary of The Proposed Optoelectronic Structures**

Optoelectronic implementations of SIRT, IFBP and the PIRT type algorithms have been proposed in this dissertation.

The structure implementing SIRT is simple and does not employ sophisticated filtering or convolution processing units. The structure for implementing IFBP using optoelectronic devices employs a high speed, low accuracy, inexpensive optical filter to accelerate convergence.

In the case of SIRT, the error corrections are superimposed on the previously reconstructed image. Therefore, errors introduced by optoelectronic devices may be accumulated in the reconstructed image. This is especially true, if the system is underdetermined where the accumulated errors may cause divergence and reach the dynamic range limits of devices. With the proposed PIRT algorithm, the need for superimposing images is eliminated. This leads to a smoother image with a better spatial resolution from

fewer projection data. The PIRT has reduced the complexity of structures for optoelectronic tomographic reconstruction. In addition, schemes for acceleration, such as PIRT-PC, can be implemented without additional expense.

#### **7.4 Areas of Future Work in Algorithms**

Iterative tomographic image reconstruction algorithms are commonly used in single photon emission computerized tomography (SPECT) and positron emission tomography (PET). Applications of PIRT type algorithms for SPECT and PET applications need to be developed further.

Many iterative estimation algorithms have been developed based on statistical models of tomographic systems. Some of these algorithms can be implemented using PIRT as a tool.

#### **7.5 Areas of Future Work in Structures**

In this dissertation, only optoelectronic implementations of additive iterative reconstruction algorithms have been presented. Multiplicative iterative reconstruction algorithms are also commonly used. Multiplicative algorithms offer solutions which are nonnegative and are therefore attractive for optoelectronic implementation.

Multiplicative x-ray tomographic algorithms can be implemented with a slightly modified optoelectronic structure. In the modified structure, only an additional SLM array

needs to be coupled to the back projection CCD array. The system concept is straightforward. However, the theoretical foundations are yet to be developed.

### **7.6 Prototype Development**

A hybrid prototype for implementing the iterative algorithms has been proposed. The hybrid structure can provide flexibility required for pursuing further research. The prototype can be built using commercial available optoelectronic devices and reach a speed of 30 frames per second.

### **7.7 Summary**

In this dissertation, novel optoelectronic systems for implementing iterative tomographic image reconstruction algorithms have been proposed. In order to exploit the advantages of optoelectronic devices fully, a new iterative tomographic image reconstruction algorithm - PIRT has been developed. The PIRT algorithm is general, in that it can be employed to solve a wide variety of problems involving large sparse matrices and underdetermined systems. The ideas developed in this dissertation are, therefore, far broader in scope than their narrow application to tomographic reconstruction described here would suggest.

**BIBLIOGRAPHY**

- [1] G.N. Hounsfield, "A method and apparatus for examination of a body by radiation such as X or gamma radiation," *Patent Specification 1283915*, The Patent Office, London, England, 1972.
- [2] G.N. Hounsfield, "Computerized transverse axial scanning tomography: Part 1, description of the system," *Br. J. Radiol.*, **46**, pp. 1015-1022, 1973.
- [3] A.M. Cormack, "Representation of a function by its line integrals, with some radiological applications," *J. Appl. Phys.*, **34**, pp. 2722-2727, 1963.
- [4] P. Gilbert, "Iterative method for the three-dimensional reconstruction of an object from projections," *J. Theor. Biol.*, **36**, pp. 105-117, 1972.
- [5] T. Lu, "An iterative method of underdetermined system for tomographic image reconstruction," An Internal Project Report for Math 509, Iowa State University, May 9, 1991.
- [6] T. Lu, S.S. Udpa, and L. Udpa, "Projection iterative reconstruction technique and optoelectronic implementation," *Proc. IEEE ISCAS'92*, pp. 2469-2472, San Diego, May 10-13, 1992.
- [7] T.M. Peter, "Spatial filtering to improve transverse tomography," *IEEE Trans. On Biomed. Eng.*, **21**, pp. 214-219, 1974.
- [8] T. Lu, S.S. Udpa, and L. Udpa, "Tomographic reconstruction using optoelectronic structures," *Proc. of IEEE ISCAS'91*, **1**, pp. 476-479, Singapore, Jun., 1991.
- [9] T. Lu, S.S. Udpa, and L. Udpa, "Optoelectronic implementation of filtered back projection tomography algorithm," *Proc. of SPIE 1991 Int. Symp. on Optical Appl. Sci. and Eng. on Opt. Inform. Proc. Syst. and Arch. III*, SPIE **1564**, pp. 704-713, San Diego, Jul. 21-26, 1991.
- [10] A. C. Kak, and M. Slaney, *Principles of Computerized Tomographic Imaging*, IEEE Press, New York, 1987.

- [11] G. Herman, *Image Reconstruction from Projections - The Fundamentals of Computerized Tomography*, Academic Press, New York, 1980.
- [12] K. Iizuka, *Optical Engineering*, Second Ed., Springer Ser. in Opt. Sci., **35**, Springer-Verlag, New York, 1987.
- [13] J. Radon, "Über die bestimmung von funktionen durch ihre integralwerte langs gewisser mannigfaltigkeiten," *Ber. Verb. Saechs. Akad. Wiss., Leipzig. Math. Phys. Kl.*, **69**, pp. 262-277, 1917.
- [14] R. Gordon, R. Bender, and G.T. Herman, "Algebraic reconstruction techniques (ART) for three-dimensional electron microscopy and x-ray photography," *J. Theor. Biol.*, **29**, pp. 471-481, 1970.
- [15] S. Kaczmarz, "Angenaherte auflosung von systemen linearer gleichungen," *Bull. Acad. Pol. Sci. Lett. A.*, **6(8A)**, pp. 355-357, 1937.
- [16] L. Landweber, "An Iterative formula for Fredholm integral equations of the first kind," *Amer. J. Math.*, **73**, pp. 615-624, 1951.
- [17] M.R. Hestenes, and E. Stiefel, "Methods of conjugate gradients for solving linear systems," *J. Res. Nat. Bur. Standards*, **29**, pp. 150-165, 1952.
- [18] E. Artzy, and G.T. Herman, "Quadratic optimization for image reconstruction II," *Comput. Graphics Im. Proc.*, **II**, pp. 242-261, 1979.
- [19] T.S. Pan, and A.E. Yagle, "Numerical study of multigrid implementations of some iterative reconstruction algorithms," *IEEE Trans. on Med. Img.*, **10(4)**, pp. 572-588, Dec., 1991.
- [20] S. Holte, P. Schmidlin, A. Linden, G. Rosenqvist, and L. Eriksson, "Iterative image reconstruction for positron emission tomography: A study of convergence and quatization problems," *IEEE Trans. on Nucl. Sci.*, **37(2)**, pp. 629-635, Apr., 1990.
- [21] G. Minerbo, "MENT: A maximum entropy algorithm for reconstructing a source from projection data," *Comput. Graph. Im. Proc.*, **10**, pp. 48-68, 1979.
- [22] N.J. Dusaussoy, and E. Abdou, "The Extended MENT Algorithm: A Maximum Entropy Type Algorithm Using Prior Knowledge for Computerized Tomography," *IEEE Trans. on Signal Proc.*, **39(5)**, pp. 1164-1180, May, 1991.

- [23] A.P. Dempster, N.M. Laird, and D.B. Rubin, "Maximum Likelihood from incomplete data via the EM algorithm," *J. Royal St. Soc.*, **39**, pp. 1-38, 1977.
- [24] L.A. Shepp, and Y. Vardi, "Maximum Likelihood Reconstruction for Emission Tomography," *IEEE Trans. on Med. Im.*, **MI-1(2)**, pp. 113-122, Oct., 1982.
- [25] L. Kaufman, "Implementing and Accelerating the EM Algorithm for Positron Emission Tomography," *IEEE Tran. on Med. Im.*, **MI-6(1)**, pp. 37-51, Mar., 1987.
- [26] J.H. Kim, K.Y. Kwak, and S.B. Park. "Iterative reconstruction-reprojection in projection space," *Proc. IEEE*, **73**, pp. 1140-1141, Jun., 1985.
- [27] J.H. Kim, K.Y. Kwak, S.B. Park, and Z.H. Cho, "Projection space iteration reconstruction\_reprojection," *IEEE Trans. on Med. Img.*, **MI-4(3)**, pp. 139-143, Sep., 1985.
- [28] J.L. Prince, and A.S. Willsky, "A projection space MAP method for limited angle reconstruction," *Proc. IEEE ICASSP'88*, pp. 1268-1271, 1988.
- [29] J.L. Prince, and A.S. Willsky, "A geometric projection-space reconstruction algorithm," *Lin. Alg. and Its Appl.*, **130**, pp. 151-191, 1990.
- [30] J.L. Prince, and A. S. Willsky, "Reconstructing convex sets from support line measurements," *IEEE Trans. on PAMI*, **12(4)**, pp. 377-389, Apr., 1990.
- [31] S. Kawata, and O. Nalcioglu, "Constrained iterative reconstruction by the conjugate gradient method," *IEEE Trans. on Med. Im.*, **MI-4(2)**, pp. 65-71, Jun., 1985.
- [32] A. van der Sluis, and A. van der Vorst, "SIRT- and CG-type methods for the iterative solution of sparse linear-squares problems," Special issue on linear algebra in computed tomography, ed. by G.T. Herman, *Linear Alg. and Its Appl.*, **130**, pp. 257-303, 1990.
- [33] G. Demoment, "Image Reconstruction and restoration: Overview of common estimation structures and problems," *IEEE Trans. ASSP*, **37**, pp. 2024-2036, Dec., 1989.
- [34] D.C. Youla, and H. Webb, "Image restoration by the method of convex projections: Part 2 - applications and numerical results," *IEEE Trans. on Med. Img.*, **MI-1(2)**, pp. 95-101, Oct., 1982.

- [35] S. Kou, R. Mammone, J. Doherty, and C. Podilchak, "Reconstruction enhancement of reconstructed images by using image restoration technique," *Proc. IEEE Int. Conf. EMBS*, Philadelphia, Nov., 1990.
- [36] C. Hamaker, and D.C. Solmon, "The angle between the null spaces of x-ray," *J. Math. Anal. Appl.*, **62**, pp. 1-23, 1978.
- [37] K. Tanabe, "Projection method for solving a singular system," *Numer. Math.*, **17**, pp. 203-214, 1973.
- [38] A.H. Andersen, and A.C. Kak, "Simultaneous algebraic reconstruction technique (SART): A superior implementation of the ART algorithm," *Ultr. Im.*, **6**, pp. 81-94, 1984.
- [39] A.H. Andersen, "Tomography transform and inverse in geometrical optics," *J. Opt. Soc. Am. A.*, **4**(8), pp. 1385-1395, Aug., 1987.
- [40] S. Duinker, R.J. Geluk, and H. Molder, "Transaxial analogue tomography," *Oldelft Sci. Eng. Q.*, **1**, pp. 41-66, 1978.
- [41] P. Edholm, L.G. Hellstrom, and B. Jacobson, "Transverse tomography with incoherent optical reconstruction," *Phys. Med. Biol.*, **23**, pp. 90-99, 1978.
- [42] P. Edholm, "Tomogram reconstruction using an opticophotographic method," *ACTA Radiol. Diag.*, **18**, pp. 126-143, 1977.
- [43] H.H. Barrett, and W. Swindell, "Analog reconstruction methods for transaxial tomography," *Proc. IEEE*, **65**, pp. 89-107, 1977.
- [44] A.F. Gmitro, J.E. Grevenkamp, W. Swindell, H.H. Barrett, M.Y. Chiu, and S.K. Gordon, "Optical computers for reconstructing objects from their x-ray projections," *Optical Engineering*, **19**(3), pp. 260-271, May/Jun., 1980.
- [45] G. Gindi, and A. Gmitro, "Optical Feature extraction via the Radon transform," *Opt. Eng.*, **23**(5), pp. 499-506, Sep./Oct., 1984.
- [46] R. Easton, Jr., and H.H. Barrett, "Tomographic transformations in optical signal processing," ed. by J. L. Homer, *Optical Signal Processing*, Academic Press Inc., San Diego, 1987.
- [47] A. M. Garvie, and G. C. Sorell, "Video-based analog tomography," *Rev. Sci. Instrum.*, **61**(1), pp. 128-145, Jan., 1990.

- [48] A. F. Gmitro, V. Tresp and G. Gind, "Videographic tomography-part I: Reconstruction with parallel-beam projection data," *IEEE Trans. on Med. Im.*, 9(4), pp. 366-357, Dec., 1990.
- [49] E. Kaneko, *Liquid Crystal TV Displays: Principles and Applications of Liquid Crystal Displays*, KTK scientific publishers, Tokyo, D. Reidel publishing company, Boston, 1987.
- [50] D.G. Feitelson, *Optical Computing - A Survey for Computer Scientists*, MIT Press, Cambridge, Massachusetts, 1988.
- [51] A.D. McAulay, *Optical Computer Architectures - The Application of Optical Concepts to Next Generation Computers*, John Wiley & Sons, Inc., New York, 1991.
- [52] J.A. Neff, R.A. Athale, and S.H. Lee, "Two-dimensional spatial light modulators: A tutorial," *Proc. of IEEE*, 78(5), pp. 826-855, May, 1990.
- [53] A.D. Fisher, "Spatial light modulators: functional capabilities, applications, and devices," *Int. J. of Opto.*, 5(2), pp. 125-167, Sep., 1990.
- [54] D.A. Jared, and K.M. Johnson, "Ferroelectric liquid crystal spatial light modulators," *SPIE Critical Review Series-Spatial Light Modulators and Applications III*, SPIE 1150, pp. 46-59, San Diego, Aug. 7-8, 1989.
- [55] K.B. Nichols, B.E. Burke, B.F. Aull, W.D. Goodhue, B.F. Gramstorff, C.D. Hoyt, and A. Vera, "Spatial light modulators using charge-coupled-device addressing and electroabsorption effects in GaAs/AlGaAs multiple quantum wells," *Appl. Phys. Lett.*, 52(14), pp. 1116-1118, Apr. 4, 1988.
- [56] T.Y. Hsu, and U. Efron, "Multiple quantum well spatial light modulators," *SPIE Critical Review Series-Spatial Light Modulators and Applications III*, SPIE 1150, pp. 61-85, San Diego, Aug. 7-8, 1989.
- [57] B.E. Burk and J.A. Higgins, "Optical processor components based on GaAs CCD Technology," R. Arrathoon, Ed., *Optical Computing*, Marcel Dekker Inc., New York, 1989.
- [58] B. Javidi, Ed., "SLMs standardized", *Signal & Image Processing*, SPIE Int. Tech. Working Group Newsletter, 2(2), pp. 5, Nov., 1991.
- [59] W.B. Boyle, and G.E. Smith, "Charge-Coupled Semiconductor Devices," *Bell Syst. Techn. J.*, 49, pp. 587-593, Apr., 1970.

- [60] D.K. Schroder, *Advanced MOS devices*, Modular Series on Solid State Devices, G.W. Neudeck, and R.F. Pierret, Eds., Addison-Wesley publishing Co. Inc., New York, 1987.
- [61] D.F. Barbe, ed, *Charge-Coupled Devices*, Topic in Applied Physics, 38, Springer-Verlag, New York, 1980.
- [62] C. D. Knittle, and S. S. Udpa, "Stochastic modeling of the optical distributed arithmetic unit," *Proc. of Opt. Comput.* 88, SPIE 963, pp. 58-65, 1988.
- [63] C.D. Knittle, S.S. Udpa, and S.C. Chan, "SLM/CCD structure for high speed signal processing," *IEEE ISCAS'90*, pp. 2361-2364, New Orleans, May 1-3, 1990.
- [64] J. Boddu, S.S. Udpa, L. Udpa, and S.C. Chan, "High-speed signal processing architectures using charge-coupled devices," *Proc. of SPIE-Device for Optical Processing*, SPIE 1562, pp. 251-262, San Diego, Jul. 23-24, 1991.
- [65] J.J. Tiemann, T.L. Vogelsong, and A.S. Steckl, "Charge Domain Recursive Filters," *IEEE J. of Solid-St. Cir.*, SC-17(3), pp. 597-605, Jun., 1982.
- [66] T. Vogelsong, J.J. Tiemann, and A. Steckl, "Charge-domain integrated circuits for signal processing," *IEEE J. Solid-St. Cir.*, SC-20(2), pp. 562-570, Apr., 1985.
- [67] E.R. Fossum, "Charge-coupled computing for focal plane image preprocessing," *Opt. Eng.*, 26(9), pp. 916-922, Sep. 1987.
- [68] J.V.D. Spiegel, G.Kreider, et al., "A foveated retina-like sensor using CCD technology," *Analog VLSI Implementation of Neural Systems*, C. Mead and M. Ismail, Eds., Kluwer Academic Publishers, Boston, 1989.
- [69] T. Lu, L. Udpa, and S.S. Udpa, "High speed image processing via SLM/CCD devices," *Proc. IEEE ISCAS'90*, pp. 763-766, New Orleans, May 1-3, 1990.
- [70] T. Lu, L. Udpa, and S.S. Udpa, "Novel devices for high speed computer vision," *Proc. of ISMM'91*, Long Beach, Dec. 16, 1991.
- [71] H. Dollekamp, L.J.M. Esser, and H.de Jong, "P<sup>2</sup>CCD in 60 MHz oscilloscope with digital image storage," *Philips Tech. Rev.*, 40, pp. 55-60, May, 1982.
- [72] *Loral Fairchild CCD Databook - CCD Sensors, Systems and Developmental Technology*, Loral Fairchild Imaging Sensors, 1991.

- [73] L. A. Hageman, and D. Young, *Applied Iterative Methods*, Academic Press, Inc., New York, 1981.
- [74] W. W. Hager, *Applied Numerical Linear Algebra*, Prentice-Hall, Englewood Cliff, New Jersey, 1988.
- [75] L.A.Shepp, and B.F. Logan, "The Fourier reconstruction of a head section," *IEEE Trans. Nucl. Sci.*, NS-21, pp. 21-24, 1974.
- [76] L.L. Scharf, *Statistical Signal Processing - Detection, Estimation, and Time Series Analysis*, Addison-Wesley Publishing Company Inc., New York, 1991.
- [77] E.J. Craig, "The N-step iteration procedure," *J. Math. Phys.*, **34**, pp. 67-73, 1955.
- [78] J. Stoer, "Solution of large linear systems of equations by conjugate gradient type methods," *Mathematical Programming - The State of the Art*, A. Bachem, M. Grottschel and B. Korte, Eds., Springer-Verlag, New York, 1983.
- [79] S.H. Lee, *Optical Information Processing: Fundamentals*, S.H.Lee, Ed., Springer-Verlag, New York, 1981.
- [80] D. Casasent, "Optical Feature Extraction", J. L. Horner, Ed., *Optical Signal Processing*, Academic Press Inc., San Diego, 1987.